A SUBSPACE APPROACH TO ACCELERATED CARDIOVASCULAR MAGNETIC RESONANCE IMAGING

BY

ANTHONY GLENN CHRISTODOULOU

DISSERTATION

Submitted in partial fulfillment of the requirements
for the degree of Doctor of Philosophy in Electrical and Computer Engineering
in the Graduate College of the
University of Illinois at Urbana-Champaign, 2015

Urbana, Illinois

Doctoral Committee:

Professor Zhi-Pei Liang, Chair
Professor Stephen A. Boppart
Professor Minh N. Do
Associate Professor Bradley P. Sutton

Abstract

Magnetic resonance imaging (MRI) is a uniquely flexible tool for imaging the heart, as it has the potential to perform a significant number of structural and functional cardiovascular assessments. However, the low imaging speed of MRI has limited its clinical application. The assessments that are currently performed in a clinical setting are typically done using gated methodologies, which are complicated by respiration and fail for patients with cardiac arrhythmias. This dissertation describes a subspace approach to accelerate cardiovascular MRI, freeing cardiac MRI from gating techniques and enabling whole-heart 3D dynamic imaging for multiple simultaneous assessments.

This imaging approach comprises developments in image modeling, data acquisition, and image reconstruction. A spatiotemporal image model is designed to represent the particular subspace structure of cardiovascular images. The data acquisition development is composed of: a) a sampling strategy which allows integration of the subspace model, parallel imaging, and sparse modeling; b) a novel pulse sequence implementing "self-navigation" for collecting both auxiliary data (for temporal subspace estimation) and imaging data after every excitation; and c) **k**-space trajectory evaluation and design, replacing Cartesian trajectories which are highly sensitive to readout direction. The image reconstruction work centers on the integration of the subspace model, sensitivity encoding (for parallel imaging), and sparse modeling into one optimization problem; evaluations of strategies for regularizing the image model, adaptively enforcing model order, and for estimating sensitivity maps are also included.

The approach is evaluated through simulations on numerical cardiac phantoms and *in vivo* experiments in human, rat, and mouse subjects. Multiple cardiovascular applications are demonstrated: cine imaging, first-pass myocardial perfusion imaging, late gadolinium enhancement imaging, extracellular volume fraction mapping, and labeled immune cell imaging. Experimental results include human cine images up to 22 fps and 1.0 mm $\times$ 1.0 mm spatial resolution, mouse cine images up to 97 fps and 0.12 mm $\times$ 0.12 mm spatial resolution, rat images at 74 fps and 0.31 mm $\times$ 0.31 mm $\times$ 1.0 mm spatial resolution (capturing wall motion, first-pass myocardial perfusion, and late gadolinium enhancement in a single scan), multi-contrast rat images (for extracellular volume fraction mapping) up to 50 fps and 0.42 mm $\times$ 0.42 mm $\times$ 1.0 mm spatial resolution, and rat images at 98 fps and 0.16 mm $\times$ 0.16 mm spatial resolution (depicting labeled immune cells).

The end result is an imaging approach capable of ungated, whole-heart 3D cardiovascular MRI in high spatiotemporal resolution. Images can be obtained even for patients with irregular heartbeats, and both cardiac motion and aperiodic contrast dynamics can be imaged in a single scan. These capabilities should enhance the utility of cardiovascular MRI, allowing comprehensive evaluation of the heart.

To my family, whom I love.

Acknowledgments

This dissertation is only a reality thanks to the help and support of many people.

I owe a great debt of gratitude to my advisor Zhi-Pei Liang, whose guidance has been indispensable over the last six years. He has provided me with more opportunities than I can count and has taught me to constantly push myself. I could not ask for a better advisor. I also owe thanks to the other members of my thesis committee—Stephen Boppart, Minh Do, and Brad Sutton—whose suggestions and advice have shaped this dissertation.

I am also grateful to my hosts and collaborators from the Pittsburgh NMR Center for Biomedical Research at Carnegie Mellon University: Chien Ho, Kevin Hitchens, Yijen Wu, and Haosen Zhang; as well as from the Paul C. Lauterbur Research Center for Biomedical Imaging at the Shenzhen Institutes of Advanced Technology: Xin Liu, Guoxi Xie, and Xiang Feng. Their hospitality and support were a joy to experience.

I would also like to thank the students and postdocs with whom I spent time at the Beckman Institute for Advanced Science and Technology, particularly Cornelius Brinegar, Justin Haldar, Bo Zhao, Derin Babacan, Fan Lam, Chao Ma, Curtis Johnson, Maojing Fu, Diego Hernando, Mohammed Sheikh, Bryan Clifford, Qiang Ning, Hien Nguyen, Darren Pocci, Xi Peng, Xiaobo Qu, and Jingfei He. Their conversation and collaboration made for a wonderful environment.

Thanks also go to my past and present roommates Dan Fisher, Chelsea Fry, Dave Cohen, James Pikul, Erik Johnson, Dan Widing, and Varun Krishna—mostly for their friendship, but also for letting me turn our living room into a writing room and for feeding me when I

forgot to eat.

I would also like to acknowledge the agencies and organizations that provided the financial support necessary to carry out my research: the American Heart Association, the National Institutes of Health, the National Science Foundation, and the Department of Electrical and Computer Engineering at the University of Illinois of Urbana-Champaign.

Finally, I want to thank my family: the Wards and Christodoulous, my parents Athena and Christos, my brothers Paul and Mark, and my wife Andrea. I am only here because of all of you.

Table of Contents

List of Abbreviations

ACS	Autocalibration signal
BN	Brown Norway
CS	Compressed sensing
DFT	Discrete Fourier transform
ECG	Electrocardiogram
ECV	Extracellular volume fraction
EF	Ejection fraction
FA	Flip angle
FLASH	Fast low-angle shot
FOV	Field of view
IRI	Ischemic reperfusion injury
LAD	Left anterior descending
LCx	Left circumflex
LGE	Late gadolinium enhancement
LV	Left ventricular
MPIO	Micron-sized particles of iron oxide
MR	Magnetic resonance
MRI	Magnetic resonance imaging
NMR	Nuclear magnetic resonance
NRMS	Normalized root-mean-square

POD	Post-operational day
PS	Partial separability
PSF	Point spread function
RF	Radiofrequency
RMS	Root-mean-square
SNR	Signal-to-noise ratio
SPIO	Superparamagnetic iron oxide
SVD	Singular value decomposition
TPC	Time to peak concentration
TPSF	Transform point spread function
VARPRO	Variable projection

Chapter 1

Introduction

1.1 Problem statement

Fourier-encoded magnetic resonance (MR) data from a spatiotemporal cardiovascular image $\rho(\mathbf{r}, t)$ can be expressed as

$$d_q(\mathbf{k}, t) = \int_{\mathbf{r}} S_q(\mathbf{r}) \rho(\mathbf{r}, t) \exp(-i2\pi \mathbf{k} \cdot \mathbf{r}) \, d\mathbf{r}, \tag{1.1}$$

where $d_q(\mathbf{k}, t)$ is the $(\mathbf{k}, t)$-space signal collected from the qth receiver coil with sensitivity $S_q(\mathbf{r})$. The nature of MR data acquisition prevents simultaneous sampling at multiple $\mathbf{k}$-space locations: time is required to traverse $\mathbf{k}$-space, precluding dense sampling of $(\mathbf{k}, t)$-space at the $(\mathbf{k}, t)$ Nyquist rate. The associated challenge in acquiring high spatial resolution images quickly enough to resolve the motion of the heart is compounded by the curse of dimensionality, and leads to a difficult balance between:

- Temporal resolution/frame rate
- Spatial resolution

- Spatial dimensionality/spatial coverage
- Number of image contrasts
- Signal-to-noise ratio

The tradeoffs involved make time-resolved cardiovascular magnetic resonance imaging (MRI) of the heart in three spatial dimensions and/or with multiple contrasts particularly challenging.

The work in this dissertation is focused on developing a subspace approach to accelerate cardiovascular MRI. This approach involves a spatiotemporal image model exploiting the particular subspace structure of cardiovascular images; data acquisition strategies appropriate for integration of this subspace model, parallel imaging, and sparse modeling; and specialized image reconstruction integrating these three components. Results are presented for human, rat, and mouse subjects, including 3D imaging with multiple contrasts.

1.2 Motivation

Cardiovascular diseases are the leading cause of death worldwide, accounting for an estimated 30% of all deaths. Efforts to address cardiovascular diseases with technology can be traced back nearly 200 years to the invention of the stethoscope in 1816. The many successful technological advances since then have significantly transformed the detection, diagnosis, and treatment of cardiovascular diseases over the last two centuries. Cardiovascular imaging technology has enabled measurement and visualization of the structure and function of the beating heart and has become an indispensable part of cardiac health care. Several noninvasive cardiac imaging modalities are currently available to cardiologists, including echocardiography [2], X-ray computed tomography [3], positron emission tomography [4], single photon emission computed tomography [5], and magnetic resonance imaging [6]. Be-

cause of the particular properties of the nuclear magnetic resonance (NMR) phenomenon, MRI has a unique potential to allow multiple comprehensive cardiac assessments in a single integrated examination [7], such as measurement of blood flow and cardiac wall motion, assessment of tissue properties, etc. [8].

The applications of MRI in cardiovascular diagnosis are significant and numerous. MRI is the preferred modality for cardiac assessments including, but not limited to, detection and assessment of acute and chronic myocardial infarction, myocardial viability, cardiac chamber anatomy and function, evaluation of congenital heart disease, pulmonary regurgitation, pulmonary artery anatomy and flow, most anomalies of the arteries, and quantification of left ventricular and right ventricular function, mass, and volumes [9]. However, the conventional electrocardiogram (ECG)–gated techniques to perform these assessments require that the heart is in normal sinus rhythm and that patients hold their breath during imaging. As a result, these techniques are not effective for the large number of cardiac patients who are unable to perform breath-holding or who have cardiac arrhythmias; nor can they image the aperiodic contrast agent dynamics central to applications such as first-pass myocardial perfusion imaging.

Accelerating cardiovascular MRI opens many doors: higher image dimensionality, more spatial coverage, higher spatial resolution, freedom from ECG and respiratory control, the ability to image irregular heartbeats, more time to collect multiple contrasts for quantitative imaging, and the ability to image both cardiac motion and aperiodic contrast dynamics in a single scan. These developments would bring MRI one step closer to achieving its potential as the premier all-around imaging modality for cardiologists.

1.3 Overview of contributions

The main contributions in this dissertation are:

- An image model which represents the particular subspace structure of cardiovascular images
- A data acquisition strategy consisting of pulse sequence design, a novel **k**-space trajectory, and a sampling scheme appropriate for integrating the subspace model, parallel imaging, and sparse modeling
- Image reconstruction integrating the subspace model, sensitivity encoding, and sparse modeling
- Demonstration and evaluation of the approach on multiple cardiac applications in both human and small rodent subjects

The end result is an imaging method capable of performing whole-heart 3D cardiovascular MRI with enough speed to simultaneously image cardiac motion, respiratory motion, contrast agent dynamics, etc., all without the use of an ECG signal for triggering or gating. The resulting images allow comprehensive evaluation of the heart through the visualization and measurement of numerous cardiac structures and functions, even in subjects with irregular heartbeats (i.e., in subjects with cardiac arrhythmias) or with heart rates above 400 bpm (e.g., in small rodents).

1.4 Organization of the dissertation

The remainder of this dissertation is organized as follows.

Chapter 2 contains background on MRI, comprising a classical treatment of MR physics, signal detection, spatial encoding, image reconstruction, and image contrast. The chapter also includes brief descriptions of three signal processing approaches to accelerated MRI (low-rank imaging, parallel imaging, and sparse modeling/compressed sensing) and brief overviews of some cardiovascular MRI applications.

Chapter 3 describes a spatiotemporal image model designed to represent the particular subspace structure of cardiovascular images. This chapter defines subspace error metrics and includes analyses of a numerical cardiac phantom in the context of the proposed model.

Chapter 4 describes data acquisition approaches specifically designed to allow integration of: a) the subspace model described in the previous chapter, b) parallel imaging, and c) sparse modeling. Particular attention is paid to strategies for collecting auxiliary data used to define the temporal subspace containing the spatiotemporal image. These strategies cover pulse sequence design, **k**-space trajectory design, and sampling design.

Chapter 5 describes image reconstruction. The chapter presents an optimization problem which integrates the subspace model, sensitivity encoding (parallel imaging), and sparse modeling, and it describes an algorithm for solving the optimization problem. Evaluations of strategies for regularizing the image model and for estimating sensitivity maps are also included.

Chapter 6 presents 2D and 3D experimental results using the approach described in the previous chapters. Results from human, rat, and mouse subjects are included for multiple cardiac applications: cine imaging, first-pass myocardial perfusion imaging, late gadolinium enhancement imaging, extracellular volume fraction mapping, and labeled immune cell imaging.

Finally, Chapter 7 offers discussion and conclusions.

Chapter 2

Background

2.1 Magnetic resonance imaging

MRI produces images of an object by measuring and spatially localizing NMR signals. The NMR phenomenon is a quantum mechanical effect experienced by nuclei with nonzero spin (an intrinsic property of nuclei possessing an odd number of either protons or neutrons) in the presence of a magnetic field. Although spin is a quantum property, classical vector models can be used to describe the NMR phenomenon on the macroscopic scale of an MRI voxel (*volume element*, the three-dimensional equivalent of a pixel) containing a large ensemble of nuclei [11].

2.1.1 Nuclear magnetic resonance

The classical vector model conceptualizes a nucleus with nonzero spin as rotating about a central axis with angular momentum equal to the amount of spin. The rotation of a positively charged nucleus generates a magnetic field described by the magnetic dipole moment $\boldsymbol{\mu}$ (i.e., the nuclei function similarly to microscopic bar magnets). The bulk magnetization vector

$\mathbf{M} = \sum_i \boldsymbol{\mu}_i$ describes the total field generated by an ensemble of nuclei, the ith nucleus of which has magnetic moment $\boldsymbol{\mu}_i$. MRI experiments measure the bulk magnetization $\mathbf{M}$ of a nuclear spin system rather than the individual magnetic moments $\{\boldsymbol{\mu}_i\}_i$.

In order for $\mathbf{M}$ to be nonzero, the $\{\boldsymbol{\mu}_i\}_i$ must sum coherently. At thermal equilibrium and in absence of an external magnetic field, the $\{\boldsymbol{\mu}_i\}_i$ are randomly oriented, leading to a bulk magnetization $\mathbf{M} = \mathbf{0}$. However, in the presence of a strong, uniform, and static external magnetic field (conventionally notated as $\mathbf{B}_0 = B_0\hat{\mathbf{z}}$, where $\hat{\mathbf{z}}$ is the unit vector pointing in the z direction), the longitudinal (z) component of $\boldsymbol{\mu}_i$ (denoted as $\mu_{z,i}$) takes on a fixed value according to the energy state of the ith nucleus.

The nuclei have only $2I + 1$ possible energy states, where I is the spin quantum number. Because nuclear spin systems with $I = \frac{1}{2}$ (e.g., ^{1}H, ^{13}C, ^{19}F, ^{23}Na, ^{31}P) are the focus of the majority of MRI experiments, the remainder of our discussion in this section will be restricted to spin-$\frac{1}{2}$ systems, which have only two possible energy states: $E_\uparrow = -\frac{1}{2}\gamma\hbar B_0$ (the *spin-up* state) and $E_\downarrow = \frac{1}{2}\gamma\hbar B_0$ (the *spin-down* state), where γ is the nucleus-dependent gyromagnetic ratio (e.g., $\gamma = 2.675 \times 10^8$ rad/s/T for ^{1}H nuclei, corresponding to 42 MHz/T) and $\hbar$ is Planck's constant (6.6×10^{-34} J·s) over 2π. At thermal equilibrium, the transverse (x-y) components of each $\boldsymbol{\mu}$ (denoted in complex phasor notation as $\mu_{xy} = \mu_x + i\mu_y$) are still incoherent: only the $\{\mu_{z,i}\}_i$ sum coherently, leading to a bulk magnetization denoted as $\mathbf{M}_0 = M_z^0\hat{\mathbf{z}}$. The ratio of spin-up nuclei $N_\uparrow$ to spin-down nuclei $N_\downarrow$ is governed by the Boltzmann relationship

$$\frac{N_\uparrow}{N_\downarrow} = \exp\left(\frac{\Delta E}{KT_\mathrm{s}}\right) = \exp\left(\frac{\gamma\hbar B_0}{KT_\mathrm{s}}\right), \tag{2.1}$$

corresponding to first-order approximated bulk magnetization value of $M_z^0 = \frac{\gamma^2\hbar^2 B_0 N_\mathrm{s}}{4KT_\mathrm{s}}$, where K is the Boltzmann constant (1.38×10^{-23} J/K), T_s is the absolute temperature of the spin system, and $N_\mathrm{s} = N_\uparrow + N_\downarrow$ is the total number of spins.

A second effect of $\mathbf{B}_0$ on the spin system is nuclear precession. At thermal equilibrium, the classical model dictates that $\boldsymbol{\mu}$ precesses about $\mathbf{B}_0$ according to

$$\frac{d\boldsymbol{\mu}}{dt} = \gamma\boldsymbol{\mu} \times B_0\hat{\mathbf{z}}, \tag{2.2}$$

which describes motion such that $\mu_{xy}(t) = \mu_{xy}(0)\exp(-i\gamma B_0 t)$ and $\mu_z(t) = \mu_z(0)$. The angular frequency of this precession is therefore $\omega_0 = \gamma B_0$, which is the natural resonance frequency of the spin system (known as the Larmor frequency).

The behavior of the bulk magnetization $\mathbf{M}$ in the presence of a magnetic field $\mathbf{B}$ is governed by the Bloch equation:

$$\frac{d\mathbf{M}}{dt} = \gamma\mathbf{M} \times \mathbf{B} - \frac{M_x\hat{\mathbf{x}} + M_y\hat{\mathbf{y}}}{T_2} - \frac{(M_z - M_z^0)\hat{\mathbf{z}}}{T_1}, \tag{2.3}$$

where T_1 and T_2 are relaxation time constants characterizing the speed at which the spin system returns to thermal equilibrium, typically in the range of 300 to 2000 ms for T_1 and 30 to 150 ms for T_2. Note that for $\mathbf{B} = \mathbf{B}_0$ and at thermal equilibrium, Eq. (2.3) reduces to $d\mathbf{M}/dt = 0$, consistent with the previous description of the bulk magnetization vector as being static at thermal equilibrium.

One implication of Eq. (2.3) is that in order to induce a measurable M_{xy}, an additional time-varying field $\mathbf{B}_1(t)$ can be applied perpendicular to $\mathbf{B}_0$. $\mathbf{B}_1(t)$ is known as the radiofrequency (RF) pulse, and the forced precession of $\mathbf{M}$ about $\mathbf{B}_1(t)$ is referred to as excitation. From a classical perspective, a nonzero M_{xy} can be induced by establishing phase coherence between the moments $\{\mu_{xy,i}\}_i$, which can be done by exciting the spin system with a $\mathbf{B}_1(t)$ that rotates in the same direction and frequency as the $\{\mu_{xy,i}\}_i$, i.e., at the resonance frequency ω_0. From a quantum perspective, a nonzero M_{xy} can be induced by coherently transitioning the $\{\boldsymbol{\mu}_i\}_i$ from the low-energy (spin-up) state to the high-energy (spin-down) state. This requires that the energy E_{rf} from $\mathbf{B}_1(t)$ is equal to $\Delta E = \gamma\hbar B_0$. By Planck's law,

an RF pulse oscillating at frequency ω_{rf} carries energy $E_{\text{rf}} = \hbar\omega_{\text{rf}}$, so achieving $E_{\text{rf}} = \Delta E$ requires that $\omega_{\text{rf}} = \gamma B_0 = \omega_0$.

After the spin system has been excited (i.e., after $\mathbf{B}_1(t)$ has been turned off and the total field returns to $\mathbf{B} = \mathbf{B}_0$), the spin system enters a state known as free precession. Equation (2.3) dictates that the system will relax according to

$$M_{xy}(t) = M_{xy}(0) \exp\left(-\frac{t}{T_2}\right) \exp(-i\gamma B_0 t) \tag{2.4}$$

$$M_z(t) = M_z^0 \left[1 - \exp\left(-\frac{t}{T_1}\right)\right] + M_z(0) \exp\left(-\frac{t}{T_1}\right), \tag{2.5}$$

where $M_{xy}(0)$ and $M_z(0)$ are the transverse and longitudinal components, respectively, of $\mathbf{M}$ immediately following the removal of $\mathbf{B}_1(t)$. If the total field instead returns to $\mathbf{B} = (B_0 + \Delta B)\hat{\mathbf{z}}$, for $\Delta B \ll B_0$ such that M_z^0 is not significantly perturbed, Eq. (2.4) is replaced by

$$M_{xy}(t) = M_{xy}(0) \exp\left(-\frac{t}{T_2}\right) \exp(-i\gamma \Delta B t) \exp(-i\gamma B_0 t). \tag{2.6}$$

Equation (2.6) describes exponential decay from T_2 relaxation; in practice, spatial inhomogeneity of $\mathbf{B}_0$ induces phase coherence between magnetic moments, leading to quicker decay of $M_{xy}(t)$. This decay can be modeled as approximately exponential with constant T_2^*, resulting in

$$M_{xy}(t) = M_{xy}(0) \exp\left(-\frac{t}{T_2^*}\right) \exp(-i\gamma \Delta B t) \exp(-i\gamma B_0 t). \tag{2.7}$$

Although the effect of field inhomogeneity can be reversed with a second RF pulse generating a spin echo [12], this process is too slow for the purposes of dynamic cardiovascular imaging, so we will consider Eq. (2.7) in the rest of this chapter.

2.1.2 Signal detection

The precessing bulk magnetization $\mathbf{M}$ induces a magnetic flux through a receiver coil in the vicinity of the object, allowing detection of the NMR signal. Faraday's law of induction dictates that the voltage $V(t)$ induced in this coil is

$$V(t) = -\frac{\partial}{\partial t}\int_{\mathbf{r}} \mathbf{B}_{\mathrm{r}}(\mathbf{r}) \cdot \mathbf{M}(\mathbf{r}, t)\, d\mathbf{r}, \tag{2.8}$$

where $\mathbf{B}_{\mathrm{r}}(\mathbf{r})$ is the receive field of the detection coil at location $\mathbf{r}$ and $\mathbf{M}(\mathbf{r}, t)$ is the spatio-temporally varying bulk magnetization vector. Substituting Eq. (2.7) into Eq. (2.8) and recognizing that $M_z(\mathbf{r}, t)$ is slowly varying compared to $M_{xy}(\mathbf{r}, t)$, we obtain

$$\begin{aligned} V(t) = -\int_{\mathbf{r}} \left(-\frac{1}{T_2^*(\mathbf{r})} - i\gamma\Delta B(\mathbf{r}) - i\gamma B_0\right) B_{\mathrm{r},xy}^*(\mathbf{r}) M_{xy}(\mathbf{r}, 0) \\ \exp\left(-\frac{t}{T_2^*(\mathbf{r})}\right) \exp(-i\gamma\Delta B(\mathbf{r})t) \exp(-i\gamma B_0 t)\, d\mathbf{r}, \end{aligned} \tag{2.9}$$

where * denotes the complex conjugate.[1] Further recognizing that $\gamma B_0 \gg \gamma\Delta B$ and $\gamma B_0 \gg 1/T_2^*(\mathbf{r})$, the voltage simplifies to

$$V(t) = \int_{\mathbf{r}} i\omega_0 B_{\mathrm{r},xy}^*(\mathbf{r}) M_{xy}(\mathbf{r}, 0) \exp\left(-\frac{t}{T_2^*(\mathbf{r})}\right) \exp(-i\gamma\Delta B(\mathbf{r})t) \exp(-i\omega_0 t)\, d\mathbf{r}, \tag{2.10}$$

In practice, $V(t)$ is moved to a low-frequency band through signal demodulation, wherein $V(t)$ is multiplied by a reference signal and low-pass filtered. Assuming the reference signal

[1] Only the real part of Eq. (2.9) is valid. However, the offending imaginary part will cancel out during the later description of signal demodulation using a reference signal (e.g., $2\exp(i\omega_0 t)$). In the text, we keep both the real and imaginary terms of Eq. (2.9) and consider the demodulating signal $2\cos(\omega_0 t)$, since low-pass filtering $2\cos(\omega_0 t)s(t)\exp(-i\omega_0 t) = s(t) + s(t)\exp(-2i\omega_0 t)$ and $2\exp(i\omega_0 t)\mathrm{Re}\{s(t)\exp(-i\omega_0 t)\} = s(t) + s^*(t)\exp(2i\omega_0 t)$ both result in the same output $s(t)$.

is $2\cos(\omega_0 t) = \exp(-i\omega_0 t) + \exp(i\omega_0 t)$, then the signal $s(t)$ before low-pass filtering is:

$$\begin{aligned} s(t) &= \int_{\mathbf{r}} 2i\omega_0 \cos(\omega_0 t) B^*_{\mathrm{r},xy}(\mathbf{r}) M_{xy}(\mathbf{r},0) \exp\left(-\frac{t}{T_2^*(\mathbf{r})}\right) \exp(-i\gamma\Delta B(\mathbf{r})t) \exp(-i\omega_0 t)\, d\mathbf{r}, \\ &= \int_{\mathbf{r}} i\omega_0 B^*_{\mathrm{r},xy}(\mathbf{r}) M_{xy}(\mathbf{r},0) \exp\left(-\frac{t}{T_2^*(\mathbf{r})}\right) \exp(-i\gamma\Delta B(\mathbf{r})t) \exp(-2i\omega_0 t) \\ &\qquad + i\omega_0 B^*_{\mathrm{r},xy}(\mathbf{r}) M_{xy}(\mathbf{r},0) \exp\left(-\frac{t}{T_2^*(\mathbf{r})}\right) \exp(-i\gamma\Delta B(\mathbf{r})t)\, d\mathbf{r}. \end{aligned} \tag{2.11}$$

Low-pass filtering removes the first term, leaving only

$$s(t) = \int_{\mathbf{r}} i\omega_0 B^*_{\mathrm{r},xy}(\mathbf{r}) M_{xy}(\mathbf{r},0) \exp\left(-\frac{t}{T_2^*(\mathbf{r})}\right) \exp(-i\gamma\Delta B(\mathbf{r})t)\, d\mathbf{r}, \tag{2.12}$$

which can be digitally sampled.

In most modern MRI scanners, multiple receive coils are used to detect the signal, where each coil has a different receive field $\mathbf{B}_{\mathrm{r}}(\mathbf{r})$. For notational simplicity, we can define $S_q(\mathbf{r}) = CB^*_{\mathrm{r},xy}(\mathbf{r})$ as the sensitivity function for the qth receiver coil, where C is some constant of proportionality. The signal $s_q(t)$ from the qth channel of a system with Q receiver coils is then

$$s_q(t) = \int_{\mathbf{r}} \frac{i\omega_0}{C} S_q(\mathbf{r}) M_{xy}(\mathbf{r},0) \exp\left(-\frac{t}{T_2^*(\mathbf{r})}\right) \exp(-i\gamma\Delta B(\mathbf{r})t)\, d\mathbf{r}. \tag{2.13}$$

2.1.3 Spatial encoding

There are numerous ways to perform the spatial encoding necessary to perform MR imaging, but here we will specifically focus on the use of a spatially varying field $\Delta B(\mathbf{r})\hat{\mathbf{z}}$ to encode spatial location into the resonance frequency. Spatial encoding using gradient fields was introduced by Paul Lauterbur in [13], and has grown to become the most commonly used spatial encoding mechanism in MRI. The use of linear gradient fields leads to a popular and convenient Fourier interpretation [14, 15] as follows.

Consider the linear gradient field described by $\Delta B(\mathbf{r}) = G_x x + G_y y + G_z z$. If we define a vector $\mathbf{k}(t)$ as

$$\mathbf{k}(t) = \frac{\gamma}{2\pi} \begin{bmatrix} G_x t \\ G_y t \\ G_z t \end{bmatrix}, \tag{2.14}$$

then we can express Eq. (2.13) as

$$s_q(t) = \int_{\mathbf{r}} \frac{i\omega_0}{C} S_q(\mathbf{r}) M_{xy}(\mathbf{r}, 0) \exp\left(-\frac{t}{T_2^*(\mathbf{r})}\right) \exp(-i2\pi \mathbf{k}(t) \cdot \mathbf{r})\, d\mathbf{r}. \tag{2.15}$$

When the signal is measured over a short time period centered on $t = T_{\mathrm{E}}$ (the *echo time*), the relaxation effect during acquisition is negligible, yielding

$$d_q(\mathbf{k}(t)) = s_q(t) = \int_{\mathbf{r}} S_q(\mathbf{r}) \rho(\mathbf{r}) \exp(-i2\pi \mathbf{k}(t) \cdot \mathbf{r})\, d\mathbf{r} \tag{2.16}$$

$$= \int_{\mathbf{r}} \rho_q(\mathbf{r}) \exp(-i2\pi \mathbf{k}(t) \cdot \mathbf{r})\, d\mathbf{r}, \tag{2.17}$$

where the image is $\rho(\mathbf{r}) \propto M_{xy}(\mathbf{r}, 0) \exp(-T_{\mathrm{E}}/T_2^*(\mathbf{r}))$ and where $\rho_q(\mathbf{r}) = S_q(\mathbf{r})\rho(\mathbf{r})$. The relationship between $d_q(\mathbf{k})$ and $\rho_q(\mathbf{r})$ is then that of the Fourier transform, and the signal $s_q(t)$ can be interpreted as measuring $\rho_q(\mathbf{r})$ in the Fourier domain at spatial frequency $\mathbf{k}(t)$. This relationship also holds when Eq. (2.14) is more generally defined to handle time-varying gradients $G_x(t)$, $G_y(t)$, and $G_z(t)$:

$$\mathbf{k}(t) = \frac{\gamma}{2\pi} \begin{bmatrix} \int_0^t G_x(\tau)\, d\tau \\ \int_0^t G_y(\tau)\, d\tau \\ \int_0^t G_z(\tau)\, d\tau \end{bmatrix}. \tag{2.18}$$

Equations (2.14) and (2.18) describe Fourier encoding in three spatial dimensions (which we will refer to as *3D imaging*). Alternatively, one spatial dimension can be encoded by

applying a field gradient during excitation. Transmitting a narrow band RF pulse will then selectively excite a "slice" of the object, leaving only two additional dimensions to Fourier encode. We will refer to this slice-selective encoding scheme as *2D imaging*.

Equations (2.16) and (2.17) assume that the signal is measured over a window of time much shorter than the relaxation times of the imaged object. It may therefore initially appear tempting to use strong, quickly varying gradients to traverse **k**-space as efficiently as possible. However, there are hardware limits, physiological implications, and signal-to-noise ratio (SNR) concerns with large gradient amplitudes and slew rates. Instead, the $\{d_q(\mathbf{k})\}_{q=1}^{Q}$ are typically read out in short bursts, relying on multiple excitations of the spin system and multiple readouts to eventually cover **k**-space. As a result, MRI measurements are fairly slow, which is a major limitation—especially in the context of cardiovascular imaging.

2.1.4 Fourier image reconstruction

Based on Eq. (2.16) and Eq. (2.17), sampled **k**-space data $\{d_q(\mathbf{k}_m)\}_{m=1,q=1}^{M,Q}$ from Q coils at sampling locations $\{\mathbf{k}_m\}_{m=1}^{M}$ can be expressed as

$$d_q(\mathbf{k}_m) = \int_{\mathbf{r}} S_q(\mathbf{r})\rho(\mathbf{r}) \exp(-i2\pi\mathbf{k}_m \cdot \mathbf{r})\, d\mathbf{r} \tag{2.19}$$

$$= \int_{\mathbf{r}} \rho_q(\mathbf{r}) \exp(-i2\pi\mathbf{k}_m \cdot \mathbf{r})\, d\mathbf{r}. \tag{2.20}$$

The Nyquist–Shannon sampling theorem allows individual reconstruction of each $\rho_q(\mathbf{r})$ from sampled **k**-space data as long as each image is spatially bandlimited and the **k**-space sampling interval does not exceed the reciprocal of the bandwidth. Obviously, any real-world objects being imaged do not have infinite size, so $\rho(\mathbf{r})$, and by extension $\{\rho_q(\mathbf{r})\}_{q=1}^{Q}$, necessarily has finite spatial support and can fit inside a window having some widths W_x, W_y, and W_z.

Considering a noiseless, one-dimensional case for clarity, the Nyquist–Shannon sampling theorem implies that a support-limited $\rho_q(x)$ for which $\rho_q(x) = 0$ over $|x| > W_x/2$ can be

exactly recovered according to

$$\rho_q(x) = \Delta k \sum_{m=-\infty}^{\infty} d_q(m\Delta k) \exp(i2\pi m\Delta k x), \quad |x| < \frac{1}{2\Delta k}, \tag{2.21}$$

as long as $\Delta k < 1/W_x$. This image is defined over a spatial window of width $1/\Delta k$, referred to as the field-of-view (FOV). It is important to note that Eq. (2.21) requires knowledge of $\{d_q(m\Delta k)\}_{m=-\infty}^{\infty}$, which contains a countably infinite number of samples. In practice, infinite sampling is not achievable: time and gradient amplitude limitations dictate that $d_q(\mathbf{k})$ can only be sampled over a finite window in $\mathbf{k}$-space. Given M samples from k-locations $\{m\Delta k\}_{m=-M/2}^{M/2-1}$, we can instead obtain

$$\hat{\rho}_q(x) = \Delta k \sum_{m=-M/2}^{M/2-1} d_q(m\Delta k) \exp(i2\pi m\Delta k x), \quad |x| < \frac{1}{2\Delta k}. \tag{2.22}$$

Equation (2.22) can be interpreted as performing the operations in Eq. (2.21) after replacing the unknown samples of $\{d_q(m\Delta k)\}_{m=-\infty}^{\infty}$ with zeros, i.e., after multiplying the $\{d_q(m\Delta k)\}_{m=-\infty}^{\infty}$ by a rectangular window of width $M\Delta k$:

$$\hat{\rho}_q(x) = \Delta k \sum_{m=-\infty}^{\infty} d_q(m\Delta k) \,\mathrm{rect}\left(\frac{m\Delta k}{M\Delta k}\right) \exp(i2\pi m\Delta k x), \quad |x| < \frac{1}{2\Delta k}. \tag{2.23}$$

This yields

$$\hat{\rho}_q(x) = \rho_q(x) * M\Delta k \mathrm{sinc}(M\Delta k x), \tag{2.24}$$

where $*$ denotes convolution. The resulting point spread function (PSF) $M\Delta k\mathrm{sinc}(M\Delta k x)$ characterizes the imaging system and indicates that $\hat{\rho}_q(x)$ exhibits blurring (induced by the main lobe of the sinc function, which has effective width $1/M\Delta k = FOV/M$) and Gibbs ringing (induced by the side lobes of the sinc function). The main lobe effective width $\Delta x = FOV/M$ is known as the Fourier voxel width, which can be used to define the spatial

resolution of $\hat{\rho}_q(x)$; the results reported in this dissertation employ this definition of spatial resolution.

It is typical to only calculate $\hat{\rho}_q(x)$ at the voxel centers $\{n\Delta x\}_{n=-M/2}^{M/2-1}$:

$$\hat{\rho}_q(n\Delta x) = \Delta k \sum_{m=-M/2}^{M/2-1} d_q(m\Delta k)\exp(i2\pi m/M), \quad n = -M/2, -M/2+1, \cdots, M/2-1, \tag{2.25}$$

a form of the inverse discrete Fourier transform (DFT), which results in a digital image $\{\hat{\rho}_q(n\Delta x)\}_{n=-M/2}^{M/2-1}$. This discrete Fourier relationship between $\{\hat{\rho}_q(n\Delta x)\}_{n=-M/2}^{M/2-1}$ and $\{d_q(m\Delta k)\}_{m=-M/2}^{M/2-1}$ can be conveniently notated in matrix form as $\mathbf{d}_q = \boldsymbol{\mathcal{F}}_{\mathbf{r}}\hat{\boldsymbol{\rho}}_q$, where $\mathbf{d}_q$ is a vector consisting of $\{d_q(\mathbf{k}_m)\}_{m=1}^{M}$, $\boldsymbol{\mathcal{F}}_{\mathbf{r}}$ applies the DFT over each spatial dimension, and $\hat{\boldsymbol{\rho}}_q$ is a vectorized form of the image $\{\hat{\rho}_q(\mathbf{r}_n)\}_{n=1}^{M}$. Equation (2.25) can then be expressed as $\hat{\boldsymbol{\rho}}_q = \boldsymbol{\mathcal{F}}_{\mathbf{r}}^{-1}\mathbf{d}_q$, the solution to the inverse problem (i.e., $\hat{\boldsymbol{\rho}}_q = \arg\min_{\boldsymbol{\rho}_q} \|\mathbf{d}_q - \boldsymbol{\mathcal{F}}_{\mathbf{r}}\boldsymbol{\rho}_q\|_2$, where the ℓ_2-norm $\|\mathbf{x}\|_2 = \sqrt{\sum_i |x_i|^2}$).

The implications of Eq. (2.22) are that higher spatial resolution and/or increased spatial coverage require more $\mathbf{k}$-space samples, which in turn take more time to acquire. This tradeoff between spatial considerations and acquisition time has major consequences for imaging moving objects such as the heart. These consequences are elucidated by updating Eqs. (2.19) and Eq. (2.20) to additionally consider the passage of time:

$$d_q(\mathbf{k}_m, t_n) = \int_{\mathbf{r}} S_q(\mathbf{r})\rho(\mathbf{r}, t_n)\exp(-i2\pi\mathbf{k}_m\cdot\mathbf{r})\,d\mathbf{r} \tag{2.26}$$

$$= \int_{\mathbf{r}} \rho_q(\mathbf{r}, t_n)\exp(-i2\pi\mathbf{k}_m\cdot\mathbf{r})\,d\mathbf{r}, \tag{2.27}$$

where $\rho(\mathbf{r}, t)$ is the spatiotemporally varying image of a moving object, and $(\mathbf{k}, t)$-space is the sampling domain [16]. It is clear then that the timings of our samples matter in addition to their locations in $\mathbf{k}$-space, and that the additional time dimension exacerbates sampling requirements as per the curse of dimensionality. It is impractical to sample at the

$(\mathbf{k}, t)$ Nyquist rate associated with rapid cardiac and respiratory motions, especially when attempting 3D dynamic imaging. This challenge is the primary problem addressed by this dissertation.

2.1.5 Image contrast

To obtain Eq. (2.16) from Eq. (2.15), we defined the image $\rho(\mathbf{r}) \propto M_{xy}(\mathbf{r}, 0) \exp(-T_{\mathrm{E}}/T_2^*(\mathbf{r}))$. As a result, the images produced by MRI have signal intensity dependent on the transverse bulk magnetization immediately after RF excitation as well as the relaxation-induced signal decay during free precession.

The transverse bulk magnetization $M_{xy}(\mathbf{r}, 0)$ is a function of tissue parameters such as spin density and relaxation time constants. This function can take many forms depending on the sequence of RF and gradient pulses used; the ability to choose different pulse sequences and adjust their parameters is the source of MRI's uniquely flexible soft-tissue contrast. There are a great many pulse sequences providing a wide array of contrast options, but here we will focus on the use of the Fast Low-Angle SHot (FLASH) pulse sequence [17]. The FLASH sequence results in a post-excitation transverse magnetization of:

$$M_{xy}(\mathbf{r}, 0) = M_z^0(\mathbf{r}) \sin\alpha \frac{1 - \exp\left(-T_{\mathrm{R}}/T_1(\mathbf{r})\right)}{1 - \cos\alpha \exp\left(-T_{\mathrm{R}}/T_1(\mathbf{r})\right)}, \tag{2.28}$$

where T_{R} is the *repetition time* between RF pulses and α is the *flip angle* (FA). The flip angle describes how far $\mathbf{M}$ is rotated about $\mathbf{B}_1$ during forced precession; it can be calculated from $\mathbf{B}_1(t)$ (e.g., $\alpha = \gamma B_1 \tau_{\mathrm{p}}$ for a rectangular pulse of strength B_1 and duration τ_{p}). We then have

$$\rho(\mathbf{r}) \propto M_z^0(\mathbf{r}) \sin\alpha \frac{1 - \exp\left(-T_{\mathrm{R}}/T_1(\mathbf{r})\right)}{1 - \cos\alpha \exp\left(-T_{\mathrm{R}}/T_1(\mathbf{r})\right)} \exp\left(-\frac{T_{\mathrm{E}}}{T_2^*(\mathbf{r})}\right). \tag{2.29}$$

Equations (2.28) and (2.29) assume the spin system has been driven into a steady-state, i.e.,

that multiple repetitions of the pulse sequence have already been performed.

The parameters α, T_{R}, and T_{E} can be selected to manipulate contrast as appropriate for the specific imaging application. In cardiovascular imaging, speed considerations typically dictate a short T_{R} (on the order of 5 ms), but α and T_{E} can be manipulated to emphasize or de-emphasize T_1 and T_2^*, respectively. T_1-weighting is desirable for most of the applications considered in this dissertation, with the exception of labeled immune cell imaging, which employs T_2^*-weighting.

Exogenous contrast agents are also available to manipulate the relaxation rates of surrounding tissues, enhancing image contrast. These contrast agents typically consist of paramagnetic materials which shorten both T_1 and T_2^* of the surrounding protons, with the T_1 effect dominating for (relatively) low paramagnetism (i.e., low magnetic susceptibility) and the T_2^* effect dominating for high paramagnetism (i.e., high magnetic susceptibility). For example, contrast agents containing chelated Gd^{3+} ions can be injected into the bloodstream, reaching tissues through blood perfusion [18]. The seven unpaired electrons of Gd^{3+} facilitate T_1 relaxation (and to a lesser extent, T_2^*) increasing the relaxation rate $R_1 = 1/T_1$ proportional to the local concentration of contrast agent. Another injected contrast agent, particles of superparamagnetic iron oxide (SPIO), exhibits even stronger paramagnetism; these iron oxide particles locally perturb the magnetic field, shortening T_2^* (and to a lesser extent, T_1) of nearby protons [19].

Relaxation time constants can be quantified by fitting the image contrast function to multiple images collected with different pulse sequence parameters. For example, T_1 can be mapped from FLASH images $\{\hat{\rho}_i(\mathbf{r})\}_{i=1}^F$ collected with $F \geq 2$ different flip angles $\{\alpha_i\}_{i=1}^F$ and fixed T_{R} and T_{E}. Let $\mathbf{f}(A, T_1)$ be the vector of functions

$$f_i(A, T_1) = A \sin \alpha_i \frac{1 - \exp\left(-T_{\mathrm{R}}/T_1\right)}{1 - \cos \alpha_i \exp\left(-T_{\mathrm{R}}/T_1\right)}. \tag{2.30}$$

Maps of $T_1(\mathbf{r})$ and $A(\mathbf{r}) \propto M_z^0(\mathbf{r}) \exp\left(-T_\mathrm{E}/T_2^*(\mathbf{r})\right)$ can be recovered by voxel-by-voxel fitting of $\mathbf{f}(A, T_1)$ to each vector $\mathbf{v}_m$ constructed from elements $v_{m,i} = \hat{\rho}_i(\mathbf{r}_m)$:

$$\{A(\mathbf{r}_m), T_1(\mathbf{r}_m)\} = \arg\min_{A,T_1} \|\mathbf{v}_m - \mathbf{f}(A, T_1)\|_2. \tag{2.31}$$

The multivariable nonlinear minimization problem in Eq. (2.31) can be simplified by variable projection (VARPRO) [20], which parameterizes the linear elements of $\mathbf{f}(A, T_1)$ (i.e., the amplitude). The vector $\mathbf{f}$ can be rewritten as $\mathbf{f} = A\mathbf{g}(T_1)$, where

$$g_i(T_1) = \sin\alpha_i \frac{1 - \exp(-T_\mathrm{R}/T_1)}{1 - \cos\alpha_i \exp(-T_\mathrm{R}/T_1)}. \tag{2.32}$$

Equation 2.31 can then be expressed as

$$\{A(\mathbf{r}_m), T_1(\mathbf{r}_m)\} = \arg\min_{A,T_1} \|\mathbf{v}_m - A\mathbf{g}(T_1)\|_2, \tag{2.33}$$

which can be solved by parameterizing A as

$$\hat{A}_m(T_1) = \arg\min_{A} \|\mathbf{v}_m - A\mathbf{g}(T_1)\|_2 = \frac{\mathbf{g}(T_1)^H \mathbf{v}_m}{\|\mathbf{g}(T_1)\|_2^2} \tag{2.34}$$

and solving the single-variable nonlinear minimization problem

$$T_1(\mathbf{r}_m) = \arg\min_{T_1} \|\mathbf{v}_m - \hat{A}_m(T_1)\mathbf{g}(T_1)\|_2. \tag{2.35}$$

If desired, the solution can be constrained within a range of physically realistic values for T_1.

2.2 Signal processing approaches to accelerated MRI

Because of the speed limitations of MRI, a great deal of work has gone into developing physics- and hardware-based approaches focused on manipulating nuclear spins for fast data acquisition (e.g., [21–25]) within the Nyquist–Shannon framework. Fast-scanning technology is now a relatively mature area of research, giving way to solutions which leverage different signal processing frameworks for sub-Nyquist imaging within the sampling constraints of nuclear spin physics. Signal processing approaches to accelerated MRI (e.g., [26–44]) exploit signal properties beyond spatial bandlimitedness to allow image reconstruction from sparse $(\mathbf{k}, t)$-space samples. Three complementary approaches to sparse sampling are discussed in this section: low-rank imaging, parallel imaging, and sparse modeling/compressed sensing.

2.2.1 Low-rank imaging

Low-rank imaging exploits the fact that images in many applications (e.g., in cardiovascular [10], speech [45], pulmonary [46], and spectroscopic [47] imaging) have a high degree of correlation and therefore reside in a low-dimensional subspace. It is based on the partial separability (PS) model [38, 39], which represents dynamic MR images as

$$\rho(\mathbf{r}, t) = \sum_{\ell=1}^{L} \psi_\ell(\mathbf{r}) \varphi_\ell(t), \tag{2.36}$$

where L is the model order and where $\{\psi_\ell(\mathbf{r})\}_{\ell=1}^{L}$ and $\{\varphi_\ell(t)\}_{\ell=1}^{L}$ are some spatial and temporal functions, respectively. The Lth-order PS model in Eq. (2.36) implies that the Casorati

matrix

$$\mathbf{C}(\rho) = \begin{bmatrix} \rho(\mathbf{r}_1, t_1) & \rho(\mathbf{r}_1, t_2) & \dots & \rho(\mathbf{r}_1, t_N) \\ \rho(\mathbf{r}_2, t_1) & \rho(\mathbf{r}_2, t_2) & \dots & \rho(\mathbf{r}_2, t_N) \\ \vdots & \vdots & \ddots & \vdots \\ \rho(\mathbf{r}_M, t_1) & \rho(\mathbf{r}_M, t_2) & \dots & \rho(\mathbf{r}_M, t_N) \end{bmatrix},$$

which can be constructed for any Cartesian set of arbitrary indices $\{m\}_{m=1}^{M}$ and $\{n\}_{n=1}^{N}$, has a rank of no more than L [39, 41]. Given Eq. (2.36), the $(\mathbf{k}, t)$-space signal $d(\mathbf{k}, t) = \int_{\mathbf{r}} \rho(\mathbf{r}, t) \exp(-i2\pi\mathbf{k} \cdot \mathbf{r})\, d\mathbf{r}$ can be expressed as

$$d(\mathbf{k}, t) = \int_{\mathbf{r}} \sum_{\ell=1}^{L} \psi_\ell(\mathbf{r}) \varphi_\ell(t) \exp(-i2\pi\mathbf{k} \cdot \mathbf{r})\, d\mathbf{r} \tag{2.37}$$

$$d(\mathbf{k}, t) = \sum_{\ell=1}^{L} \left[\int_{\mathbf{r}} \psi_\ell(\mathbf{r}) \exp(-i2\pi\mathbf{k} \cdot \mathbf{r})\, d\mathbf{r} \right] \varphi_\ell(t), \tag{2.38}$$

or more succinctly,

$$d(\mathbf{k}, t) = \sum_{\ell=1}^{L} \tilde{\psi}_\ell(\mathbf{k}) \varphi_\ell(t), \tag{2.39}$$

where $\tilde{\psi}_\ell(\mathbf{k}) = \int_{\mathbf{r}} \psi_\ell(\mathbf{r}) \exp(-i2\pi\mathbf{k} \cdot \mathbf{r})\, d\mathbf{r}$. Therefore, Lth order partial separability is preserved in $(\mathbf{k}, t)$-space, and the $(\mathbf{k}, t)$-space Casorati matrix

$$\mathbf{C}(d) = \begin{bmatrix} d(\mathbf{k}_1, t_1) & d(\mathbf{k}_1, t_2) & \dots & d(\mathbf{k}_1, t_N) \\ d(\mathbf{k}_2, t_1) & d(\mathbf{k}_2, t_2) & \dots & d(\mathbf{k}_2, t_N) \\ \vdots & \vdots & \ddots & \vdots \\ d(\mathbf{k}_M, t_1) & d(\mathbf{k}_M, t_2) & \dots & d(\mathbf{k}_M, t_N) \end{bmatrix}$$

also has rank not exceeding L. Equations (2.36) and (2.39) permit a useful matrix factorization: $\mathbf{C}(\rho) = \mathbf{\Psi}\mathbf{\Phi}$ and $\mathbf{C}(d) = \tilde{\mathbf{\Psi}}\mathbf{\Phi}$, where $\mathbf{\Psi}_{ij} = \psi_j(\mathbf{r}_i)$, $\tilde{\mathbf{\Psi}}_{ij} = \tilde{\psi}_j(\mathbf{k}_i)$, and $\mathbf{\Phi}_{ij} = \varphi_i(t_j)$. Low-rank matrices have fewer real degrees of freedom than full-rank matrices: when $\text{rank}(\mathbf{C}(d)) = L$, the number of real degrees of freedom is reduced from $2MN$ to

$2(N + M - L)L$, providing an avenue for sparse sampling of dynamic images which are Lth-order partially separable.

It has been observed that dynamic images often exhibit spatiotemporal correlation [27]. When this correlation is very high, as it is in many imaging applications, the family of time functions at different voxels, $\{\rho(\mathbf{r}_m, t)\}_{m=1}^M$, are linearly dependent, implying that each entry can be expressed as a linear combination of $L < M$ temporal functions $\{\varphi_\ell(t)\}_{\ell=1}^L$; similarly, the family of static images at different times, $\{\rho(\mathbf{r}, t_n)\}_{n=1}^N$ are also linearly dependent, with each entry expressible as a linear combination of $L < N$ spatial functions $\{\psi_\ell(\mathbf{r})\}_{\ell=1}^L$. In these cases, the model in Eq. (2.36) clearly applies.

This low-order partial separability of $\rho(\mathbf{r}, t)$ or $d(\mathbf{k}, t)$ implies that the signal resides in a low-dimensional subspace. More specifically, in terms of its Casorati matrix representation, $\mathbf{C}(d)$ and $\mathbf{C}(\rho)$ belong, in general, to $\mathbb{C}^{M\times N}$, but because of their low-rankness induced by partial separability, they actually reside in an L-dimensional temporal subspace S_Φ, spanned by, for example, $\{[\varphi_\ell(t_1), \varphi_\ell(t_2), \ldots, \varphi_\ell(t_N)]\}_{\ell=1}^L$. This subspace property enables accelerated imaging with sparse sampling.

It has been shown that a low-rank $\mathbf{C}$ can be recovered by imposing rank constraints [48], for example by solving the optimization problem

$$\hat{\mathbf{C}}(d) = \arg\min_{\mathbf{C}(d)} \operatorname{rank}(\mathbf{C}(d)) \quad \text{s.t.} \quad \|\mathbf{d} - \mathcal{U}\{\mathbf{C}(d)\}\|_2 < \epsilon, \tag{2.40}$$

where the undersampling (or sparse sampling) operator $\mathcal{U}\{\cdot\}$ retains only the entries of $C(d)$ at the $\mathbf{k}$-space locations $\{(\mathbf{k}_j, t_j)\}_{j=1}^J$, where the jth element of the vector $\mathbf{d}$ contains the measured $d(\mathbf{k}_j, t_j)$, and where ϵ specifies some allowable data discrepancy [41]. Low-rank matrix recovery theory states that an $N \times N$ matrix $\mathbf{C}(d)$ with rank L can be recovered with high probability when $J \sim \mathcal{O}(NL \log N)$ [48, 49].

Matrix completion approaches solving problems such as Eq. (2.40) are tasked with deter-

mining both the spatial and temporal subspaces of $\mathbf{C}(\rho)$; the reconstruction problem becomes much simpler and requires even fewer samples when one of these subspaces is already known. For example, when the temporal subspace S_Φ is already known (and therefore an appropriate $\mathbf{\Phi}$ can be constructed), image reconstruction is instead equivalent to recovery of $\mathbf{\Psi}$ from measured data given $\mathbf{\Phi}$ [39]:

$$\hat{\mathbf{C}}(d) = \arg \min_{\mathbf{C}(d) \in S_\Phi} \|\mathbf{d} - \mathcal{U}\{\mathbf{C}(d)\}\|_2^2 , \tag{2.41}$$

or in another form,

$$\hat{\mathbf{\Psi}} = \arg \min_{\mathbf{\Psi}} \|\mathbf{d} - \mathcal{U}\{\boldsymbol{\mathcal{F}}_\mathbf{r} \mathbf{\Psi} \mathbf{\Phi}\}\|_2^2 , \tag{2.42}$$

where $\boldsymbol{\mathcal{F}}_\mathbf{r}$ applies the DFT over each spatial dimension. Predetermining S_Φ fixes many of the degrees of freedom in $\mathbf{C}(\rho)$ and $\mathbf{C}(d)$. This explicit-subspace low-rank reconstruction problem requires only $J = ML$ samples to be well posed. The final reconstructed image is calculated as $\hat{\mathbf{C}}(\rho) = \hat{\mathbf{\Psi}}\mathbf{\Phi}$.

The technical contributions in this dissertation are presented in the context of explicit-subspace low-rank imaging of the heart, so later sections will cover details such as strategies for determining S_Φ in greater detail.

2.2.2 Parallel imaging

Early approaches to multichannel MRI focused on the SNR benefits of combining the Q images $\{\hat{\rho}_q(\mathbf{r}, t)\}_{q=1}^Q$—each independently reconstructed from Fourier-encoded data sampled at the Nyquist rate—into the final reconstructed image $\hat{\rho}(\mathbf{r}, t)$. Accelerated parallel imaging approaches instead focus on utilizing the additional encoding power of the $\{S_q(\mathbf{r})\}_{q=1}^Q$ to allow reconstruction of $\hat{\rho}(\mathbf{r}, t)$ from sub-Nyquist data. It is illuminating to consider parallel imaging as an application of Papoulis's multichannel sampling theorem to MRI [50, 51],

wherein a single image $\rho(\mathbf{r}, t)$ is being passed through a bank of filters $\{S_q(\mathbf{r})\}_{q=1}^{Q}$, although this is not the context in which accelerated parallel MRI methods were originally developed (e.g., [52–58]).

It is well known that, under certain conditions, a bandlimited signal can be exactly recovered from sub-Nyquist measurements of the signal from multiple sensors. Consider that $\rho(\mathbf{r}, t)$ is spatially bandlimited to $[-W/2, W/2]$ and that $\{d_q(\mathbf{k}, t)\}_{q=1}^{Q}$ are the outputs from a bank of Q linear and $\mathbf{k}$-shift-invariant filters $\{S_q(\mathbf{r})\}_{q=1}^{Q}$. Papoulis's multichannel sampling theorem then states that $d(\mathbf{k}, t) = \int_{\mathbf{r}} \rho(\mathbf{r}, t) \exp(-i2\pi\mathbf{k} \cdot \mathbf{r})\, d\mathbf{r}$—and by extension $\rho(\mathbf{r}, t)$—can be recovered from samples of $\{d_q(\mathbf{k}, t)\}_{q=1}^{Q}$ taken at rate $\Delta\hat{k} = Q/W$ (i.e., a factor of Q above the Nyquist rate $\Delta k = 1/W$) using interpolation kernels $\{g_q(\mathbf{k})\}_{q=1}^{Q}$ derived from $\{S_q(\mathbf{r})\}_{q=1}^{Q}$ [51]. Considering only one spatial dimension for notational simplicity, this signal recovery can be expressed as

$$d(k, t) = \sum_{q=1}^{Q} \sum_{m=-\infty}^{\infty} d_q(mQ\Delta k, t) g_q(k - mQ\Delta k). \tag{2.43}$$

The interpolation kernels are defined as

$$g_q(k) = \int_{-W/2}^{W/2} G_q(x) \exp(i2\pi kx)\, dx, \tag{2.44}$$

where the $\{G_q(x)\}_{q=1}^{Q}$ are the solutions to $\mathbf{S}(x)\mathbf{G}(x) = Q\Delta k\mathbf{e}$, with

$$\mathbf{S}(x) = \begin{bmatrix} S_1(x) & S_2(x) & \cdots & S_q(x) \\ S_1\left(x - \frac{W}{Q}\right) & S_2\left(x - \frac{W}{Q}\right) & \cdots & S_q\left(x - \frac{W}{Q}\right) \\ \vdots & \vdots & & \vdots \\ S_1\left(x - (Q-1)\frac{W}{Q}\right) & S_2\left(x - (Q-1)\frac{W}{Q}\right) & \cdots & S_q\left(x - (Q-1)\frac{W}{Q}\right) \end{bmatrix},$$

$$\mathbf{G}(x) = \begin{bmatrix} G_1(x) \\ G_2(x) \\ \vdots \\ G_Q(x) \end{bmatrix}, \qquad \text{and } \mathbf{e} = \begin{bmatrix} 1 \\ 0 \\ \vdots \\ 0 \end{bmatrix}.$$

In order to achieve perfect reconstruction, a unique solution must exist for $\mathbf{S}(x)\mathbf{G}(x) = Q\Delta k\mathbf{e}$, implying that each $\mathbf{S}(x)$ must be full-rank for $\left(\frac{W}{2} - \frac{W}{Q}\right) < x < \frac{W}{2}$. In other words, the vectors $\left\{\left[S_q(x), S_q\left(x - \frac{W}{Q}\right), \cdots, S_q\left(x - (Q-1)\frac{W}{Q}\right)\right]^T\right\}_{q=1}^{Q}$ must be linearly dependent for every $\left(\frac{W}{2} - \frac{W}{Q}\right) < x < \frac{W}{2}$, a stronger condition than requiring the sensitivity functions $\{S_q(x)\}_{q=1}^{Q}$ to be linearly dependent.

In the situation with known $\{S_q(\mathbf{r})\}_{q=1}^{Q}$, $\hat{\rho}(\mathbf{r}, t)$ can be recovered in image space, e.g. by least-squares inversion of Eq. (2.26):

$$\hat{\boldsymbol{\rho}} = \arg\min_{\boldsymbol{\rho}} \sum_{q=1}^{Q} \|\mathbf{d}_q - \boldsymbol{\mathcal{U}}\boldsymbol{\mathcal{F}}_{\mathbf{r}}\mathbf{S}_q\boldsymbol{\rho}\|_2^2, \tag{2.45}$$

where $\boldsymbol{\mathcal{U}}$ only retains the input corresponding to $(\mathbf{k}, t)$-space sampling locations $\{(\mathbf{k}_j, t_j)\}_{j=1}^{J}$, $\mathbf{d}_q$ is the vector of measured data $\{d_q(\mathbf{k}_j, t_j)\}_{j=1}^{J}$, and $\mathbf{S}_q$ is a diagonal matrix which multiplies the image (vectorized as $\boldsymbol{\rho}$) by $S_q(\mathbf{r})$. Parallel imaging reconstruction methods of this class are commonly referred to as "image-space" or "SENSE-like" methods, after [55].

When $\{S_q(\mathbf{r})\}_{q=1}^{Q}$ are unknown, $\rho(\mathbf{r}, t)$ can be recovered using $\mathbf{k}$-space interpolation kernels analogous to the $\{g_q(\mathbf{k})\}_{q=1}^{Q}$ defined by Papoulis's sampling theorem. These kernels are typically learned from auxiliary data in the form of Nyquist-sampled data in the central region of $\mathbf{k}$-space. These auxiliary data are commonly referred to as the autocalibration signal (ACS). Methods of this class are commonly referred to as "$\mathbf{k}$-space" or "GRAPPA-like" methods, after [58].

Although Papoulis's multichannel sampling framework permits acceleration factors up to

Q, measurement noise, ACS requirements, and ill-conditioning of the reconstruction problem limit the practically achievable acceleration factor. As a result, acceleration factors well below Q are applied in practice. To achieve greater acceleration, parallel imaging can be applied jointly alongside complementary acceleration approaches such as low-rank imaging and compressed sensing.

2.2.3 Compressed sensing

Compressed sensing (CS) [59–63], sometimes called compressive sensing or compressive sampling, exploits the sparsity of signals to enable signal recovery from sub-Nyquist data. This sparse modeling approach has found useful application in MRI [30, 31] due to the compressibility of natural MR images in certain transform domains (e.g., the wavelet or finite-difference domains). A vector $\boldsymbol{\beta}$ is sparse (or compressible) when it has many zero (or negligible) entries; when $\boldsymbol{\beta} = \mathbf{T}\boldsymbol{\rho}$ is sparse, then the linear transform $T\{\cdot\}$ applied by $\mathbf{T}$ is said to sparsify the image $\rho(\mathbf{r}, t)$. In this scenario, an attractive solution to the image reconstruction problem is the $\hat{\boldsymbol{\rho}}$ which results in sparsest $\boldsymbol{\beta}$ (i.e., the solution for which $\boldsymbol{\beta}$ has the fewest nonzero entries) and which fits the measured data to within a tolerance ϵ:

$$\hat{\boldsymbol{\rho}} = \arg\min_{\boldsymbol{\rho}} \|\mathbf{T}\boldsymbol{\rho}\|_0 \quad \text{s.t.} \quad \|\mathbf{d} - \boldsymbol{\mathcal{U}}\boldsymbol{\mathcal{F}}_{\mathbf{r}}\boldsymbol{\rho}\|_2 < \epsilon, \tag{2.46}$$

where $\|\cdot\|_0$ is the ℓ_0 pseudonorm returning the number of nonzero entries in the argument vector, i.e., $\|\boldsymbol{\beta}\|_0 = \text{card}(\{i|\beta_i \neq 0\})$.

However, the use of an ℓ_0-norm in Eq. (2.46) results in a nonconvex optimization problem that is difficult to solve. A common surrogate for the ℓ_0-norm in Eq. (2.46) is the ℓ_1-norm $\|\boldsymbol{\beta}\|_1 = \sum_i |\beta_i|$, which has been shown to result in the same (or approximately same) solution

in many cases [60]:

$$\hat{\boldsymbol{\rho}} = \arg\min_{\boldsymbol{\rho}} \|\mathbf{T}\boldsymbol{\rho}\|_1 \quad \text{s.t.} \quad \|\mathbf{d} - \boldsymbol{\mathcal{U}}\boldsymbol{\mathcal{F}}_{\mathbf{r}}\boldsymbol{\rho}\|_2 < \epsilon, \tag{2.47}$$

or in its unconstrained form,

$$\hat{\boldsymbol{\rho}} = \arg\min_{\boldsymbol{\rho}} \|\mathbf{d} - \boldsymbol{\mathcal{U}}\boldsymbol{\mathcal{F}}_{\mathbf{r}}\boldsymbol{\rho}\|_2^2 + \lambda \|\mathbf{T}\boldsymbol{\rho}\|_1 . \tag{2.48}$$

An important theoretical result from compressed sensing literature is that when $\mathbf{T}\boldsymbol{\rho}$ is sparse, the performance of image reconstruction according to Eq. (2.48) can be guaranteed under certain conditions on $\boldsymbol{\mathcal{U}}\boldsymbol{\mathcal{F}}_{\mathbf{r}}\mathbf{T}^{-1}$. One such condition is that $\boldsymbol{\mathcal{U}}\boldsymbol{\mathcal{F}}_{\mathbf{r}}\mathbf{T}^{-1}$ obeys the restricted isometry property [64]. However, this property is difficult to verify for large problem sizes, so this section will instead focus on incoherence [65], which is easier to evaluate.

Because the actual support of $\boldsymbol{\beta} = \mathbf{T}\hat{\boldsymbol{\rho}}$ is not known beforehand—it is only known to be sparse—compressed sensing works best when the undersampling artifacts in the minimum-norm (zero-filled) solution

$$\hat{\boldsymbol{\rho}}_{\mathrm{MN}} = \arg\min_{\boldsymbol{\rho}} \|\boldsymbol{\rho}\|_2 \quad \text{s.t.} \quad \mathbf{d} = \boldsymbol{\mathcal{U}}\boldsymbol{\mathcal{F}}_{\mathbf{r}}\boldsymbol{\rho} \tag{2.49}$$

$$= \boldsymbol{\mathcal{F}}_{\mathbf{r}}^{-1}\boldsymbol{\mathcal{U}}^T\mathbf{d} \tag{2.50}$$

are incoherent and therefore do not obscure the true support of $\boldsymbol{\beta}$ (i.e., when the locations of large values of $\boldsymbol{\beta}_{\mathrm{MN}} = \mathbf{T}\hat{\boldsymbol{\rho}}_{\mathrm{MN}}$ correspond to the locations of nonzero values of $\boldsymbol{\beta}$), preferably resembling random additive noise.

Incoherence can be measured from the transform point spread functions (TPSFs) that collectively relate $\boldsymbol{\beta}_{\mathrm{MN}}$ and $\boldsymbol{\beta}$. Based on Eq. (2.50), we can see that $\boldsymbol{\beta}_{\mathrm{MN}} = \mathbf{T}\boldsymbol{\mathcal{F}}_{\mathbf{r}}^{-1}\boldsymbol{\mathcal{U}}^T\boldsymbol{\mathcal{U}}\boldsymbol{\mathcal{F}}_{\mathbf{r}}\mathbf{T}^{-1}\boldsymbol{\beta}$. The operator $\mathbf{P} = \mathbf{T}\boldsymbol{\mathcal{F}}_{\mathbf{r}}^{-1}\boldsymbol{\mathcal{U}}^T\boldsymbol{\mathcal{U}}\boldsymbol{\mathcal{F}}_{\mathbf{r}}\mathbf{T}^{-1}$ describes the TPSFs, i.e., P_{ij} describes the contribution of input β_j to output $\beta_{\mathrm{MN},j}$. It follows that large off-diagonal elements $\{P_{ij}\}_{i \neq j}$ risk

obscuring the true support of β and are undesirable. The metric $\max_{i \neq j} |P_{ij}|$ is therefore a useful measure of incoherence and can be used to guide selection of $T\{\cdot\}$ and sampling design of $\boldsymbol{\mathcal{U}}$ [31]. It has been established that random $(\mathbf{k}, t)$-space sampling typically results in incoherence alongside many sparsifying transforms (e.g., wavelet, or temporal Fourier), although other sampling strategies are useful as well [66].

2.3 Cardiovascular MRI applications

This section provides brief overviews of the applications which will be demonstrated through *in vivo* experiments in Chapter 6. There are many other applications of cardiovascular MRI not described here, many of which could also benefit from the accelerated imaging approach in this dissertation.

2.3.1 Cine imaging

Dynamic cine image sequences depict the structure and function of the heart, including the mechanical contraction, timing, and extent of wall motion and thickening, as well as the function of valves [6]. From these images, it is possible to perform a multitude of cardiac assessments. Global measures such as cardiac mass, blood volume, and ejection fraction can be measured from time-resolved images at different cardiac phases. Regional wall motion may be used to determine and localize abnormal tissue function: akinetic regions of the myocardium can be well visualized, helping to determine the extent of injury to the myocardium. Functional cine imaging may augment morphological imaging to better assess complex structural abnormalities and congenital heart defects by visualizing the motion of the blood and valves. Cine imaging may also be used to assess the mechanical activation of the heart, which may be important in understanding arrhythmias and in guiding treatment.

The classical cine imaging approach (known as cardiac gating) utilizes data acquired across

many heartbeats to reconstruct a single representative heartbeat. This operates on the assumption that each heartbeat is exactly the same, i.e., that the $\rho(\mathbf{r}, t)$ is periodic in time. This is achieved by using the ECG as a reference signal and instructing the subject to hold his or her breath; the data from multiple heartbeats are then combined to reconstruct a single representative heartbeat. However, many patients are unable to hold their breath adequately or have cardiac arrhythmias that violate the assumption of a periodic heartbeat, leading to poor image quality using gated methods. For this reason, it is often preferable to use ungated acceleration approaches—such as the one described in this dissertation—to produce high-spatial-resolution images quickly enough to resolve cardiac and respiratory motion without resorting to ECG triggering or breath holding.

2.3.2 Late gadolinium enhancement imaging

Late gadolinium enhancement (LGE) imaging is used to assess the viability of myocardial tissue (i.e., to distinguish irreversibly damaged myocardium from stunned myocardium after ischemia) [67]. The heart is typically imaged 10 to 20 min after the administration of gadolinium-based contrast agent into the blood stream. As described in Section 2.1.5, gadolinium-based contrast agents shorten the spin-lattice relaxation time constant T_1, boosting the signal when using T_1-weighting and brightening voxels in which the contrast agent is concentrated. After a period of time following administration of gadolinium, contrast agent concentration is higher in fibrous scar tissue than in normal myocardium, since the contrast agent in that tissue washes out at a slower rate. With T_1-weighted sequences, the normal myocardium appears dark and scar tissue appears bright, leading to positive contrast.

Like with cine imaging, it is customary to acquire data over multiple heartbeats using cardiac gating. This approach presumes that the subject has a stable heart period and is able to reliably hold their breath, but it is often difficult (or for some unhealthy subjects, impossible) to fulfill this requirement. Ungated accelerated approaches are therefore desirable

for LGE imaging as well.

2.3.3 Extracellular volume fraction mapping

Extracellular volume fraction (ECV) mapping is a quantitative extension to LGE based on quantification of myocardial T_1 both before and after administration of contrast agent [68]. While qualitative T_1-weighted imaging such as LGE imaging can reveal regional differences in the T_1 of tissue, it is more challenging to detect abnormalities when there is a global shift in T_1. In this instance, there will be no regional differences or spatial contrast observed. To detect diseases that result in a global abnormality (i.e., a uniform contrast change), it is required to quantify the actual change in T_1 resulting from the injection of contrast agent.

As discussed in Section 2.1.5, it is possible to quantify T_1 by collecting multiple images with different pulse sequence parameters (and therefore different T_1-weightings). The T_1 values can then be extracted by fitting the appropriate image contrast equation to the measured images, generating parameter maps. Once T_1 maps (and therefore maps of the spin-lattice relaxation rate $R_1 = 1/T_1$) have been acquired, the ECV in myocardial voxels can be calculated according to

$$\mathrm{ECV} = (1-h)\frac{R_{1,\mathrm{post}} - R_{1,\mathrm{pre}}}{R_{1,\mathrm{blood,post}} - R_{1,\mathrm{blood,pre}}}, \tag{2.51}$$

where h is the hematocrit (calculated from a blood sample drawn from the subject), and $R_{1,\mathrm{blood}}$ is the R_1 value of blood (estimated from the left ventricular blood pool in the R_1 maps) [68].

This objective, quantitative measurement of myocardial tissue properties provides a means to perform serial measurements which may be used to evaluate the effectiveness of therapies in the long term. Parametric mapping places additional demands on accelerated imaging to achieve the desired image quality and spatiotemporal resolution in the presence of motion,

as even more images are required to be collected.

2.3.4 Myocardial perfusion imaging

First-pass myocardial perfusion imaging measures blood flow through the myocardium by capturing the wash-in and wash-out of a gadolinium-based contrast agent or other contrast mechanism [69]. This has potential for myocardial tissue assessment and early detection of coronary artery disease (among other applications). During wash-in, regions with normal flow will appear brighter than regions with reduced flow, as the contrast agent reaches healthy regions first. Perfusion measurements can be extracted from the signal intensity curve $|\rho(\mathbf{r}_m, t)|$ for any voxel $\mathbf{r}_m$ inside the myocardium.

Myocardial perfusion contrast dynamics are transient and therefore aperiodic, precluding ECG gating as an imaging strategy. Instead, it is common to use the ECG as a reference to trigger quick acquisition of a low-resolution image each time the heart returns to a certain phase of the cardiac cycle [70]; cardiac motion is not represented in the resulting images. In 2D imaging with ECG triggering, different slices are triggered at different cardiac phases, leading to phase mismatches between slices. Volumetric 3D imaging does not have this problem (and further benefits from the absence of slice gaps and no need for preparation pulses), but 3D acquisition is very technically challenging, requiring a great deal of acceleration.

2.3.5 Labeled immune cell imaging

Labeled immune cell imaging detects the accumulation of magnetically labeled cells, providing a powerful tool for biomedical research, cellular medicine, and diagnosis [71]. Immune cells are involved in many important physiological and pathological conditions in the heart, such as in atherosclerosis, inflammation, coronary heart disease, and organ rejection, among others. Macrophages and monocytes can be labeled in circulation by direct intravenous

injection of biologically compatible SPIO particles; these cells then migrate to the site of injury, infection, or inflammation.

MRI of SPIO-labeled immune cells can be performed through T_2^*-weighted cine imaging. The SPIO particles induce local magnetic field inhomogeneity, shortening the T_2^* of the surrounding water and providing a mechanism to generate negative image contrast. However, the late echo time required for T_2^* weighting leads to long pulse sequences and inefficient data acquisition, making the difficult task of free-breathing, ungated cardiac imaging even more challenging. There is a great need for accelerated cardiac imaging methods, particularly those which are specifically designed for T_2^*-weighted imaging.

Chapter 3

Spatiotemporal Image Model

3.1 Cardiovascular PS model

The basic PS model assumes that the entire image shares a common temporal subspace of the same dimension. However, cardiac and non-cardiac anatomy undergo different types of motion, so the spatiotemporal signal changes can be more efficiently represented by a regional PS model as:

$$\rho(\mathbf{r},t) = \begin{cases} \sum_{\ell=1}^{L_1} \psi_\ell(\mathbf{r})\phi_\ell(t), & \text{if } \mathbf{r} \notin \Omega \\ \sum_{\ell=1}^{L_2} \psi_\ell(\mathbf{r})\varphi_\ell(t), & \text{if } \mathbf{r} \in \Omega \end{cases}, \tag{3.1}$$

where $\{\varphi_\ell(t)\}_{\ell=1}^{L_2}$ and $\{\phi_\ell(t)\}_{\ell=1}^{L_1}$ span the temporal subspace for the cardiac region (Ω) and the non-cardiac region, respectively [10, 72]. In practice, we may further assume that $\text{span}\{\varphi_\ell(t)\}_{\ell=1}^{L_2} \supset \text{span}\{\phi_\ell(t)\}_{\ell=1}^{L_1}$ since any background motion (e.g., respiratory motion) also

affects the cardiac region. Therefore, we can rewrite Eq. (3.1) as

$$\rho(\mathbf{r},t) = \begin{cases} \sum_{\ell=1}^{L_1} \psi_\ell(\mathbf{r})\varphi_\ell(t), & \text{if } \mathbf{r} \notin \Omega \\ \sum_{\ell=1}^{L_2} \psi_\ell(\mathbf{r})\varphi_\ell(t), & \text{if } \mathbf{r} \in \Omega \end{cases}, \tag{3.2}$$

where it is assumed that $L_2 \geq L_1$. Equation (3.2) implies that $\{\varphi_\ell(t)\}_{\ell=1}^{L_2}$ span the entire temporal subspace for $d(\mathbf{k},t)$ or $\rho(\mathbf{r},t)$, while temporal signal changes in non-cardiac regions live only in the subspace spanned by $\{\varphi_\ell(t)\}_{\ell=1}^{L_1}$. The basic PS model corresponds to $L_1 = L_2$.

Given a measured $(\mathbf{k},t)$-space data set $\{d(\mathbf{k}_m,t_n)\}_{m=1,n=1}^{M,N}$, we can express the singular value decomposition (SVD) of its Casorati matrix $\mathbf{C}(d)$ as

$$\mathbf{C}(d) = \sum_{\ell=1}^{L} \sigma_\ell \mathbf{u}_\ell \mathbf{v}_\ell^H, \tag{3.3}$$

where σ_ℓ is the ℓth singular value, and where $\mathbf{u}_\ell$ and $\mathbf{v}_\ell$ are the ℓth left and right singular vectors, respectively. Clearly, we have $L = L_2$. The dominant right singular vectors tend to capture the "low-frequency" (e.g., respiratory) temporal signal changes, while the less-significant "high-frequency" components represent mainly cardiac signal changes, as illustrated in Figs. 3.1 and 3.2. This can be taken advantage of when constructing the PS model in Eq. (3.2): a set of temporal basis functions for $\rho(\mathbf{r},t)$ can be defined in the form $\hat{\varphi}_\ell(t_n) = \mathbf{V}_{n\ell}^*$ (note that the ℓth column of $\mathbf{V}$ is equal to $\mathbf{v}_\ell$), already partitioned according to the assumptions in Eq. (3.2).

The SVD of $\mathbf{C}(\rho)$ for a numerical cardiac phantom (constructed as described in Section 3.2.3) yields further insight into the subspace structure of cardiovascular images. As ℓ increases, signal in the spatial eigenmaps $\{\mathbf{u}_\ell\}_{\ell=1}^{L}$ becomes more concentrated in the cardiac region than in the non-cardiac region. Figure 3.2 shows image representations of $|\mathbf{u}_\ell|$ and $\mathrm{Re}\{\mathbf{v}_\ell\}$ for $\ell = 1, 5, 19$ from the cardiac phantom. Each eigenmap contains cardiac signal;

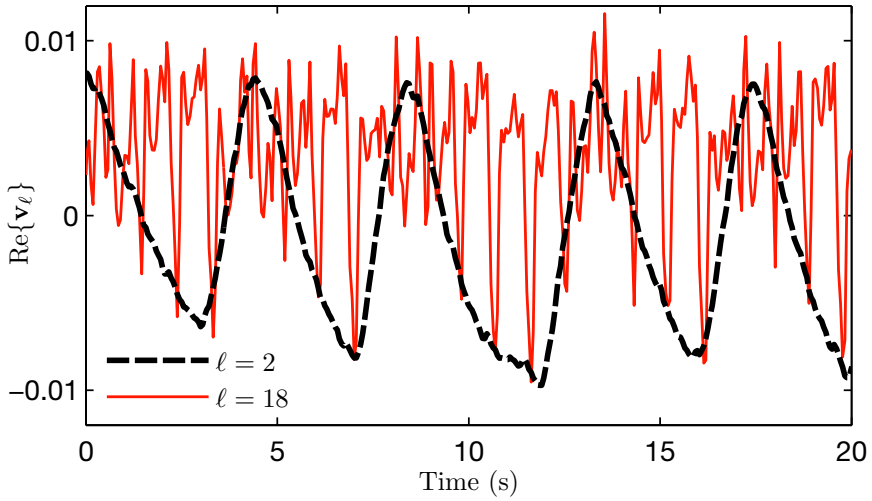

Figure 3.1: Separation of respiratory and cardiac signal changes in the right singular vectors of a typical human cardiac MR data set. The Casorati matrix was created from data measured at a limited number of **k**-space locations. The figure plots the real parts of $\mathbf{v}_2$ and $\mathbf{v}_{18}$, respectively. Both vectors are complex, but only the real parts are shown for the purposes of simplicity. As can be seen, $\mathbf{v}_2$ contains the low-frequency signal changes (related to respiratory motion), whereas $\mathbf{v}_{18}$ captures faster cardiac motion.

however, by $\ell = 19$, the non-cardiac signal is highly sparse, limited to only a few voxels over the vasculature.

3.2 Simulation analysis

3.2.1 Error metrics

Before presenting analyses and results, it is useful to establish criteria for evaluating model and subspace accuracy. Here, the error between the estimated subspace $S_{\hat{\Phi}}$ and the true subspace S_Φ is quantified in terms of E_{proj}, the error which results from projecting $\mathbf{C}(\rho)$ onto $S_{\hat{\Phi}}$ (i.e., the distance between $\mathbf{C}(\rho)$ and $S_{\hat{\Phi}}$), as well as E_{rec}, the error which results from reconstructing $\mathbf{C}(\rho) \in S_{\hat{\Phi}}$ from noisy sparse data. E_{proj} is defined as the normalized

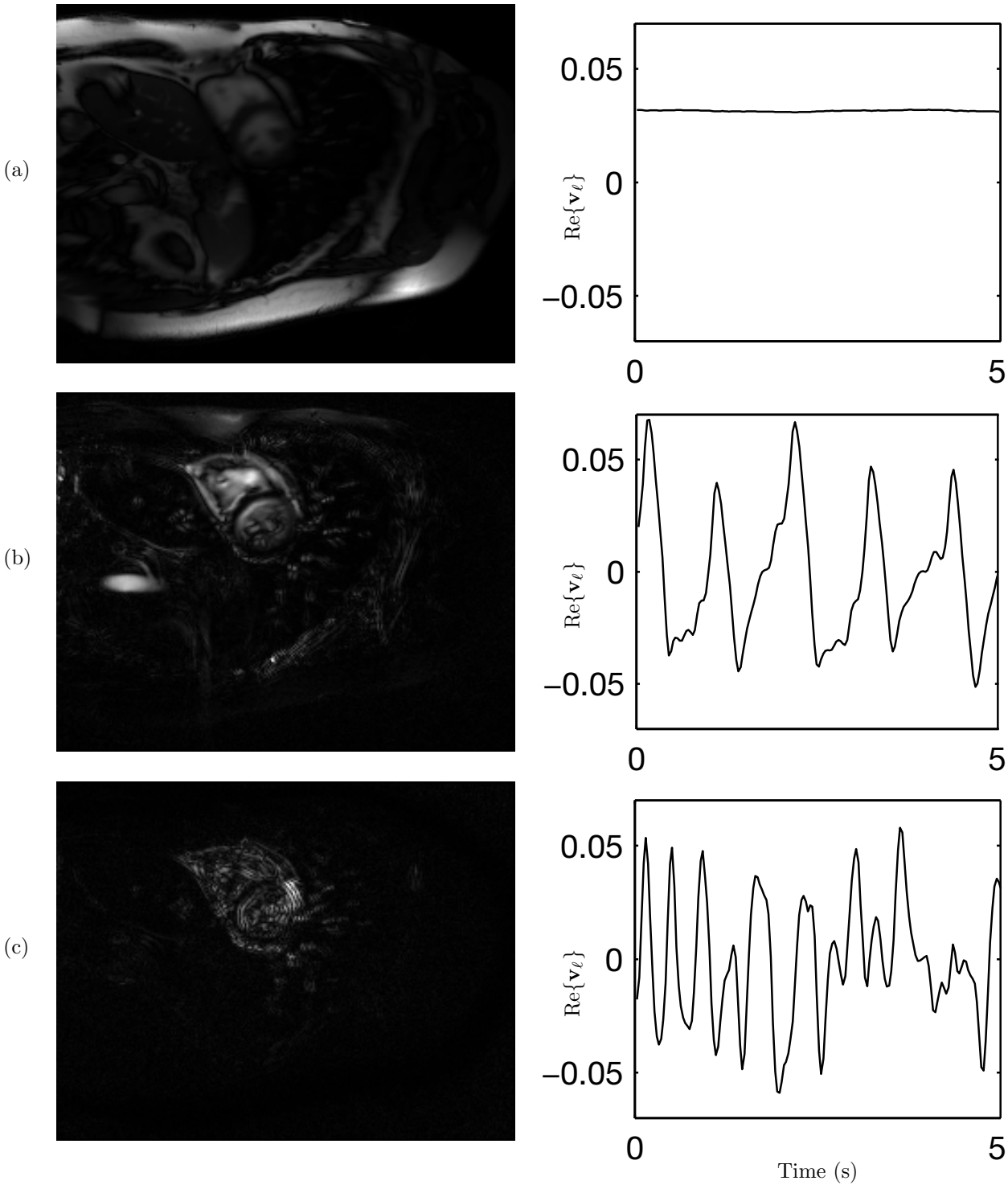

Figure 3.2: Representations of $|\mathbf{u}_\ell|$ and $\mathrm{Re}\{\mathbf{v}_\ell\}$ from $\mathbf{C}(\rho)$ for (a) $\ell = 1$, (b) $\ell = 5$, and (c) $\ell = 19$.

root-mean-square (NRMS) error of $\hat{\mathbf{C}}_{\text{proj}}(\rho) = \mathbf{C}(\rho)\hat{\mathbf{\Phi}}^H\hat{\mathbf{\Phi}} = \arg\min_{\mathbf{X}\in S_{\hat{\Phi}}} \|\mathbf{C}(\rho) - \mathbf{X}\|_F$:

$$E_{\text{proj}}(\hat{\mathbf{\Phi}}) = \frac{\|\mathbf{C}(\rho) - \hat{\mathbf{C}}_{\text{proj}}(\rho)\|_F}{\|\mathbf{C}(\rho)\|_F} = \frac{\|\mathbf{C}(\rho)(\mathbf{I} - \hat{\mathbf{\Phi}}^H\hat{\mathbf{\Phi}})\|_F}{\|\mathbf{C}(\rho)\|_F}.$$

E_{rec} is the NRMS error of $\hat{\mathbf{C}}_{\text{rec}}(\rho)$, the reconstruction from noisy sparse imaging data $\mathbf{d} = \mathcal{U}\{\mathbf{C}(\rho)\} + \mathbf{\eta}$ (where $\mathbf{\eta}$ is the noise vector):

$$E_{\text{rec}}(\hat{\mathbf{\Phi}}) = \frac{\|\mathbf{C}(\rho) - \hat{\mathbf{C}}_{\text{rec}}(\rho)\|_F}{\|\mathbf{C}(\rho)\|_F}.$$

E_{proj} quantifies the optimal reconstruction (in the Frobenius norm sense) of $\mathbf{C}(\rho)$ given $S_{\hat{\Phi}}$; E_{rec} quantifies the error of a practically achievable reconstruction of $\mathbf{C}(\rho)$.

3.2.2 Numerical cardiac phantom

The cardiac phantom used for the analyses in this chapter was generated from *in vivo* human short axis MR cardiac images and features variable-rate cardiac and respiratory motion. The images were collected using retrospective ECG and respiratory gating, resulting in images of a single representative cardiac cycle. These images were looped and time-warped to simulate a variable-rate heartbeat, and then spatially deformed to simulate variable-rate respiration. The phantom image sequence contains one complex-valued 200×256 frame every 3 ms over a duration of 30 s.

3.2.3 Subspace structure

This section contains an analysis of subspace structure in a numerical cardiovascular phantom $\rho(\mathbf{r}, t)$. This analysis demonstrates the utility of the model in Eq. (3.2) when combined with the proposed data acquisition/subspace definition scheme using the SVD of auxiliary data $\mathcal{D}_{\text{nav}}$ to define $\hat{\mathbf{\Phi}}$ (as will be detailed in Section 4.1).

In the following paragraphs, $\mathbf{C}_\Omega$ and $\mathbf{C}_{\not\Omega}$ are denoted as the mutually exclusive submatrices of $\mathbf{C}(\rho)$ which represent the cardiac and non-cardiac regions of the image, respectively. Formally, these submatrices are described as $\mathbf{C}_\Omega = [\mathbf{C}(\rho)_{mn}]_{m|\mathbf{r}_m\in\Omega,n=1,2,\ldots,N}$ and $\mathbf{C}_{\not\Omega} = [\mathbf{C}(\rho)_{mn}]_{m|\mathbf{r}_m\notin\Omega,n=1,2,\ldots,N}$. The SVDs of $\mathbf{C}_\Omega$ and $\mathbf{C}_{\not\Omega}$ yield Eckart–Young subspaces [73], the bases $\mathbf{V}_\Omega$ and $\mathbf{V}_{\not\Omega}$ for which would yield the lowest possible projection error for each submatrix:

$$\mathbf{V}_\Omega^H = \arg\min_{\mathbf{\Phi}} E_{\text{proj},\Omega}(\mathbf{\Phi}) = \arg\min_{\mathbf{\Phi}} \frac{\|\mathbf{C}_\Omega(\mathbf{I}-\mathbf{\Phi}^H\mathbf{\Phi})\|_F}{\|\mathbf{C}_\Omega\|_F} \tag{3.4}$$

$$\mathbf{V}_{\not\Omega}^H = \arg\min_{\mathbf{\Phi}} E_{\text{proj},\not\Omega}(\mathbf{\Phi}) = \arg\min_{\mathbf{\Phi}} \frac{\|\mathbf{C}_{\not\Omega}(\mathbf{I}-\mathbf{\Phi}^H\mathbf{\Phi})\|_F}{\|\mathbf{C}_{\not\Omega}\|_F}. \tag{3.5}$$

Here we compare the approximation errors resulting from different low-rank approximations of $\mathbf{C}_\Omega^H$ and $\mathbf{C}_{\not\Omega}^H$, comparing $E_{\text{proj},\Omega}(\mathbf{V}_\Omega^H)$ and $E_{\text{proj},\not\Omega}(\mathbf{V}_{\not\Omega}^H)$ (projection error using the optimal subspaces) to $E_{\text{proj},\Omega}(\hat{\mathbf{\Phi}})$ and $E_{\text{proj},\not\Omega}(\hat{\mathbf{\Phi}})$ (projection error using practically achievable estimated subspaces). The matrix $\mathbf{\Phi}$ was constructed from the SVD of $\mathcal{D}_{\text{nav}}$, which was collected using $N_{\text{d}} = 5$. Figure 3.3 shows the corresponding NRMS error values E_{proj} as a function of model order L.

In Fig. 3.3, the error curves from Eckart–Young approximation are an indicator of the intrinsic rank properties of each region. It is evident that very low-order representations of the non-cardiac region can match the accuracy of moderately low-order representations of the cardiac region. Here, a rank-6 approximation of $\mathbf{C}_{\not\Omega}$ is as accurate as a rank-54 approximation of $\mathbf{C}_\Omega$ (as measured by NRMS error). When compared to the ideal regional subspaces, there only is a small loss of accuracy associated with use of the suboptimal estimate $\hat{\mathbf{\Phi}}$: the relatively small size of this loss suggests that the intrinsic rank properties of cardiovascular images can be successfully and practically exploited using the nested subspace strategy represented in Eq. (3.2) as combined with the proposed data acquisition/subspace definition scheme using the SVD of $\mathcal{D}_{\text{nav}}$ to define $\hat{\mathbf{\Phi}}$.

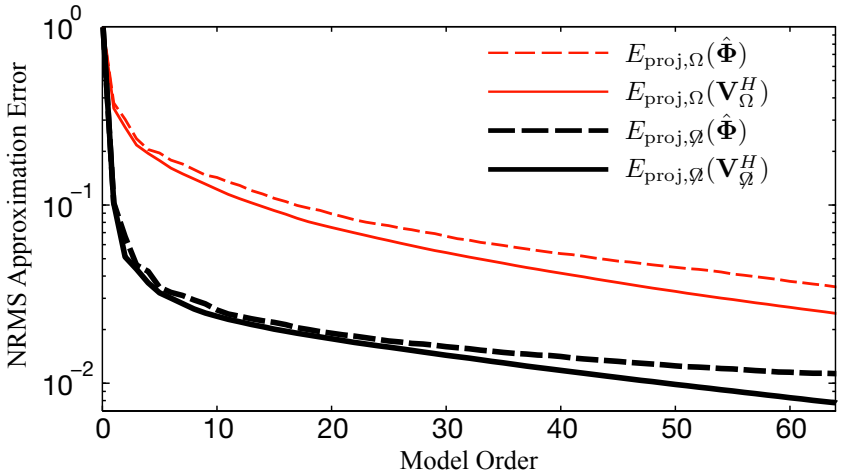

Figure 3.3: NRMS error of low-rank approximations from projecting the cardiac and non-cardiac matrices $\mathbf{C}_\Omega^H$ and $\mathbf{C}_{\not\Omega}^H$ onto different temporal subspaces. In both cases, the non-cardiac region can be estimated with a low-order model as accurately as the cardiac region can with a higher-order model.

3.2.4 Model order and cardiac function

This section investigates the basic relationship between model order and cardiac function as measured by left ventricular (LV) ejection fraction (EF). LVEF measures the volume of blood ejected in one heartbeat, expressed as a percentage of total LV capacity; it is one of the most predictive measurements of cardiac risk [74]. Because increased deformation of the cardiac wall induces greater EF, the following analysis also serves to investigate PS model order as a function of image deformation distance.

The numerical cardiac phantom described in Section 3.2.2 was regenerated for EF = 25% (severely reduced), 50% (low end of normal), 75% (high end of normal). Figure 3.4 shows (a) the end-diastole frame shared across variations, as well as (b-d) the end-systole frames and (e-g) spatiotemporal slices for each variation of the phantom, in order of ascending EF.

Figure 3.5 shows $E_{\mathrm{proj}}(\mathbf{V}^H)$ (i.e., the error curves from Eckart–Young approximation) over a range of model orders for each of the three scenarios. As might be expected, reduced EF corresponds to a "simpler" image in the sense that the phantoms with lower EF can be represented with slightly more accuracy at any given model order. Overall, the error curves

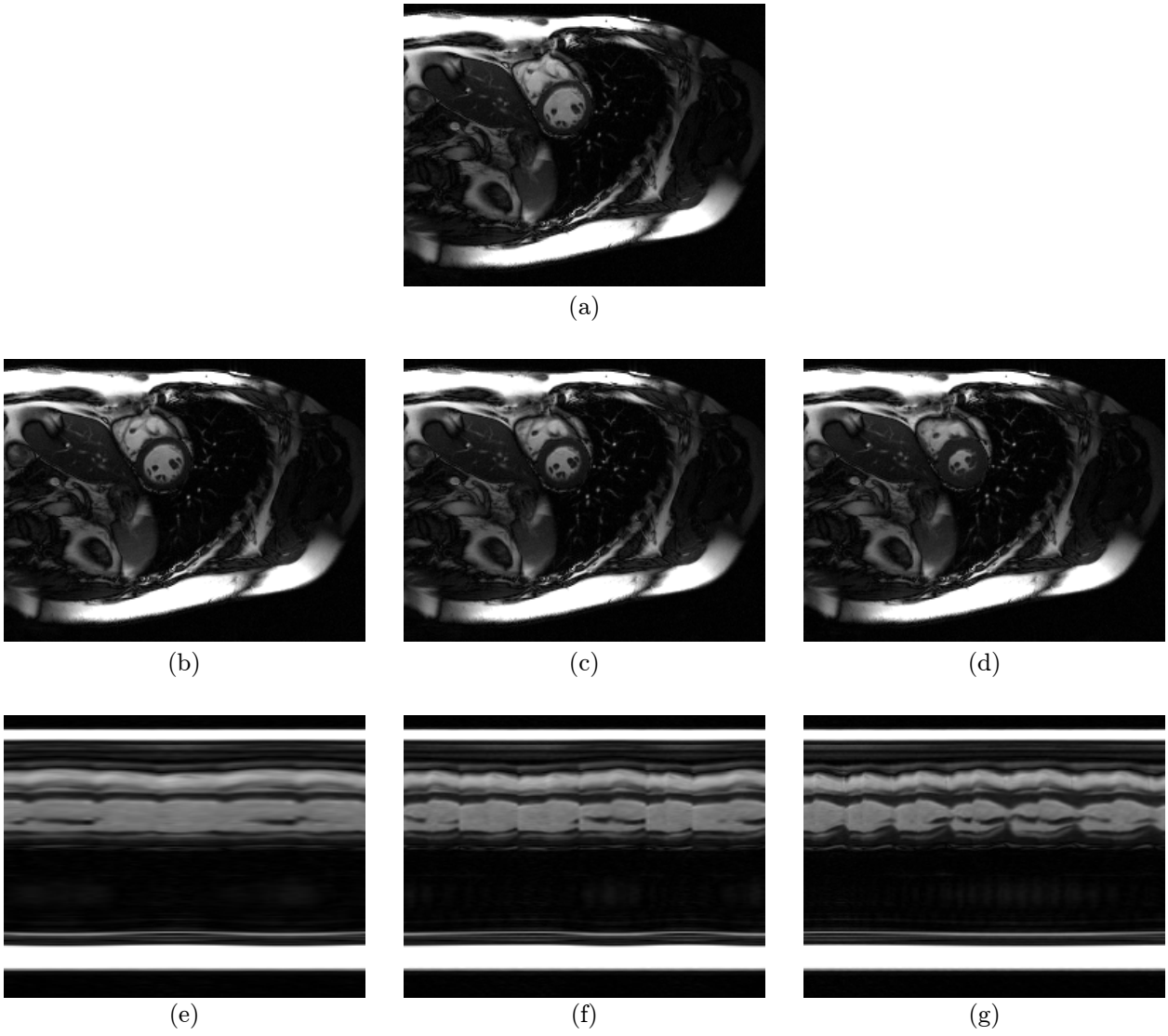

Figure 3.4: (a) The end-diastole frame shared across variations; the end-systole frames from the phantom variations with (b) EF = 25%, (c) EF = 50%, and (d) EF = 75%; and spatiotemporal slices from the phantom variations with (e) EF = 25%, (f) EF = 50%, and (g) EF = 75%.

are similar, suggesting that the acceptable range of model orders is relatively stable as a function of EF.

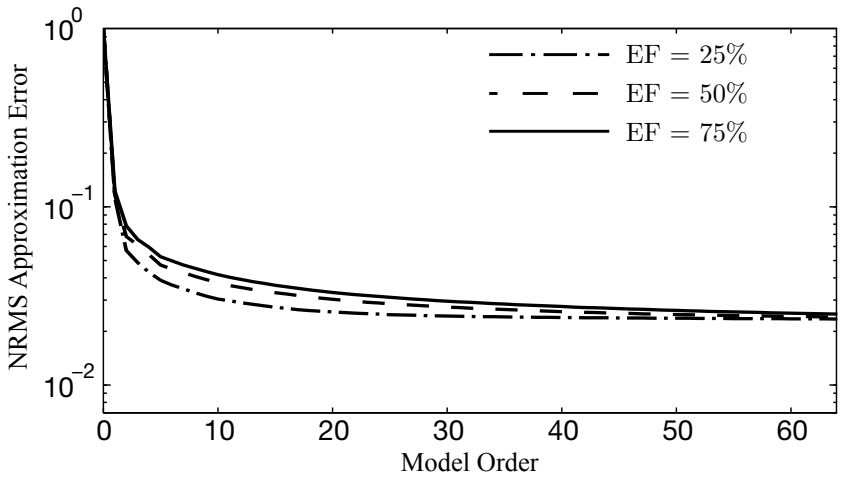

Figure 3.5: Error curves for Eckart–Young approximations of phantoms with different EFs. Phantoms with lower EF can be represented with slightly more accuracy at any given model order, although overall the error curves are fairly similar.

Chapter 4

Data Acquisition

4.1 Sampling requirements

The proposed data acquisition scheme is characterized by the collection of two data sets denoted as $\mathcal{D}_{\text{nav}}$ and $\mathcal{D}_{\text{img}}$ here. For simplicity, we ignore the readout direction of $\mathbf{k}$-space. $\mathcal{D}_{\text{nav}}$ contains data from a few $\mathbf{k}$-space locations at a high temporal rate, and $\mathcal{D}_{\text{img}}$ contains data from sparse $(\mathbf{k}, t)$-space locations. This scheme is motivated by the signal model in Eq. (3.2): $\mathcal{D}_{\text{nav}}$ can just be navigator data (or training data) used to determine the temporal basis functions $\{\hat{\varphi}_\ell(t)\}_{\ell=1}^{L}$, and $\mathcal{D}_{\text{img}}$ should contain imaging data with proper contrast-weighting for determining $\{\hat{\psi}_\ell(\mathbf{r})\}_{\ell=1}^{L}$. Using navigator (or training) data for model estimation in MR dynamic imaging was introduced in [26], and the idea was later used in several other publications (e.g., [27, 38–40]).

Let $\mathcal{D}_{\text{nav}} = \{d_q(\mathbf{k}_{j,1}, t_{j,1})\}_{j=1,q=1}^{J_1,Q}$. Here $\{\mathbf{k}_{j,1}\}_{j=1}^{J_1}$ covers a few $\mathbf{k}$-space locations to ensure that the temporal Nyquist condition is satisfied, without being subject to the $\mathbf{k}$-spaceNyquist constraint or any spatial resolution considerations. In practice, $\{\mathbf{k}_{j,1}\}_{j=1}^{J_1}$ often sample the central $\mathbf{k}$-space based on signal-to-noise considerations. For each $\mathbf{k}_{j,1}$, we assume that

$d_q(\mathbf{k}_{j,1}, t)$ is measured for $t = t_1, t_2, \ldots, t_N$, and that this sampling rate satisfies the temporal Nyquist condition for the underlying signal. The data in $\mathcal{D}_{\text{nav}}$ can be rearranged into Q Casorati matrices $\mathbf{C}(d_q)$, for $q = 1, 2, \ldots, Q$. All the $\mathbf{C}(d_q)$'s share the same temporal subspace as $\rho(\mathbf{r}, t)$, as the inclusion of time-invariant coil sensitivity weightings $\{S_q(\mathbf{r})\}_{q=1}^{Q}$ in Eq. (2.26) does not alter partial separability of the $(\mathbf{k}, t)$-space data. We can then compute the SVD of

$$\begin{bmatrix} \mathbf{C}(d_1) \\ \mathbf{C}(d_2) \\ \vdots \\ \mathbf{C}(d_Q) \end{bmatrix} = \sum_{\ell=1}^{L} \sigma_\ell \mathbf{u}_\ell \mathbf{v}_\ell^H \tag{4.1}$$

and define the temporal basis functions as $\hat{\varphi}_\ell(t_n) = \mathbf{V}_{n\ell}^*$. Having this set of predefined temporal basis functions is enormously useful in low-rank modeling [43] because: a) it reduces the number of degrees-of-freedom in the PS model, b) it simplifies the model-fitting inverse problem so that only the spatial coefficients $\{\hat{\psi}_\ell(\mathbf{r})\}_{\ell=1}^{L}$ need to be determined, and perhaps more importantly, c) it improves the quality of the resulting reconstructions.

With $\{\hat{\varphi}_\ell(t)\}_{\ell=1}^{L}$ being defined, we have a lot of flexibility in acquiring the sparse data $\mathcal{D}_{\text{img}} = \{d_q(\mathbf{k}_{j,2}, t_{j,2})\}_{j=1,q=1}^{J_2,Q}$; there are numerous ways to obtain sufficient data for determining the spatial coefficients of the PS model without being subject to the Nyquist constraint along both $\mathbf{k}$ and t. The following practical factors should be considered in deciding the $(\mathbf{k}, t)$-space sampling locations $\{(\mathbf{k}_{j,2}, t_{j,2})\}_{j=1}^{J_2}$ in a specific data acquisition scheme.

With sensitivity-encoding using Q receiver coils, we can undersample $\mathbf{k}$-space by a factor of $P \leq Q$ according to multichannel sampling theory [51]. In practice, we choose $P \ll Q$ to avoid the well-known ill-conditioning problem associated with conventional parallel imaging. In conventional parallel imaging, there is a trade-off between $\mathbf{k}$-space undersampling and temporal undersampling. By integrating parallel imaging with subspace modeling, the proposed image reconstruction method avoids this trade-off: temporal undersampling is

allowed in PS model-based image reconstruction (as discussed in Chapter 5). Therefore, the proposed method allows more flexibility in placing $\{(\mathbf{k}_{j,2}, t_{j,2})\}_{j=1,q=1}^{J_2,Q}$ and enables sparser sampling of $(\mathbf{k}, t)$-space than conventional parallel imaging.

The proposed method can utilize a spatial-spectral sparsity constraint to regularize the PS model to avoid any potential ill-conditioning problem associated with $(\mathbf{k}, t)$-space undersampling [43]. Sparse modeling is most effective with "incoherent" data acquisition [31]. One can gain the desired incoherence by sampling $(\mathbf{k}, t)$-space in a randomized order [30]. Simply put, for a given $\mathbf{k}_{j,2}$, temporal sampling should not be periodic, i.e., $t_{j,2} \neq j\Delta t$. Details of our experimental implementation can be found in Section 6.2, including an illustrative example of a suitable sampling pattern in Fig. 6.1.

4.2 Self-navigation

In applications with very high temporal resolution requirements (e.g., small rodent imaging), we propose to use "self-navigation" for further acceleration [75]. Self-navigated pulse sequences collect readouts of both $\mathcal{D}_{\text{nav}}$ and $\mathcal{D}_{\text{img}}$ within the space of a single T_{R}, eliminating the need to expend an entire T_{R} to collect navigator data. This is particularly suited for T_2^*-weighted imaging (and therefore SPIO-labeled immune cell imaging), as the late $\mathcal{D}_{\text{img}}$ echo time required for T_2^*-weighted imaging leaves extra room for the navigator signal to be collected prior to each sparse (i.e., $\mathcal{D}_{\text{img}}$) imaging echo [76]. In this case, self-navigation shortens the temporal sampling rate of $\mathcal{D}_{\text{nav}}$ from $2T_{\text{R}}$ to T_{R}, thereby doubling the frame rate of the final reconstructed images from $1/2T_{\text{R}}$ to $1/T_{\text{R}}$. In this approach, $J_1 = J_2 = J$ and $t_{j,2} = (t_{j,1} + \Delta T_{\text{E}})\,\forall j$, where ΔT_{E} is the time between navigator and sparse echoes.

One way to accomplish self-navigation is to separate the slice rephase, read dephase, and phase encode gradient pulses and collect navigator data during slice rephasing and read dephasing. The slice rephase and read dephase pulses are the same after every RF

pulse, enabling collection of suitable data for $\mathcal{D}_{\text{nav}}$. In our implementations, we additionally replace the read dephase pulse with a novel "music note" (♪) trajectory [75], which has the same integral as the typical read dephase pulse (i.e., it ends in the same **k**-space location). The 1D trajectory of the typical read dephase pulse has a null space such that it cannot detect perpendicular translation (as discussed in Section 4.3), so it is preferable to use a 2D navigator such as the music note trajectory or a spiral trajectory. We have designed and implemented the music note to: a) traverse a high-SNR region of **k**-space; and b) be less demanding of gradient hardware than spiral trajectories. We use the same music note navigator trajectory after each RF pulse, but vary the phase encode pulse to acquire different Cartesian imaging readouts of $\mathcal{D}_{\text{img}}$.

Figure 4.1 shows an example of slice-spoiled FLASH pulse sequences implementing (a) interleaved-pulse navigation and (b) self-navigation. As pictured, our "read dephase" gradient actually traverses the 2D "music note" trajectory illustrated in Fig. 4.1-c. Other gradient combinations and **k**-space trajectories could also be used for self-navigation, but the remainder of this dissertation will consider the implementation represented by Fig. 4.1-b.

When short echo times are desired (e.g., T_1-weighted imaging), or when speed requirements do not approach $1/T_{\text{R}}$ (e.g., human imaging), it may be useful to use a interleaved-pulse navigation scheme instead of self-navigation. In this approach, successive readouts of $\{d_q(\mathbf{k},t)\}_{q=1}^{Q}$ alternate between $\mathcal{D}_{\text{nav}}$ and $\mathcal{D}_{\text{img}}$ such that $J_1 = J_2 = J$ and $t_{j,2} = (t_{j,1} + T_{\text{R}})\,\forall j$, where T_{R} is the time between readouts. Thus, $\mathcal{D}_{\text{nav}}$ contains $(\mathbf{k},t)$-space data from N_{d} unique **k**-space trajectories sampled in repeating order: $\mathbf{k}_{j,2} = \mathbf{k}_{(j-N_{\text{d}}),2}\,\forall\, j > N_{\text{d}}$.

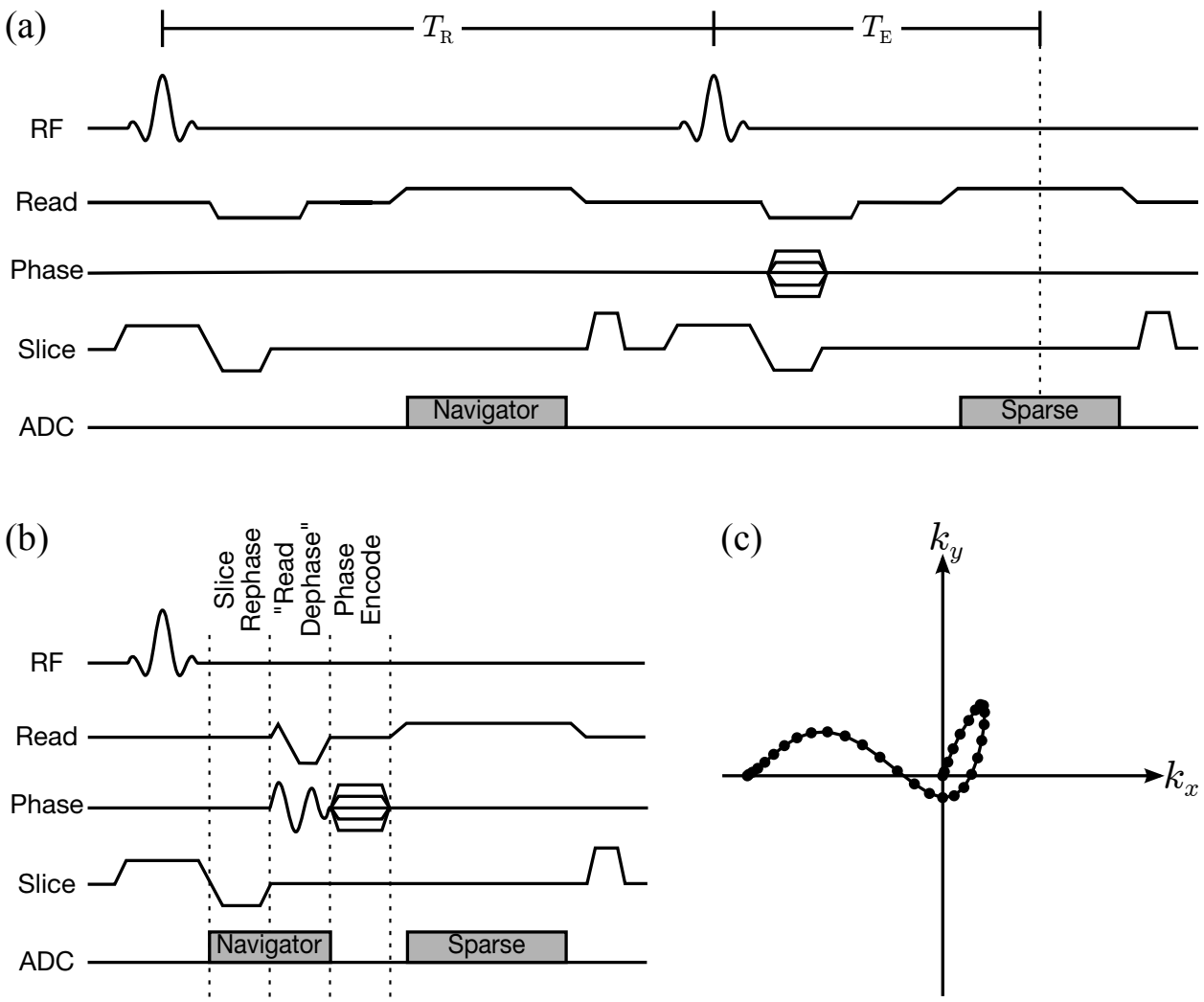

Figure 4.1: Slice-spoiled FLASH sequences illustrating (a) the interleaved-pulse navigation strategy, (b) the proposed self-navigated strategy, and (c) the music note trajectory employed for the results in this dissertation. The self-navigated sequence is half the duration of the interleaved-pulse sequence, doubling the frame rate of the reconstructed images.

4.3 Subspace error

Accurate estimation of the subspace S_Φ (and thus $\mathbf{\Phi}$) is essential for accurate image reconstruction in subspace-constrained imaging. Potential sources of error in the estimated subspace $S_{\hat{\Phi}}$ are measurement noise and limited k-space coverage of $\mathcal{D}_{\text{nav}}$. Both sources of error are closely tied to the choice of navigator trajectories (i.e., navigator $\mathbf{k}$-space locations). Although measurement noise is unavoidable, navigator trajectories can be chosen to traverse regions of $\mathbf{k}$-space which generally have high SNR (e.g., central $\mathbf{k}$-space). The second source of error occurs when S_Φ nontrivially intersects a null space associated with the chosen navigator trajectory, preventing accurate subspace estimation even under noiseless conditions: $\mathbf{C}(\mathcal{D}_{\text{nav}}) \in S_{\hat{\Phi}} \subset S_\Phi$, with $\dim(S_{\hat{\Phi}}) < L$.

A simple example of this null space problem arises for any navigator trajectory which is a line through the $\mathbf{k}$-space origin: here, the navigator data are Fourier-transformed projections of $\rho(\mathbf{r}, t)$, so any translation of $\rho(\mathbf{r}, t)$ perpendicular to the navigator direction will have no effect on $\mathcal{D}_{\text{nav}}$ and will therefore go undetected. Figure 4.2 shows the results of projecting a numerical phantom onto subspaces estimated from horizontal ($k_y = 0$, pictured in Fig. 4.3-a) and vertical ($k_x = 0$) Cartesian navigators. This phantom depicts a large gray circle which translates vertically and a small white circle which translates horizontally; additionally, the two circles live in orthogonal temporal subspaces. The horizontal navigator fails to capture vertical translation, and the vertical navigator fails to capture horizontal translation.

We address the null space problem by replacing the conventional Cartesian trajectories with 2D spiral trajectories, the 2D music note trajectory, or 3D cone trajectories. Unlike the Cartesian trajectories, each of these trajectories has no problem detecting translation perpendicular to the readout direction; this makes subspace estimation robust to navigator orientation. The music note trajectory is a practical and efficient stand-in for a spiral trajectory, traversing a high-SNR region of $\mathbf{k}$-space with low gradient slew rates (particularly

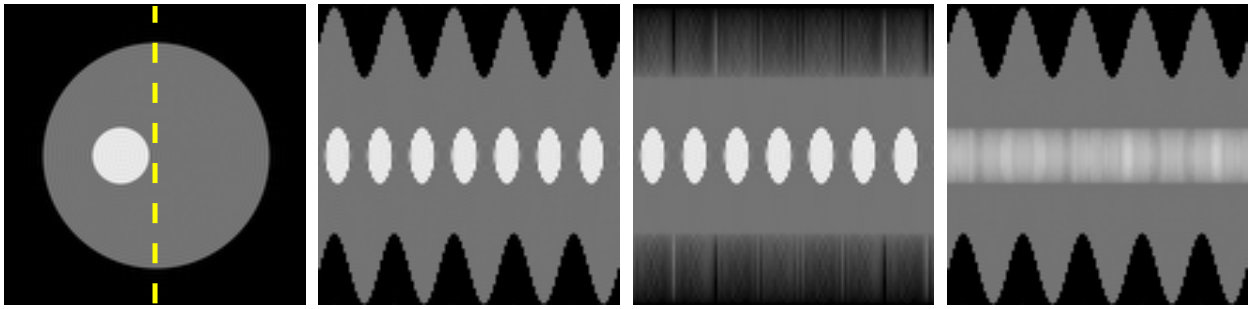

Figure 4.2: Demonstration of the null space problem using central Cartesian navigators. (a) One frame of a numerical phantom and (b) a spatiotemporal slice through the dotted line. Spatiotemporal slices after projecting the phantom onto the subspace $S_{\hat{\Phi}}$ estimated from (c) horizontal and (d) vertical Cartesian navigators through the **k**-space origin. The vertical translation of the gray circle is not captured by the horizontal navigator, and the horizontal translational of the white circle is not captured by the vertical navigator.

useful for self-navigation).

4.4 Simulation analysis

We used the numerical cardiac phantom described in Section 3.2.2 to synthesize and compare different navigator trajectories and the accuracy of the resulting temporal subspaces. We measured six sets of noisy navigator data using the three trajectories in Fig. 4.3, as well as those same trajectories rotated clockwise by 90°. The SVD of the ith noisy navigator data set yielded each $\hat{\mathbf{\Phi}}_i$, which were used to define the temporal subspaces.

White complex Gaussian noise with a blood-to-myocardium contrast-to-noise ratio of 10 was added to all simulated data to better represent realistic experimental conditions. For simulated sparse sampling, $\mathcal{U}\{\cdot\}$ retained only one random **k**-space line per time frame.

Figure 4.4 depicts an 81 × 81 closeup of the heart from the gold standard $\rho(\mathbf{r}, t)$, from the direct Fourier reconstruction of fully sampled noisy data, and from $\{\hat{\mathbf{C}}_{\text{rec},i}(\rho)\}_{i=1}^{6}$, reconstructed from sparsely sampled noisy data using $L_1 = 14$ and $L_2 = 32$. Error images (scaled by a factor of 3) are also shown for all reconstructions. Table 4.1 shows the corresponding

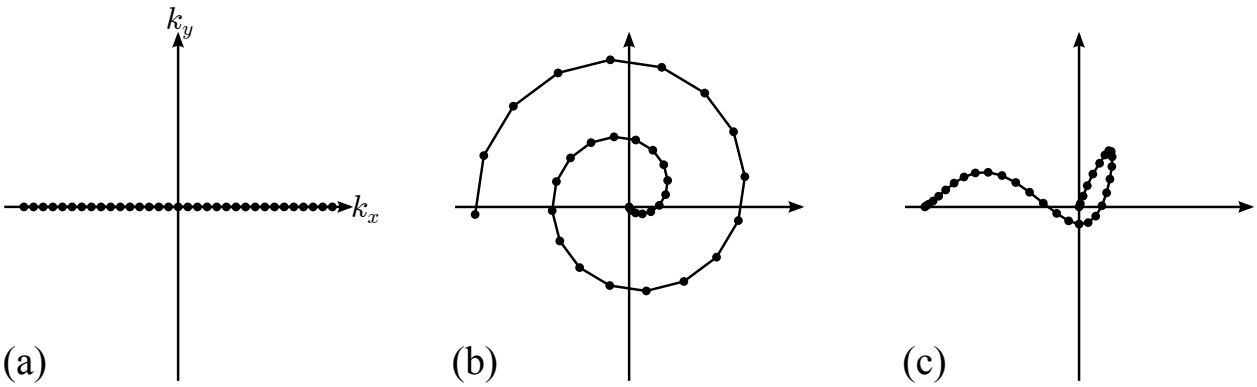

Figure 4.3: Illustrations of the **k**-space trajectories used for simulations: (a) Cartesian, (b) spiral, (c) music note.

Table 4.1: NRMS errors $\{E_{\text{rec}}(\hat{\mathbf{\Phi}}_i)\}_{i=1}^6$

	Cartesian	Spiral	Music note
Standard	5.63%	5.70%	5.61%
Rotated	5.90%	5.67%	5.66%

NRMS errors $\{E_{\text{rec}}(\hat{\mathbf{\Phi}}_i)\}_{i=1}^6$. Figure 4.5 shows the NRMS errors for $\{E_{\text{proj}}(\hat{\mathbf{\Phi}}_i)\}_{i=1}^6$ over a variety of ranks.

Figures 4.4 and 4.5 demonstrate that the subspace accuracy when using Cartesian navigation is highly dependent on trajectory orientation: rotating the trajectory 90° caused a noticeable degradation in image quality. The spiral and music note trajectories were more robust to orientation. For both projections and reconstructions, the rotated Cartesian navigator yielded the least accurate results, whereas the music note navigator provided the most accurate results.

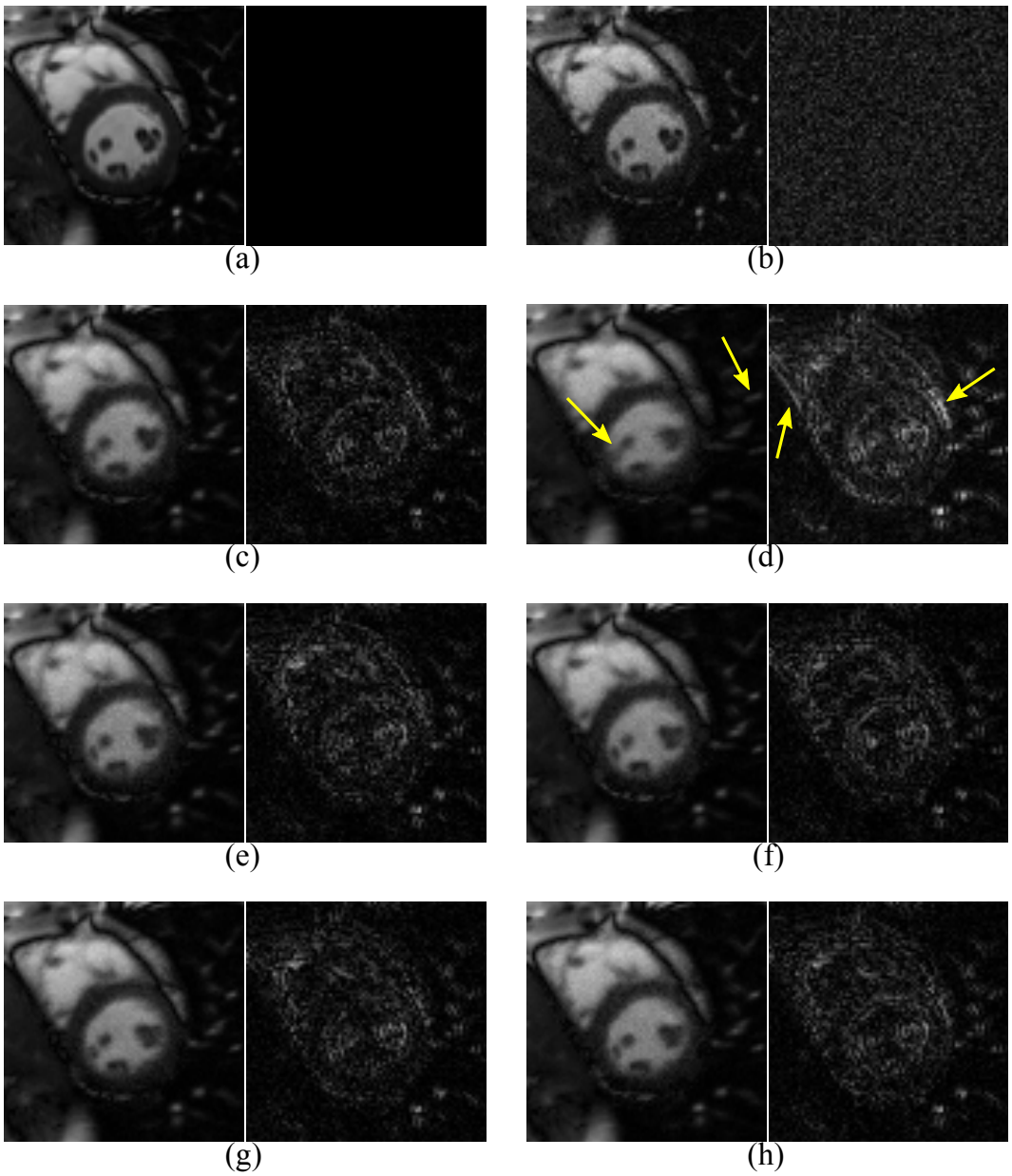

Figure 4.4: A closeup (*left*) and error image (*right*, scaled by a factor of 3) from one frame of (a) the gold standard image $\rho(\mathbf{r}, t)$, (b) the direct Fourier reconstruction from fully sampled noisy data, and (c-h) $\{\hat{\mathbf{C}}_{\mathrm{rec},i}(\rho)\}_{i=1}^{6}$ ($L_1 = 14$, $L_2 = 32$) reconstructed from sparsely sampled noisy data. The navigator data were collected using the (c) Cartesian, (d) rotated Cartesian, (e) spiral, (f) rotated spiral, (g) music note, and (h) rotated music note trajectories. Rotation of the Cartesian navigator causes spatiotemporal blurring, with examples indicated by the arrows. Regardless of rotation, the spiral and music note navigators yield similar visual quality to the unrotated Cartesian navigator.

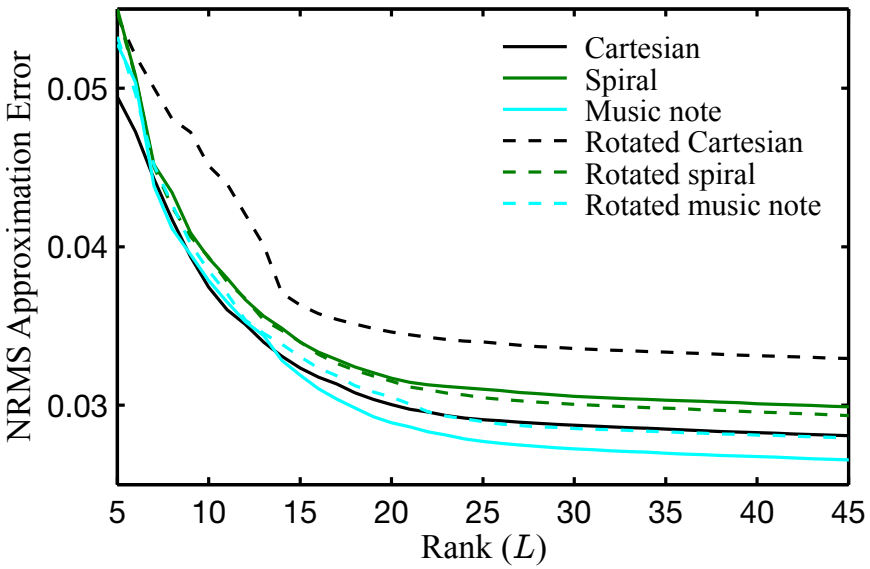

Figure 4.5: NRMS errors $\{E_{\text{proj}}(\hat{\mathbf{\Phi}}_i)\}_{i=1}^{6}$ over a range of model orders. Rotating the Cartesian navigator causes noticeably larger error. The spiral and music note navigators are robust to rotation, with both music note navigators providing slightly more accuracy than either of the spiral navigators.

Chapter 5

Image Reconstruction

5.1 Model fitting equation

Equation (2.36) admits the factorization $\mathbf{C}(\rho) = \mathbf{\Psi}\mathbf{\Phi}$, where $\mathbf{\Psi}_{ij} = \psi_j(\mathbf{r}_i)$ and $\mathbf{\Phi}_{ij} = \varphi_i(t_j)$. Given a predetermined $\hat{\mathbf{\Phi}}$ estimated from $\mathcal{D}_{\text{nav}}$, we can reconstruct $\hat{\mathbf{C}}(\rho)$ by solving for $\hat{\mathbf{\Psi}}$.

We do this by solving the following optimization problem:

$$\hat{\mathbf{\Psi}} = \arg\min_{\mathbf{\Psi}} \sum_{q=1}^{Q} \left\| \mathbf{d}_q - \mathcal{U}\{\boldsymbol{\mathcal{F}}_{\mathbf{r}} \mathbf{S}_q \mathbf{\Psi} \hat{\mathbf{\Phi}}\} \right\|_2^2 + \lambda_1 \|R\{\mathbf{\Psi}\}\|_{1,2} + \lambda_2 P(\mathbf{\Psi}), \tag{5.1}$$

where

$$\|R\{\mathbf{\Psi}\}\|_{1,2} = \sum_{\ell=L_1+1}^{L_2} \left(\sqrt{\sum_{m|\mathbf{r}_m \in \Omega} |\psi_\ell(\mathbf{r}_m)|^2} + \sum_{m|\mathbf{r}_m \notin \Omega} |\psi_\ell(\mathbf{r}_m)| \right). \tag{5.2}$$

The final reconstructed image $\hat{\rho}(\mathbf{r}, t)$ is obtained by $\hat{\mathbf{C}} = \hat{\mathbf{\Psi}}\hat{\mathbf{\Phi}}$.

The first term of the cost function in Eq. (5.1), $\sum_{q=1}^{Q} \|\mathbf{d}_q - \mathcal{U}\{\boldsymbol{\mathcal{F}}_{\mathbf{r}} \mathbf{S}_q \mathbf{\Psi} \hat{\mathbf{\Phi}}\}\|_2^2$, integrates explicit-subspace low-rank imaging with parallel imaging. The second term, $\|R\{\mathbf{\Psi}\}\|_{1,2}$—where $R\{\mathbf{\Psi}\}$ concatenates the rightmost columns of $\mathbf{\Psi}$ (i.e., $\boldsymbol{\psi}_{L_1+1}$ through $\boldsymbol{\psi}_{L_2}$) and vec$(\cdot)$ concatenates the columns of the argument matrix—enforces the modeled subspace structure

in Eq. (3.2) by promoting group sparsity of $\{\psi_\ell(\mathbf{r})\}_{\ell=L_1+1}^{L_2}$. This group-sparse constraint is described and evaluated in greater detail later, in Section 5.3. The third term, $P(\mathbf{\Psi})$, is an optional regularization function enforcing additional image properties to address any remaining ill-conditioning of the data fitting problem. When $P(\cdot)$ is chosen as a sparsity-promoting penalty, Eq. (5.1) additionally integrates sparse modeling; when we additionally consider the case with $\lambda_1 = 0$ or $L_1 = L_2$, Eq. (5.1) can be viewed as integrating the PS-Sparse model [42, 43] with multicoil reconstruction.

5.2 Choice of $P(\cdot)$

Here we investigate two choices for $P(\cdot)$. One choice employs an ℓ_1 penalty to enforce spatial-spectral sparsity; another employs an ℓ_2 penalty to impose anatomical constraints. In comparing these two example choices of $P(\cdot)$, we will consider reconstruction error, noise properties, and image artifacts.

5.2.1 Enforcing spatial-spectral sparsity

It is well established that cardiovascular images have compact spatial-spectral support [28, 29, 79], and can therefore be sparsified by a temporal Fourier transform [31, 33, 35, 44, 80] (among other transforms [30, 32, 34]). Figure 5.1 shows the utility of $T = \mathcal{F}_t$ (i.e., the temporal Fourier transform) as a sparsifying transform for a spatiotemporal slice from a cardiac image.

As described in Section 2.2.3, ℓ_1-norm penalties can be used to promote sparse solutions, so the regularization functional $P(\mathbf{\Psi}) = \|\text{vec}(\mathbf{\Psi}\hat{\mathbf{\Phi}}\boldsymbol{\mathcal{F}}_t)\|_1$ (where $\boldsymbol{\mathcal{F}}_t$ applies the temporal Fourier transform) can be used to promote spatial-spectral sparsity alongside explicit-subspace imaging [42,43]. When evaluating this regularization functional, we will employ randomly ordered $(\mathbf{k}, t)$-space sampling, as it generally results in a sampling basis $\boldsymbol{\mathcal{U}}\boldsymbol{\mathcal{F}}_{\mathbf{r}}$ which is incoherent

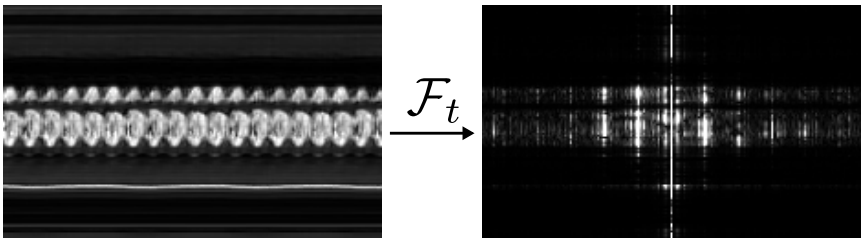

Figure 5.1: An illustration of spatial-spectral sparsity. *Left*, a spatial-temporal slice of a typical cardiac image function, and *right*, its corresponding spatial-spectral representation. The image in the spatial-spectral domain is highly sparse (or highly compressible).

with the temporal Fourier transform [42, 43].

5.2.2 Enforcing anatomical constraints

When morphological information is already available from a reference image $\rho_{\text{ref}}(\mathbf{r})$ depicting the same anatomy, it is possible to define $P(\cdot)$ to impose anatomical constraints on the smoothness of the reconstruction [81]. This controlled smoothing penalizes the formation of motion artifacts and increases SNR without blurring the edges of the object. In the case of cardiovascular imaging, $\rho_{\text{ref}}(\mathbf{r})$ can be gleaned from the temporal average of the $(\mathbf{k}, t)$-space data, removing the need for auxiliary scans or prior information [77].

Specifically, we can define

$$\begin{aligned} P(\mathbf{\Psi}) &= \sum_m \sum_n \sum_i \left| w_i(\mathbf{r}_m) \nabla_i \left\{ \hat{\rho}(\mathbf{r}_m, t_n) \right\} \right|^2 \\ &= \sum_m \sum_n \sum_i \left| w_i(\mathbf{r}_m) \nabla_i \left\{ \sum_\ell \psi_\ell(\mathbf{r}_m) \hat{\varphi}_\ell(t_n) \right\} \right|^2 , \end{aligned} \tag{5.3}$$

where $\{\mathbf{r}_m\}_m$ and $\{t_n\}_n$ are the spatial and temporal coordinates of the voxel centers, $\nabla_i\{\cdot\}$ is a gradient operator (e.g., the finite difference operator) in the ith spatial direction, $w_i(\mathbf{r})$

is the penalty weighting function

$$w_i(\mathbf{r}) = \min\left(\frac{1}{|\nabla_i\{\rho_{\text{ref}}(\mathbf{r})\}|}, w_{\max}\right), \tag{5.4}$$

and $w_{\max}$ is the maximum allowed penalty value. Note that when the $\{\varphi_\ell(t)\}_\ell$ are orthonormal (as when defined from directly from the SVD), Eq. (5.3) reduces to

$$P(\mathbf{\Psi}) = \sum_m \sum_\ell \sum_i |w_i(\mathbf{r}_m)\nabla_i\{\psi_\ell(\mathbf{r}_m)\}|^2, \tag{5.5}$$

which applies the smoothness penalty directly to the spatial coefficient functions $\{\psi_\ell(\mathbf{r})\}_\ell$.

Equation (5.3) discourages the formation of sharp image features in $\rho(\mathbf{r}, t)$ which are not represented in $\rho_{\text{ref}}(\mathbf{r})$. This helps suppress both noise and motion artifacts in the reconstruction while protecting image edges from being smoothed. The overall effect is that it penalizes the formation of image features in $\rho(\mathbf{r}, t)$ inversely proportional to their prominence in $\rho_{\text{ref}}(\mathbf{r})$, excluding when $w_i(\mathbf{r}) = w_{\max}$. The use of $w_{\max}$ softens the penalties corresponding to very smooth areas of $\rho_{\text{ref}}(\mathbf{r})$ and prevents these areas from overinfluencing the final solution. When Eq. (5.1) is viewed in a quasi-Bayesian context, the definition of the weighting functions as in Eq. (5.4) may be interpreted as incorporating $\rho_{\text{ref}}(\mathbf{r})$ into the model as a statistical prior [81].

Practically speaking, $\rho_{\text{ref}}(\mathbf{r})$ is not always available in the form of *a priori* information. However, it is both simple and effective to generate $\rho_{\text{ref}}(\mathbf{r})$ from a composite of the measured data $\{d_q(\mathbf{k}_j, t_j)\}_{j=1,Q=1}^{J,Q}$. Ideally, $\rho_{\text{ref}}(\mathbf{r})$ should be free from aliasing artifacts and should exhibit high SNR. There are many methods for reconstructing such images from composite $(\mathbf{k}, t)$-space data, even when the measured data violates the Nyquist condition [82]. The results in this section use $\rho_{\text{ref}}(\mathbf{r})$ reconstructed from $\{\bar{d}_q(\mathbf{k}_m)\}_{q=1}^{Q}$, a weighted sum of the

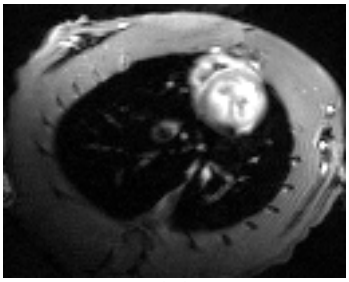

(a)

(b)

(c)

Figure 5.2: (a) Example reference image $\rho_{\text{ref}}(\mathbf{r})$ (*top*) and (b-c) the resulting penalty weighting functions $\{w_i(\mathbf{r})\}_i$. Note that weighting is defined separately for the (b) vertical and (c) horizontal gradients.

measured data over the time axis:

$$\bar{d}(\mathbf{k}_m) = \frac{\sum_n d(\mathbf{k}_m, t_n)}{\sum_n \mathcal{U}(\mathbf{k}_m, t_n)}, \tag{5.6}$$

where $\mathcal{U}(\mathbf{k}_m, t_n)$ is set to 1 for the $(\mathbf{k}, t)$-space locations which were actually sampled (i.e., for which $(\mathbf{k}_m, t_n) \in \{(\mathbf{k}_j, t_j)\}_{j=1}^{J}$); otherwise, $\mathcal{U}(\mathbf{k}_m, t_n)$ takes the value of 0. The expression $\sum_n \mathcal{U}(\mathbf{k}_m, t_n)$ gives the total number of samples which are collected at $\mathbf{k}_m$, and Eq. (5.6) is therefore equivalent to averaging the measured data independently at each $\mathbf{k}_m$. We can then obtain $\rho_{\text{ref}}(\mathbf{r})$ by reconstructing $\{\bar{d}_q(\mathbf{k}_m)\}_{q=1}^{Q}$ by Fourier reconstruction or by parallel imaging reconstruction methods when appropriate. Figure 5.2 shows an example reference image $\rho_{\text{ref}}(\mathbf{r})$ and penalty weightings $\{w_i(\mathbf{r})\}$ used in the proposed reconstruction scheme.

5.2.3 Simulation analysis

5.2.3.1 Separation of artifacts and noise

Nonlinear reconstruction methods do not allow for direct separation of image artifacts and image noise in the resulting reconstructions. Here, we perform Monte Carlo simulation to perform this separation instead. Given multiple reconstructions with different noise patterns, the nth reconstructed image vector $\hat{\boldsymbol{\rho}}^{(n)}$ can be represented as a sum of the true image vector $\boldsymbol{\rho}$, an image artifact vector $\mathbf{a} = E[\hat{\boldsymbol{\rho}} - \boldsymbol{\rho}]$ (where E denotes expectation), and an image noise vector $\boldsymbol{\eta}^{(n)}$ (i.e., $\hat{\boldsymbol{\rho}}^{(n)} = \boldsymbol{\rho} + \mathbf{a} + \boldsymbol{\eta}^{(n)}$). We consider $\mathbf{a}$ to be the deterministic error component which represents the systematic reconstruction error (i.e., the spatiotemporally localized error bias) for a specific input noise distribution and $\boldsymbol{\eta}$ to be the error component whose elements are realizations of zero-mean random variables. We perform this analysis for each input noise distribution in our simulations.

For a set input noise distribution, Monte Carlo simulation of N different reconstructions $\{\hat{\boldsymbol{\rho}}^{(n)}\}_{n=1}^{N}$ yields an average reconstruction

$$\hat{\boldsymbol{\rho}}_{\text{avg}} = \frac{1}{N}\sum_{n=1}^{N}\hat{\boldsymbol{\rho}}^{(n)} = \boldsymbol{\rho} + \mathbf{a} + \frac{1}{N}\sum_{n=1}^{N}\boldsymbol{\eta}^{(n)}, \tag{5.7}$$

where $\boldsymbol{\eta}^{(n)}$ is the image noise pattern corresponding to $\hat{\boldsymbol{\rho}}^{(n)}$. Equation (5.7) suggests the approximations

$$\|\mathbf{a}\|_2^2 \approx \|\hat{\boldsymbol{\rho}}_{\text{avg}} - \boldsymbol{\rho}\|_2^2 - \frac{1}{N}\|\boldsymbol{\eta}\|_2^2 \tag{5.8}$$

and

$$\|\boldsymbol{\eta}\|_2^2 \approx \frac{1}{N-1}\sum_{n=1}^{N}\|\hat{\boldsymbol{\rho}}^{(n)} - \hat{\boldsymbol{\rho}}_{\text{avg}}\|_2^2. \tag{5.9}$$

For large N, a useful estimate of $\mathbf{a}$ is the mean reconstruction error function

$$\mathbf{a} \approx \hat{\boldsymbol{\rho}}_{\text{avg}} - \boldsymbol{\rho}, \tag{5.10}$$

which further yields

$$\boldsymbol{\eta}^{(n)} \approx \hat{\boldsymbol{\rho}}^{(n)} - \hat{\boldsymbol{\rho}}_{\text{avg}}. \tag{5.11}$$

The range of N for which Eqs. (5.10) and (5.11) are useful may be inferred from spatiotemporally varying confidence intervals; however, Eqs. (5.8) and (5.9) suggest the simple guideline $N \gg \max\left(\|\boldsymbol{\eta}\|_2^2/\|\mathbf{a}\|_2^2,\, 1\right)$.

5.2.3.2 Monte Carlo Results

To demonstrate both the ℓ_1 and ℓ_2 regularization methods using a realistic gold standard, we include simulation results using the numerical cardiac phantom described in Section 3.2.2.

Simulations were conducted by sparsely sampling $(\mathbf{k}, t)$-space data from the numerical phantom. Only one $(\mathbf{k}, t)$-space readout line was collected every 3 ms (the effective T_{R}). Data acquisition was alternated between $\mathcal{D}_{\text{nav}}$ and $\mathcal{D}_{\text{img}}$ over the full duration of the image sequence. In the ℓ_1 case, the order of phase encodings for $\mathcal{D}_{\text{img}}$ was permuted to simulate a uniform random sampling pattern. In the ℓ_2 case, $\mathcal{D}_{\text{img}}$ was collected using sequential phase encoding (from one end of $\mathbf{k}$-space to the other). In both cases, $\mathcal{D}_{\text{nav}}$ was acquired by repeatedly measuring data from seven lines at the center of $\mathbf{k}$-space.

Three noise levels were considered for each regularization scheme, specifically the noiseless case and two noisy cases. For the noisy cases, complex Gaussian noise $\boldsymbol{\xi}$ was added to the $(\mathbf{k}, t)$-space samples. The artifact and noise components of the resulting noisy reconstructions were separated through Monte Carlo simulation, using a sample size of 10 for each regularization scheme at each noise level. Regularization parameters were set according to the noise level in the data. All reconstructions were performed with model order

Table 5.1: NRMS values for total reconstruction error, image artifacts, and image noise

		Total Error	Artifacts	Noise
Noiseless	ℓ_1	3.34%	3.34%	n/a
	ℓ_2	3.91%	3.91%	n/a
Low Noise	ℓ_1	3.58%	3.38%	1.17%
	ℓ_2	4.36%	3.96%	1.82%
High Noise	ℓ_1	4.98%	3.68%	3.35%
	ℓ_2	6.09%	5.04%	3.42%

$L_1 = L_2 = 16$.

Figure 5.3 shows reconstructed frames over the 63×63 cardiac region. The top row shows the gold standard plus the appropriate level of noise. The top right image is from the noiseless gold standard ρ against which all reconstructions were compared. The second row shows least-squares PS reconstructions (i.e., PS without regularization). The bottom two rows show PS reconstructions with ℓ_1 and ℓ_2 regularization. Figure 5.4 shows spatial maps of the separated artifact (bias) and noise terms at the high input noise level. Each spatial map depicts RMS values across time. Table 5.1 gives NRMS values for the reconstruction error, image artifacts, and image noise. The ℓ_1 scheme resulted in overall lower reconstruction error energy, image artifact energy, and image noise variance in all cases.

Because the ℓ_2 regularization scheme imposes a spatially weighted smoothness penalty, the resulting image noise is predictably focused in the areas which correspond to low smoothness penalties. The spatial location of the image noise in the ℓ_1-regularized reconstructions exhibits less structure: that is to say, the image noise is more evenly distributed spatially. Reconstructions from the ℓ_2 scheme shows significantly higher error bias over most spatial regions when compared to reconstructions from the ℓ_1 scheme.

The spatial maps of artifacts and error give a general idea as to the utility of each regularization scheme for different biomedical applications. Although there are some spatial regions

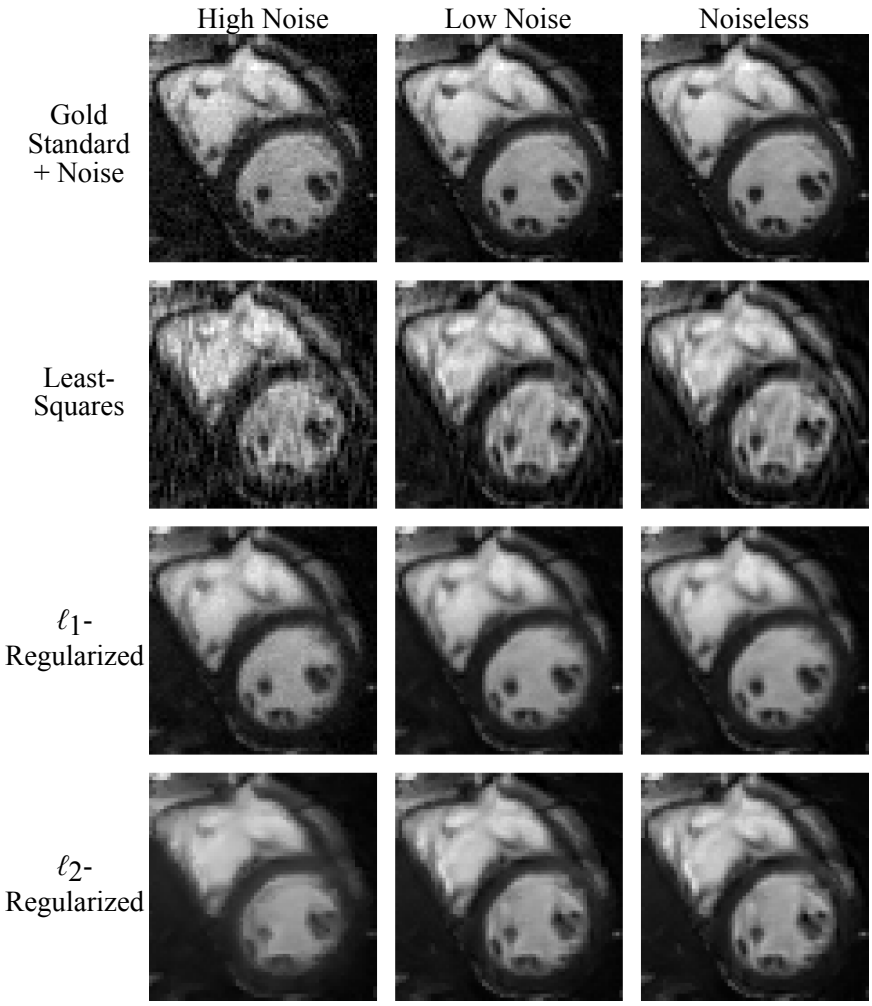

Figure 5.3: Reconstructions over the 63×63 cardiac region. The top row depicts the gold standard plus noise with appropriate variance. The second row depicts least-squares PS reconstructions. The bottom two rows depict the PS reconstructions with ℓ_1 and ℓ_2 regularization.

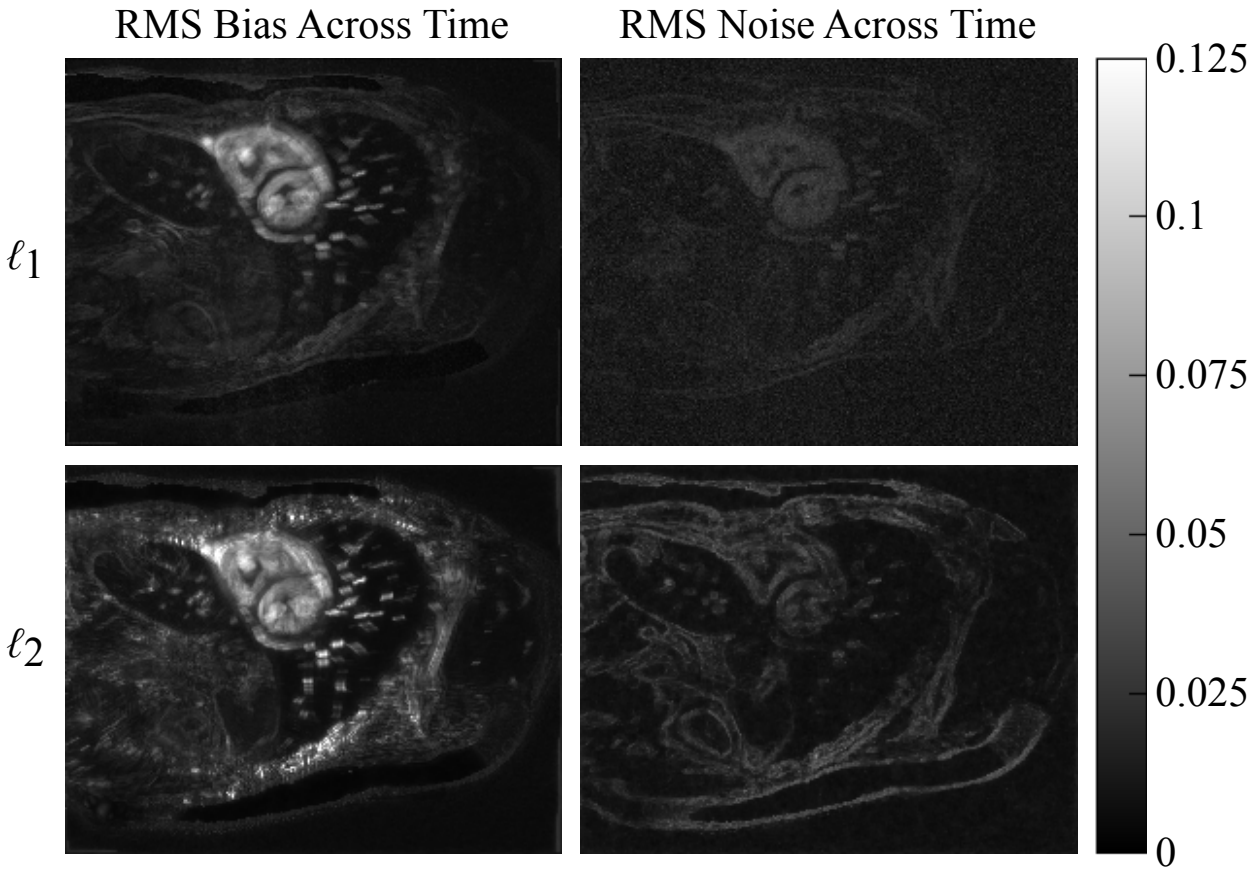

Figure 5.4: Spatial maps of artifacts and noise (i.e., RMS values of the bias and noise across time) for the regularized PS reconstructions corresponding to the high input noise level. For clarity, the contrast window is 8 times brighter here than the contrast window in Fig. 5.3

of the reconstructions over which the ℓ_2 solution exhibits both smaller error bias and lower noise, the cardiac region is generally better represented by the ℓ_1 solution.

Overall, the ℓ_1 solution is consistently the most accurate in terms of reconstruction error, image artifacts, and image noise. The ℓ_2 solution is much quicker to compute, and the closed-form linear solution to the ℓ_2 optimization problem has the benefit of easier characterizability as compared to the nonlinear ℓ_1 optimization problem. When computation time and resources are freely available, the ℓ_1 method will be preferable in most situations. The ℓ_2 method may be preferable when computational efficiency is desired. The remainder of the results in this dissertation employ the ℓ_1 method.

5.3 Group sparsity

The constraint $\|R\{\mathbf{\Psi}\}\|_{1,2}$ in Eq. (5.1) promotes group sparsity of $\{\psi_\ell(\mathbf{r})\}_{\ell=L_1+1}^{L_2}$ in order to enforce the subspace structure in Eq. (3.2). Defining $\mathbf{x}_{(i)}$ as the ith group of some vector $\mathbf{x}$, then the mixed (1,2)-norm is defined as $\|\mathbf{x}\|_{1,2} = \sum_{i=1} \|\mathbf{x}_{(i)}\|_2$ [83, 84]. Equation (5.2) distributes the higher-order spatial coefficients $\{\psi_\ell(\mathbf{r})\}_{\ell=L_1+1}^{L_2}$ into different groups. For each $L_1 < \ell \leq L_2$, each set of cardiac spatial coefficients $\{\psi_\ell(\mathbf{r}_m)\}_{m|\mathbf{r}_m \in \Omega}$ composes a group, as does each individual non-cardiac spatial coefficient $\psi_\ell(\mathbf{r}_m), \mathbf{r}_m \notin \Omega$. As a result, the cardiac region takes on an effective model order up to L_2 and each non-cardiac voxel individually takes on an effective model order of L_1 or slightly higher. This grouping promotes a uniformly high model order over the cardiac region and a spatially varying low model order over the non-cardiac region, introducing flexibility to the choices of L_1 and L_2. This flexibility is desirable for model order selection and region identification in practical applications because: if either L_1 or L_2 is chosen too small, then the representational power of the model is reduced, leading to model bias; if either L_1 or L_2 is chosen too high, then the model becomes sensitive to noise and reconstruction quality will be heavily dependent on regularization. Similarly, this

flexibility also allows imprecise specification of Ω, as voxels incorrectly placed outside Ω would also be allowed to take on a higher model order. Voxels incorrectly placed inside Ω will have higher model orders than necessary, but the model overfitting problem would still be addressed by spatial-spectral sparsity regularization. The group sparsity constraint reduces these potential pitfalls while still allowing the option to exactly enforce the basic PS model by using $L_1 = L_2$.

5.3.1 Simulation analysis

We have evaluated the proposed image reconstruction method using the same numerical cardiac phantom. We provide reconstruction examples using the proposed method as well as sliding window reconstructions (i.e., direct Fourier reconstructions of the sparsely sampled $(\mathbf{k}, t)$-space data after nearest-neighbor temporal interpolation), and CS model reconstructions.

In all simulations, we sparsely sampled $(\mathbf{k}, t)$-space data from the numerical phantom. The sampling pattern was limited to a single $(\mathbf{k}, t)$-space readout line every 3 ms (the effective T_{R}) to represent real-world sampling conditions. Data were collected with $Q = 1$, $P = 1$, and $N_{\mathrm{d}} = 5$.

Reconstructions were performed with a variety of parameters. Regularization parameters were chosen for minimum NRMS reconstruction error E_{rec} after a comprehensive sweep. All reconstructions have a frame rate of 33 fps, which is equal to the temporal sampling rate of the navigator data (i.e., $1/2N_{\mathrm{d}}T_{\mathrm{R}}$).

Table 5.2 presents the NRMS reconstruction errors E_{rec} over a range of values for L_1 and L_2. Entries where $L_1 = L_2$ are denoted by "$*$", and the full-rank (i.e., CS) reconstruction is denoted by "†". The smallest overall reconstruction error appears in bold. Model order combinations where $L_1 > L_2$ are inconsistent with the assumption in Eq. (3.2) that $L_2 \geq L_1$ and are therefore grayed out.

Table 5.2: NRMS reconstruction errors E_{rec} in simulations. "$*$" denotes a result where $L_1 = L_2$, and "†" denotes the full-rank (i.e., CS) result. The model order combinations corresponding to $L_1 > L_2$ are grayed out. The smallest reconstruction error appears in bold.

		L_1 (Non-cardiac)				
		16	25	32	64	1000
L_2 (Cardiac)	16	3.67%*				
	25	3.37%	3.46%*			
	32	3.32%	3.35%	3.42%*		
	64	3.35%	**3.28%**	3.53%	3.81%*	
	1000					9.31%†

The left column of Fig. 5.5 depicts 2D spatiotemporal slices from the phantom (i.e., the gold standard) and the noiseless reconstructions which yielded the smallest NRMS error E_{rec} for each method. The right column depicts the error image for each reconstruction, scaled by a factor of 2 for clarity. We can see that the reconstructions with $L_1 < L_2$ yielded the most accurate reconstruction (in the NRMS error sense) as well as providing the most faithful representation of the true cardiovascular dynamics. For each fixed L_2, the minimum-error reconstruction occurs for some $L_1 < L_2$. Each of the subspace-constrained imaging results achieved significantly less error than the full-rank (i.e., CS) method. The superior performance from using $L_1 < L_2$ over that using $L_1 = L_2$ can be attributed to the variable-rank model which better reflects the nature of cardiovascular images. In contrast, the subspace model with $L_1 = L_2$ and the full-rank model do not distinguish between the different regions of the image, imposing regionally unspecific model assumptions.

Figure 5.6 depicts normalized singular value curves of the cardiac region $\hat{\mathbf{C}}_{\Omega}$ and the non-cardiac region $\hat{\mathbf{C}}_{\not\Omega}$ of the proposed reconstruction with $L_1 = 25$ and $L_2 = 64$. The curves indicate that the constraint $\|R\{\mathbf{\Psi}\}\|_{1,2}$ successfully promoted sparsity of the non-cardiac spatial coefficients indexed above $L_1 = 25$, yielding effective ranks of $L_2 = 64$ for the cardiac

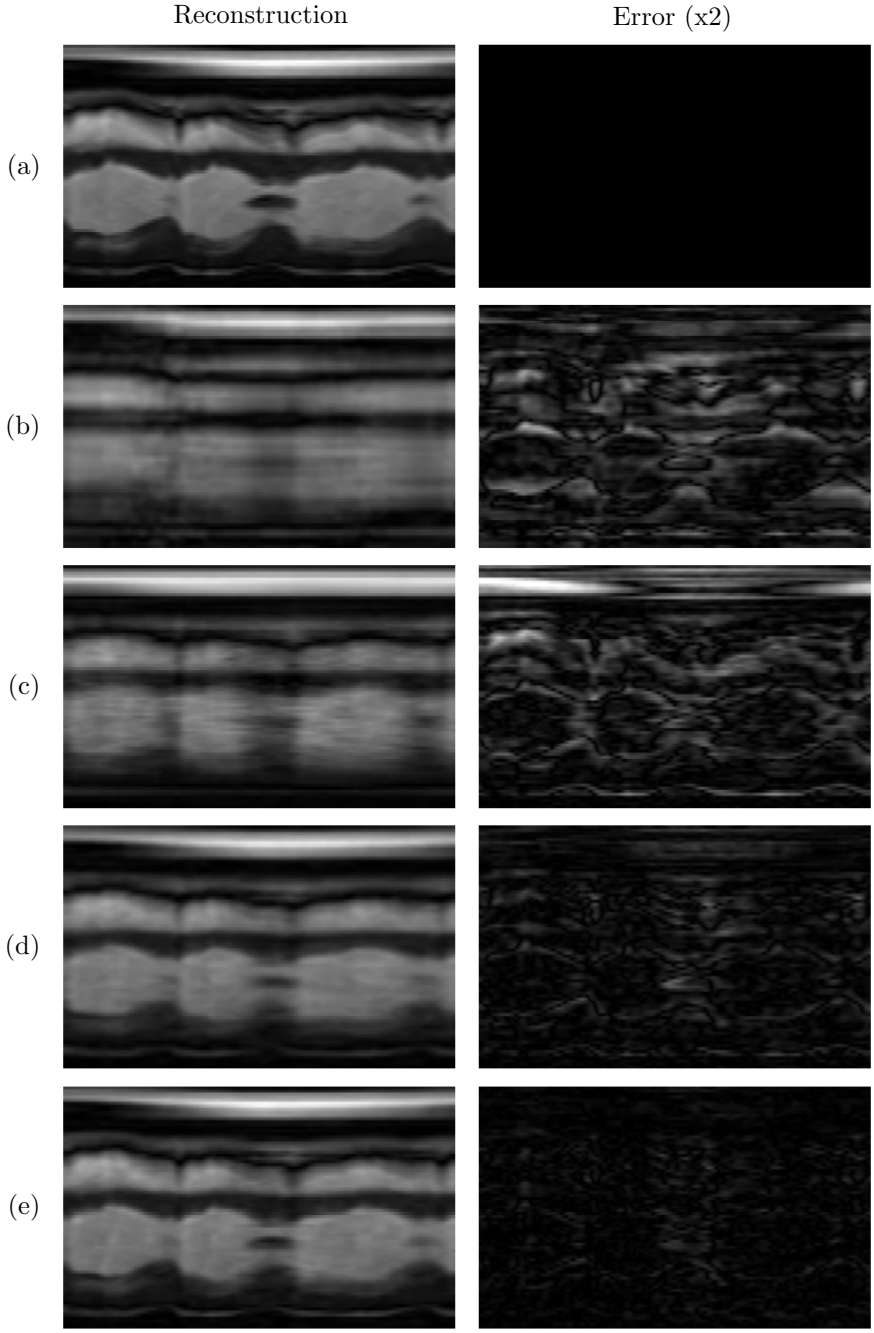

Figure 5.5: The (a) gold standard, (b) sliding window reconstruction, and reconstructions using (c) the full-rank (i.e., CS) model, (d) the proposed model with $L_1 = L_2$, and (e) the proposed model with $L_1 < L_2$. The error images are scaled by a factor of 2.

region and $L_1 = 25$ for the non-cardiac region.

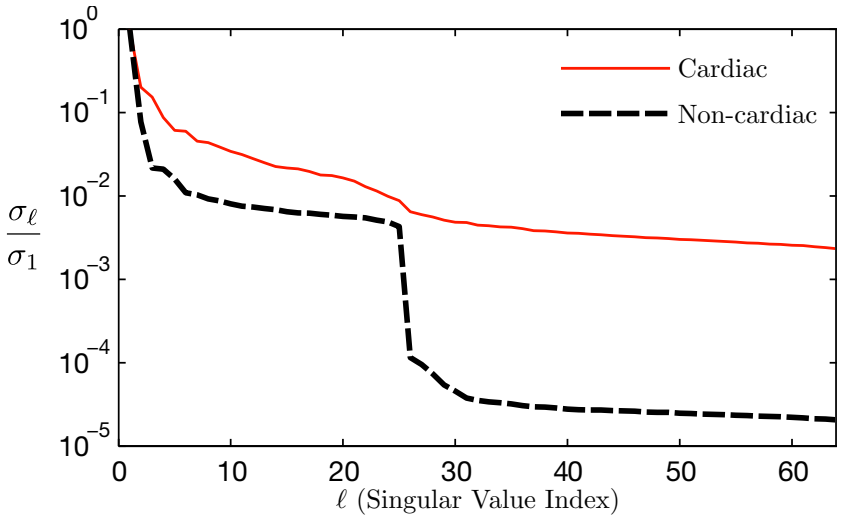

Figure 5.6: Normalized singular value curves from the cardiac and non-cardiac regions of the proposed reconstruction with $L_1 = 25$ and $L_2 = 64$. The proposed method successfully enforced the desired effective ranks.

5.4 Sensitivity map estimation

The sensitivity encoding functions $\{S_q(\mathbf{r})\}_{q=1}^{Q}$ must also be known in order to solve Eq. (5.1). Because these sensitivity encoding functions are assumed to be time-invariant, we propose to extract them from composite $\mathbf{k}$-space data $\{\bar{d}_q(\mathbf{k})\}_{q=1}^{Q}$, e.g., time-averaged $(\mathbf{k}, t)$-space data calculated according to using Eq. (5.6). The sampling schedule $\{\mathbf{k}_j, t_j\}$ plays a large part in determining which strategy should be used to extract $\{S_q(\mathbf{r})\}_{q=1}^{Q}$ from the measured data.

For example, when $\{\mathbf{k}_j\}_{j=1}^{J}$ (the set of $\mathbf{k}$-space locations sampled over the course of the image experiment) satisfies the Nyquist condition, composite images $\{\bar{\rho}_q(\mathbf{r})\}_{q=1}^{Q}$ can be reconstructed from $\{\bar{d}_q(\mathbf{k})\}_{q=1}^{Q}$ via direct Fourier inversion; the sensitivity maps can then be defined as $S_q(\mathbf{r}) = \bar{\rho}_q(\mathbf{r})/\rho_{\text{ref}}(\mathbf{r})$, where $\rho_{\text{ref}}(\mathbf{r})$ is a coil reference image produced from $\{\bar{\rho}_q(\mathbf{r})\}_{q=1}^{Q}$ by the sum-of-squares algorithm $\rho_{\text{ref}}(\mathbf{r}) = \sqrt{\sum_{q=1}^{Q} |\bar{\rho}_q(\mathbf{r})|^2}$ or by some other method (e.g., [85–88]).

When $\{\mathbf{k}_j\}_{j=1}^{J}$ does not satisfy the Nyquist condition but does satisfy the sampling requirements of autocalibrating parallel imaging methods (e.g., GRAPPA [58], SPIRiT [89]), then we have the option of using one of these methods to reconstruct full-resolution composite images $\{\bar{\rho}_q(\mathbf{r})\}_{q=1}^{Q}$ or to instead reconstruct low-resolution composite images from the autocalibration signal. The first strategy extends the method in [90] to instead produce full-resolution sensitivity encoding functions; the second strategy can be seen as a variation of mSENSE [91].

Although coil sensitivities are typically smooth (which would imply that they can be calculated from low-resolution images), it is commonplace for cardiovascular images to be acquired with an FOV larger than the heart but smaller than the chest as a whole. This leads to aliasing of the chest wall (but not the heart) as well as sharp features in the resulting lightly aliased sensitivity functions [92], violating the assumption of smoothness and ensuring that reduced-resolution images alone are inadequate for estimating the resulting coil sensitivities. Figure 5.7 compares the effect of using low-resolution and full-resolution composite images as we have described above to define the sensitivity maps for such a case. The sensitivity weighting function changes sharply from high to low sensitivity in the aliased region; these sharp changes are poorly modeled by the low-resolution sensitivity map and lead to artifacts in the reconstruction. As such, the results in the remainder of this dissertation employ GRAPPA [58] to obtain $\{S_q(\mathbf{r})\}_{q=1}^{Q}$ from the time-averaged measured data (unless otherwise noted), combining the advantages of GRAPPA reconstruction (e.g., robustness to overlapping geometry) with the joint-channel reconstruction of the SENSE [55] inverse problem.

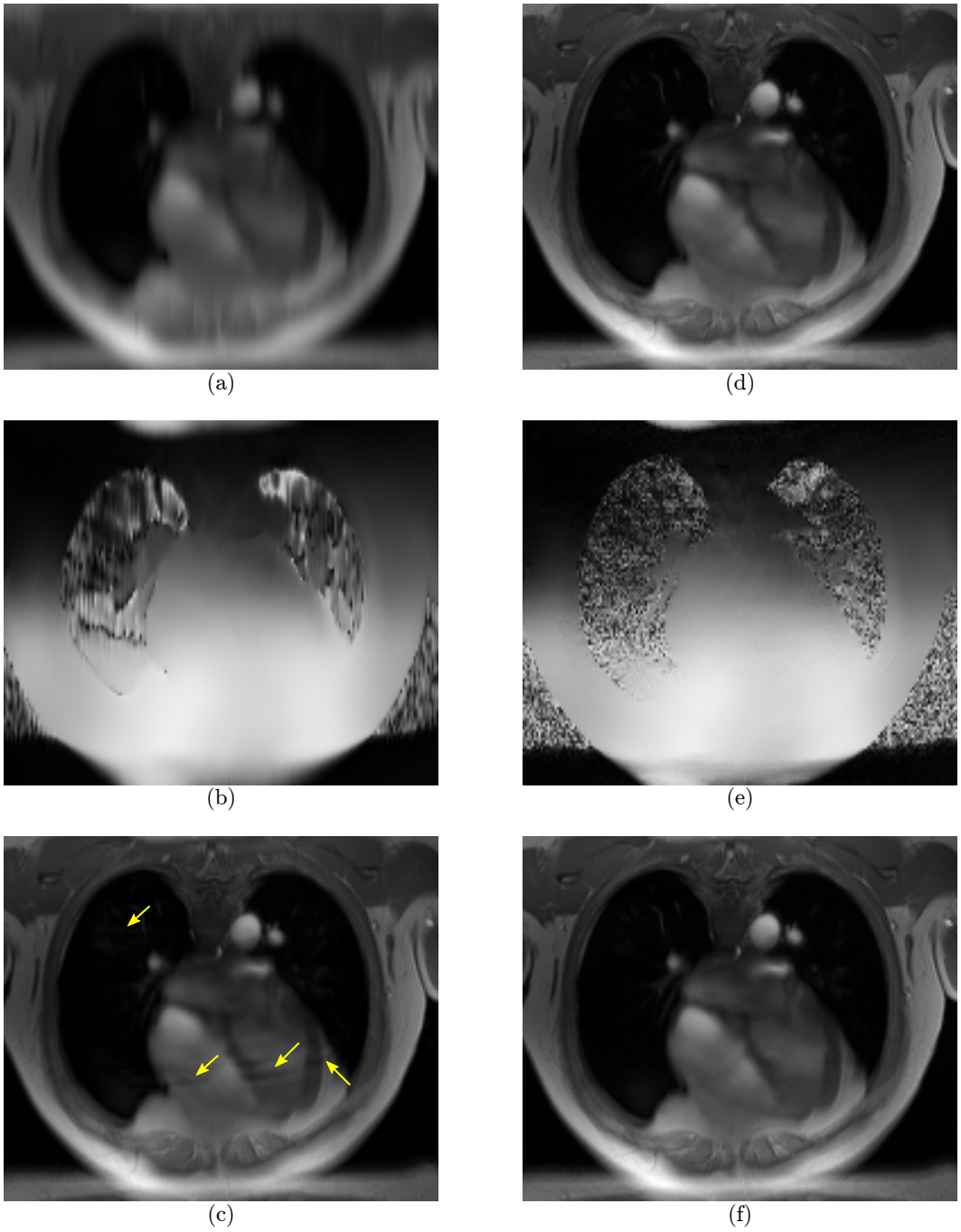

Figure 5.7: $\rho_{\text{ref}}(\mathbf{r})$, $S_4(\mathbf{r})$, and SENSE reconstruction from $\{\bar{d}_q(\mathbf{k})\}_{q=1}^{Q}$ using $\{S_q(\mathbf{r})\}_{q=1}^{Q}$ when (a-c) low-resolution $\{\bar{\rho}_q(\mathbf{r})\}_{q=1}^{Q}$ are calculated using mSENSE; (d-f) full-resolution $\{\bar{\rho}_q(\mathbf{r})\}_{q=1}^{Q}$ are calculated using GRAPPA. The coil sensitivity changes sharply where there is aliasing of the chest wall, so the low-resolution sensitivity maps lead to artifacts in the SENSE reconstruction (as indicated by the arrows).

5.5 Algorithm

The convex optimization problem in Eq. (5.1) can be solved using an additive half-quadratic minimization algorithm [93, 94] extended to handle (1,2)-norm regularization and combined with a continuation procedure [95]. This algorithmic approach has previously been shown to be efficient for similar problems [43], and was used to generate the results in this dissertation.

For simplicity of notation, we define the operator

$$T\{\boldsymbol{\Psi}\} = \frac{1}{\lambda}\begin{bmatrix} \lambda_1 R\{\boldsymbol{\Psi}\} \\ \lambda_2 \mathrm{vec}(\boldsymbol{\Psi}\hat{\boldsymbol{\Phi}}\boldsymbol{\mathcal{F}}_t) \end{bmatrix} \tag{5.12}$$

in order to express the regularization constraints in Eq. (5.1) using an alternative (1,2)-norm expression with groupings such that

$$\lambda\|T\{\boldsymbol{\Psi}\}\|_{1,2,\mathrm{alt}} = \lambda_1\|R\{\boldsymbol{\Psi}\}\|_{1,2} + \lambda_2\|\mathrm{vec}(\boldsymbol{\Psi}\hat{\boldsymbol{\Phi}}\boldsymbol{\mathcal{F}}_t)\|_1. \tag{5.13}$$

Using this simplified notation, Eq. (5.1) becomes

$$\hat{\boldsymbol{\Psi}} = \arg\min_{\boldsymbol{\Psi}} \sum_{q=1}^{Q} \left\| \mathbf{d}_q - \mathcal{U}\{\boldsymbol{\mathcal{F}}_{\mathbf{r}}\mathbf{S}_q\boldsymbol{\Psi}\hat{\boldsymbol{\Phi}}\} \right\|_2^2 + \lambda\|T\{\boldsymbol{\Psi}\}\|_{1,2,\mathrm{alt}}, \tag{5.14}$$

which is a (1,2)-norm regularized inverse problem.

To solve Eq. (5.14), we employ the approximation $\|\mathbf{x}\|_{1,2,\mathrm{alt}} \approx \sum_{i=1} h[\mathbf{x}_{(i)}]$, where $\mathbf{x}_{(i)}$ is the ith group of $\mathbf{x}$ and

$$\begin{aligned} h(\mathbf{y}) &= \begin{cases} \|\mathbf{y}\|_2^2/2\alpha, & \|\mathbf{y}\|_2 \le \alpha \\ \|\mathbf{y}\|_2 - \alpha/2, & \|\mathbf{y}\|_2 > \alpha \end{cases} \\ &= \min_{\mathbf{q}} \frac{1}{2\alpha}\|\mathbf{y}-\mathbf{q}\|_2^2 + \|\mathbf{q}\|_2, \end{aligned} \tag{5.15}$$

with parameter $\alpha > 0$ [94, 95]. This function h is both continuous and differentiable. As $\alpha \to 0$, we have $h[\mathbf{x}_{(i)}] \to \|\mathbf{x}_{(i)}\|_2$, which further yields $\sum_{i=1} h[\mathbf{x}_{(i)}] \to \|\mathbf{x}\|_{1,2,\text{alt}}$. The resulting (1,2,alt)-norm approximation is

$$\|\mathbf{x}\|_{1,2,\text{alt}} \approx \min_{\mathbf{g}} \frac{1}{2\alpha}\|\mathbf{x}-\mathbf{g}\|_2^2 + \|\mathbf{g}\|_{1,2,\text{alt}}. \tag{5.16}$$

The value of $h(\mathbf{y})$ in Eq. (5.15) is reached when $\mathbf{q}$ is the projection of $\mathbf{y}$ onto the 2-norm ball of radius $\max\{0, \|\mathbf{y}\|_2 - \alpha\}$. Similarly, the approximation in Eq. (5.16) is achieved when $\mathbf{g}$ is the projection of $\mathbf{x}$ onto the (1,2,alt)-norm ball of radius $\max\{0, \|\mathbf{x}\|_{1,2,\text{alt}} - \alpha\}$ [96].

Substituting Eq. (5.16) into Eq. (5.14), we now have a different optimization problem:

$$\{\hat{\mathbf{\Psi}}, \hat{\mathbf{g}}\} = \arg\min_{\mathbf{\Psi},\mathbf{g}} \sum_{q=1}^{Q} \left\| \mathbf{d}_q - \mathcal{U}\{\boldsymbol{\mathcal{F}}_\mathbf{r}\mathbf{S}_q\mathbf{\Psi}\hat{\mathbf{\Phi}}\} \right\|_2^2 + \frac{\lambda}{2\alpha}\|T\{\mathbf{\Psi}\} - \mathbf{g}\|_2^2 + \lambda\|\mathbf{g}\|_{1,2,\text{alt}}. \tag{5.17}$$

We can solve Eq. (5.17) through alternating optimization of $\mathbf{g}$ and $\mathbf{\Psi}$. At the nth iteration, we fix $\mathbf{\Psi}$ as the result from the previous iteration, which we denote as $\hat{\mathbf{\Psi}}^{(n-1)}$. The minimization problem for $\mathbf{g}^{(n)}$ then has a cost function in the form of Eq. (5.16):

$$\hat{\mathbf{g}}^{(n)} = \arg\min_{\mathbf{g}} \frac{1}{2\alpha} \left\| T\left\{\hat{\mathbf{\Psi}}^{(n-1)}\right\} - \mathbf{g} \right\|_2^2 + \|\mathbf{g}\|_{1,2,\text{alt}}. \tag{5.18}$$

It follows that $\hat{\mathbf{g}}^{(n)}$ is the projection of $T\{\hat{\mathbf{\Psi}}^{(n-1)}\}$ onto the (1,2,alt)-norm ball of radius $\max\{0, \|T\{\hat{\mathbf{\Psi}}^{(n-1)}\}\|_{1,2,\text{alt}} - \alpha\}$. This projection is given by [96]

$$\hat{\mathbf{g}}_{(i)}^{(n)} = \begin{cases} \frac{\max\{0, \|\mathbf{c}_{(i)}\|_2 - \alpha\}}{\|\mathbf{c}_{(i)}\|_2}\mathbf{c}_{(i)}, & \text{if } \|\mathbf{c}_{(i)}\|_2 \neq 0 \\ 0, & \text{otherwise} \end{cases}, \tag{5.19}$$

where $\mathbf{c} = T\{\hat{\mathbf{\Psi}}^{(n-1)}\}$.

With a fixed $\hat{\mathbf{g}}^{(n)}$, we then minimize Eq. (5.17) with respect to $\mathbf{\Psi}$. This is the quadratic

optimization problem

$$\hat{\boldsymbol{\Psi}}^{(n)} = \arg\min_{\boldsymbol{\Psi}} \sum_{q=1}^{Q} \left\| \mathbf{d}_q - \mathcal{U}\{\boldsymbol{\mathcal{F}}_{\mathbf{r}} \mathbf{S}_q \boldsymbol{\Psi} \hat{\boldsymbol{\Phi}}\} \right\|_2^2 + \frac{\lambda}{2\alpha} \| T\{\boldsymbol{\Psi}\} - \hat{\mathbf{g}}^{(n)} \|_2^2, \tag{5.20}$$

which we solve by the conjugate gradient method with initial guess $\hat{\boldsymbol{\Psi}}^{(n-1)}$.

Alternating optimization of Eq. (5.17) using the described procedure globally converges to the solution [95]

$$\hat{\boldsymbol{\Psi}} = \arg\min_{\boldsymbol{\Psi}} \sum_{q=1}^{Q} \left\| \mathbf{d}_q - \mathcal{U}\{\boldsymbol{\mathcal{F}}_{\mathbf{r}} \mathbf{S}_q \boldsymbol{\Psi} \hat{\boldsymbol{\Phi}}\} \right\|_2^2 + \lambda \sum_{i=1} h[T\{\boldsymbol{\Psi}\}_{(i)}]. \tag{5.21}$$

The alternating minimization steps are each straightforward to compute: as the closed-form solution to Eq. (5.18) is given by Eq. (5.19), and Eq. (5.20) can be efficiently solved using the conjugate gradient method (the closed-form solution generally requires inversion of matrices too large for direct computation).

The solution in Eq. (5.21) approximates the solution in Eq. (5.14) with increasing accuracy as $\alpha \to 0$. Convergence generally requires fewer iterations for higher values of α [94], so we combine the above alternating minimization algorithm with a continuation procedure [42,95]. In this procedure, a large initial α is used to solve Eq. (5.21), after which the resulting $\hat{\boldsymbol{\Psi}}$ is used as an initial guess to solve Eq. (5.21) with a smaller value of α. This process is repeated until α is small enough that Eq. (5.21) closely approximates Eq. (5.14). Alternating optimization with this continuation procedure converges globally to the solution in Eq. (5.21) corresponding to the final value of α [95].

Chapter 6

Experimental Results

6.1 Relative resolution and speed metrics

Spatial resolution and imaging speed will be reported in absolute terms as the Fourier pixel width in mm and as the temporal sampling rate of the navigator data in frames per second (fps), respectively. However, because the results in this chapter include images from rodent (i.e., rat and mouse) studies in addition to human studies, relative metrics normalized to the typical heart size and heart rate of each species will also be reported, facilitating comparison between images of different species. Here we establish standardized relative units of: a) spatial resolution in myocardial units (mu), where 1 mu = the species average normal thickness of the LV myocardium; and b) frame rate in frames per beat (fpb), where 1 fpb = the frame rate matching the species average normal resting heart rate. Tables 6.1 and 6.2 report the reference values and conversion factors employed for reporting resolution and speed in relative units.

Table 6.1: Relative spatial resolution units and conversion factors from absolute to relative units.

	Reference LV myocardial thickness	Conversion factor
Human	5.8 mm [97]	0.17 mu/mm
Rat	1.3 mm [98]	0.77 mu/mm
Mouse	0.67 mm [99]	1.5 mu/mm

Table 6.2: Relative frame rate units and conversion factors from absolute to relative units.

	Reference heart rate	Conversion factor
Human	75 bpm [100]	0.80 fpb/fps
Rat	400 bpm [101]	0.15 fpb/fps
Mouse	475 bpm [102]	0.13 fpb/fps

6.2 Implementation

All data for subspace-constrained imaging were collected according to the strategy outlined in Chapter 4. For $\mathcal{D}_{\text{img}}$, each $k_{y,j,2}$ was drawn from a set consisting of a) N_{ACS} central k_y-space locations with a sampling rate Δk_y satisfying the Nyquist condition, and b) additional k_y-space locations at the sampling rate $P\Delta k_y$. The readout direction is considered to be k_x by convention, and no $\mathbf{k}$-space undersampling was performed in the k_z direction. We produced the sampling schedule $\{(\mathbf{k}_{j,2}, t_{j,2})\}_{j=1,q=1}^{J_2,Q}$ from successive random permutations of the resulting (k_y, k_z)-space locations. The various implementations of $\mathcal{D}_{\text{nav}}$ will be specified for each set of results. Figure 6.1 illustrates a representative sampling pattern. All subspace-constrained imaging reconstructions were performed according to Eq. (5.1).

Experimental results include both human and animal subjects. All human experiments were approved by the local Institutional Review Board, and all subjects gave informed consent prior to scanning. All animals received humane care in compliance with the *Guide for the Care and Use of Laboratory Animals* published by the National Academy of Science [103],

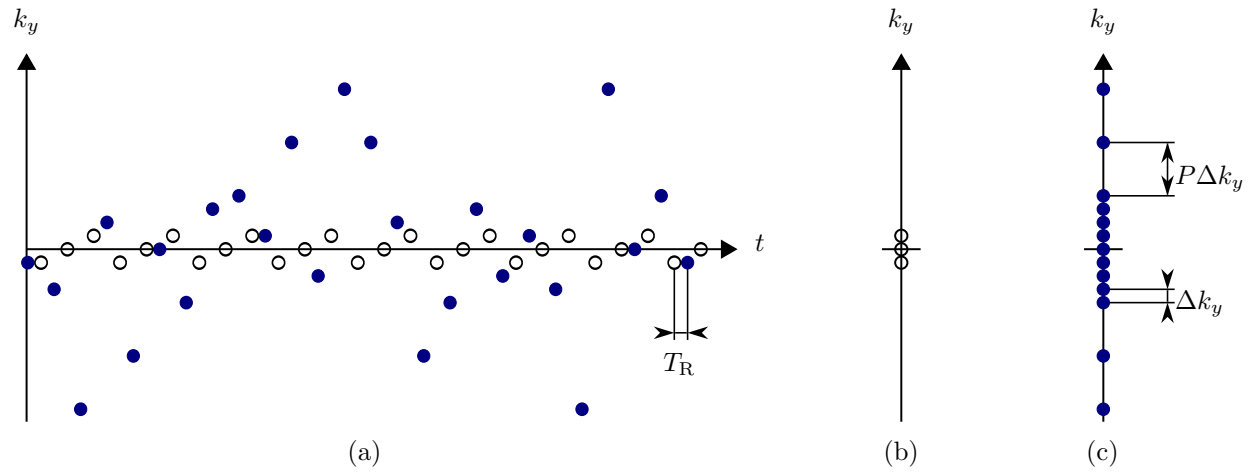

Figure 6.1: Illustrative example of the sampling patterns implemented throughout this chapter. Subfigure (a) depicts the $(\mathbf{k}, t)$-space sampling patterns for $\mathcal{D}_{\mathrm{nav}}$ (outlined circles) and $\mathcal{D}_{\mathrm{img}}$ (filled circles) for 2D imaging using interleaved-pulse navigation and parameters $N_{\mathrm{d}} = 3$, $N_{\mathrm{ACS}} = 9$, and $P = 4$. Subfigures (b) and (c) depict the $\mathbf{k}$-space sampling locations $\{\mathbf{k}_{j,1}\}_{j=1}^{J_1}$ and $\{\mathbf{k}_{j,2}\}_{j=1}^{J_2}$, respectively.

and the animal protocol was approved by the Carnegie Mellon University Institutional Animal Care and Use Committee.

6.3 Cine imaging

6.3.1 Data acquisition comparison

6.3.1.1 Rat subjects

To compare subspace estimation schemes *in vivo* in rats, we implemented different navigator schemes using customized FLASH pulse sequences. We modified the interleaved-pulse navigation strategy (Fig. 4.1-a) to use spiral navigators, and we performed self-navigation using a music note navigator. (Fig. 4.1-b). Both experiments used Cartesian trajectories to collect $\mathcal{D}_{\mathrm{img}}$. For reference, we also acquired 2D gated cine images using the Bruker IntraGate technique (Bruker BioSpin MRI, Ettlingen, Germany).

Experiments were conducted on a Bruker Avance AV1 4.7 T scanner equipped with a B-GA12 gradient set capable of 400 mT/m maximum gradient strength and a 4-channel array coil. Imaging data were collected with FA = 18°, FOV = 40 mm × 40 mm, matrix size = 256 × 256, spatial resolution = 0.16 mm × 0.16 mm (0.12 mu × 0.12 mu), slice thickness = 2 mm (1.5 mu), and imaging time = 5 min. Parallel acceleration was performed with $N_{\mathrm{ACS}} = 32$ and $P = 2$. The timing parameters for each imaging method were selected for maximum speed: the Cartesian- and spiral-navigated images were collected with $T_{\mathrm{E}} = 3.0$ ms and $T_{\mathrm{R}} = 6.8$ ms, for a frame rate of 74 fps (11 fpb); the self-navigated images were collected with $T_{\mathrm{E}} = 4.9$ ms and $T_{\mathrm{R}} = 10.5$ ms, for a frame rate of 95 fps (14 fpb); and the IntraGate images were collected with $T_{\mathrm{E}} = 3.6$ ms, $T_{\mathrm{R}} = 7.3$ ms, and 10 frames per cardiac cycle (analogous to 67 fps and 10 fpb). The animals used in the comparison study were Brown Norway (BN) rats. All data for subspace-constrained imaging were collected continually with neither ECG gating/triggering nor breath holding. Low-rank images were reconstructed with $L_1 = 16$, $L_2 = 24$ and shared regularization parameters.

Figure 6.2 shows representative images and spatiotemporal slices from each method. The IntraGate method only reconstructs a single representative cardiac cycle rather than "real-time" images; this cycle is repeated here to depict two cardiac cycles. The spiral-navigated images have a slightly higher frame rate than the gated images, and the self-navigated images are faster still, reaching 95 fps (14 fpb).

6.3.2 Image reconstruction comparison

6.3.2.1 Human subjects

We demonstrate the proposed approach *in vivo* in human subjects. We implemented the data acquisition scheme on a Siemens TRIO 3 T scanner using a customized FLASH pulse sequence and interleaved-pulse navigation. Typical imaging parameters were as follows:

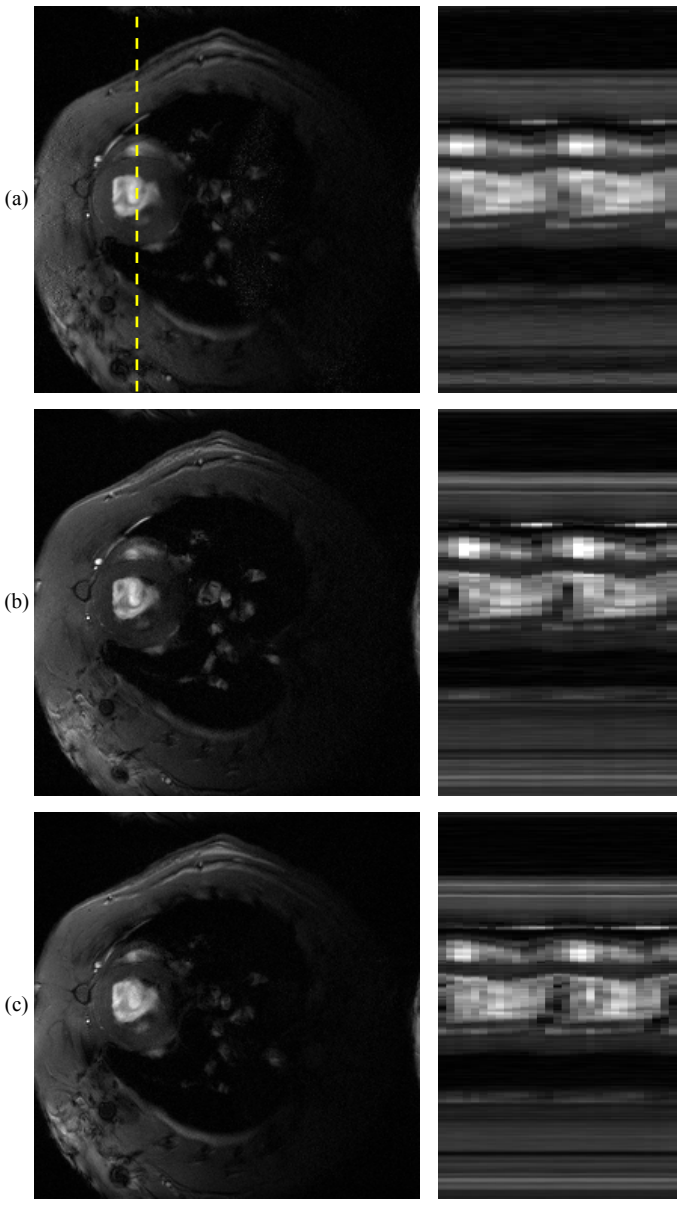

Figure 6.2: (a) Bruker IntraGate frame and a spatiotemporal slice through the dotted line, followed by frames and spatiotemporal slices of subspace-constrained images using (b) interleaved-pulse navigation with a spiral navigator trajectory, and (c) self-navigation with a music note trajectory. Gated scans reconstruct only a single representative cardiac cycle, so the same cycle is shown twice in (a). The spiral-navigated images have a slightly higher frame rate than the gated images, without the experimental burdens and sensitivities to arrhythmia and respiration associated with gated imaging. The self-navigated images share these benefits and are faster still, reaching 95 fps (14 fpb).

$T_{\mathrm{R}} = 4.6$ ms, $T_{\mathrm{E}} = 2.5$ ms, FA = 18°, FOV = 328 mm × 350 mm, matrix size 330 × 352, in-plane spatial resolution = 1.0 mm × 1.0 mm (0.17 mu × 0.17 mu), slice thickness = 6.0 mm (1.0 mu), $Q = 12$, $N_{\mathrm{d}} = 5$, $N_{\mathrm{ACS}} = 42$, and $P = 3$. The total acquisition time was 3 minutes. All data were collected continually with neither ECG gating nor breath holding. We reconstructed the sparsely sampled $(\mathbf{k}, t)$-space data according to the proposed model with $L_1 = 16$ and $L_2 = 48$, the proposed model with $L_1 = L_2 = 48$, and the full-rank (i.e., CS) model. All regularization parameters λ_1 and λ_2 were set according to Morozov's discrepancy principle [104]. Specifically, the data discrepancy of our reconstructions matches the expected discrepancy of a perfect, noiseless reconstruction: $\sum_{q=1}^{Q} \|\mathbf{d}_q - \mathcal{U}\{\boldsymbol{\mathcal{F}}_{\mathbf{r}}\mathbf{S}_q\hat{\boldsymbol{\Psi}}\hat{\boldsymbol{\Phi}}\}\|_2^2 = QJ\sigma^2$, where J is the number of measured samples per channel and σ^2 is the variance of the measurement noise. A data discrepancy $\sum_{q=1}^{Q} \|\mathbf{d}_q - \mathcal{U}\{\boldsymbol{\mathcal{F}}_{\mathbf{r}}\mathbf{S}_q\hat{\boldsymbol{\Psi}}\hat{\boldsymbol{\Phi}}\}\|_2^2 \ll QJ\sigma^2$ is associated with overfitting of noise, and a data discrepancy $\sum_{q=1}^{Q} \|\mathbf{d}_q - \mathcal{U}\{\boldsymbol{\mathcal{F}}_{\mathbf{r}}\mathbf{S}_q\hat{\boldsymbol{\Psi}}\hat{\boldsymbol{\Phi}}\}\|_2^2 \gg QJ\sigma^2$ is associated with model bias. We estimated σ^2 from our outermost $\mathbf{k}$-space data, which have a low signal-to-noise ratio. Figure 6.3 depicts an end-diastolic frame from the reconstruction with $L_1 = 16$ and $L_2 = 48$ as well as spatiotemporal slices through the left ventricle from all reconstructions. The frame rate of all reconstructions is 22 fps (17 fpb).

A similar experimental procedure was used to demonstrate the effectiveness of the proposed approach in human subjects with cardiac arrhythmias. The imaging protocol remained the same, with specific imaging parameters as follows: $T_{\mathrm{R}} = 4.3$ ms, $T_{\mathrm{E}} = 2.5$ ms, FA = 18°, FOV = 286 mm × 340 mm, matrix size = 130 × 192, in-plane spatial resolution = 2.2 mm × 1.8 mm (0.38 mu × 0.31 mu), slice thickness = 7.0 mm (1.2 mu), $Q = 12$, $N_{\mathrm{d}} = 5$, $N_{\mathrm{ACS}} = 32$, and $P = 3$. The total acquisition time was 2 minutes. We performed reconstruction according to the proposed model with $L_1 = 15$ and $L_2 = 64$, the proposed model with $L_1 = L_2 = 64$, and the full-rank (i.e., CS) model. All regularization parameters λ_1 and λ_2 were set according to Morozov's discrepancy principle. Figure 6.4 depicts an end-diastolic frame from the reconstruction with $L_1 = 15$ and $L_2 = 64$ as well as spatiotemporal

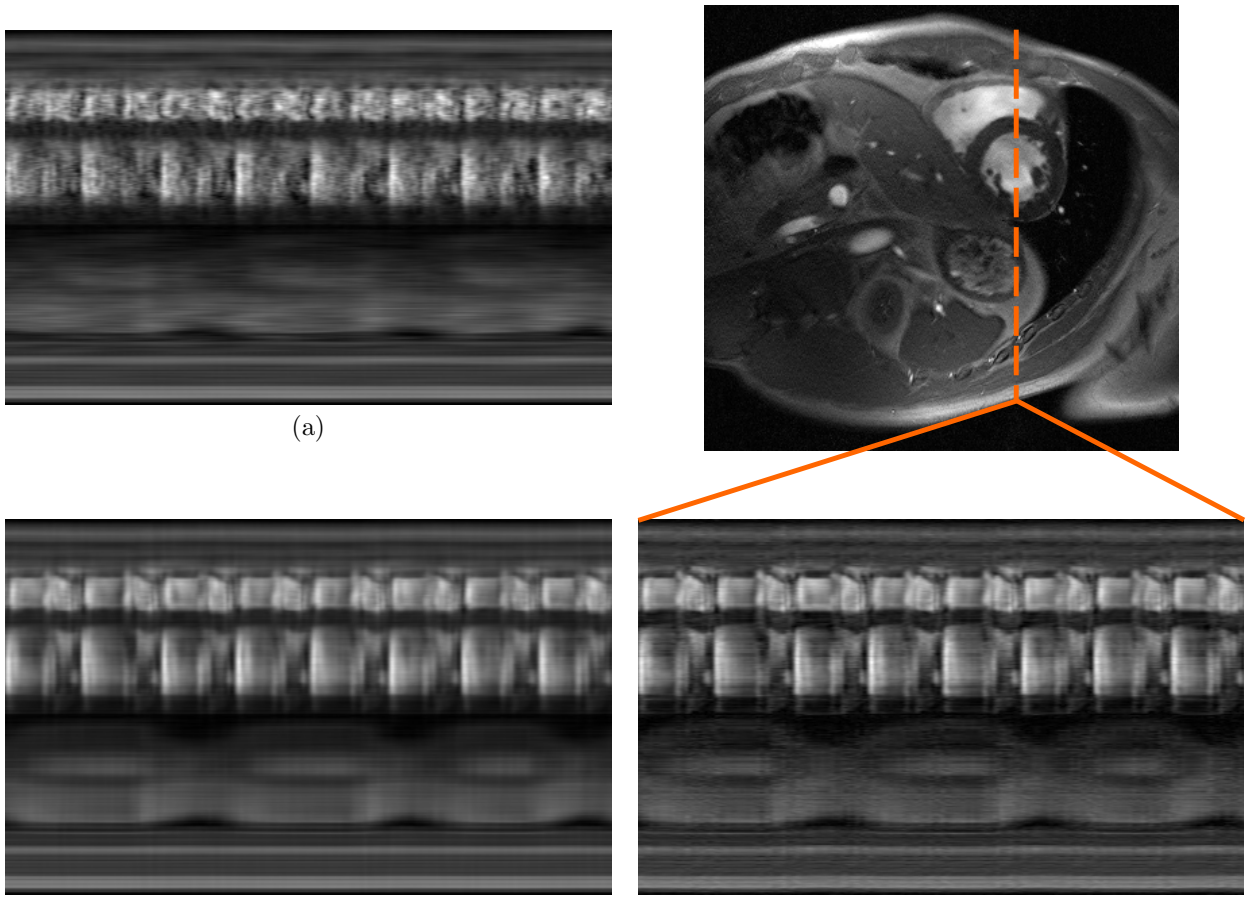

(a) (b) (c)

Figure 6.3: End-diastolic cardiac frame and spatiotemporal slices from human experimental results using (a) the full-rank (i.e., CS) model, (b) the proposed model with $L_1 = L_2$, and (c) the proposed model with $L_1 < L_2$.

slices through the left ventricle from all reconstructions. The frame rate of all reconstructions is 23 fps (19 fpb).

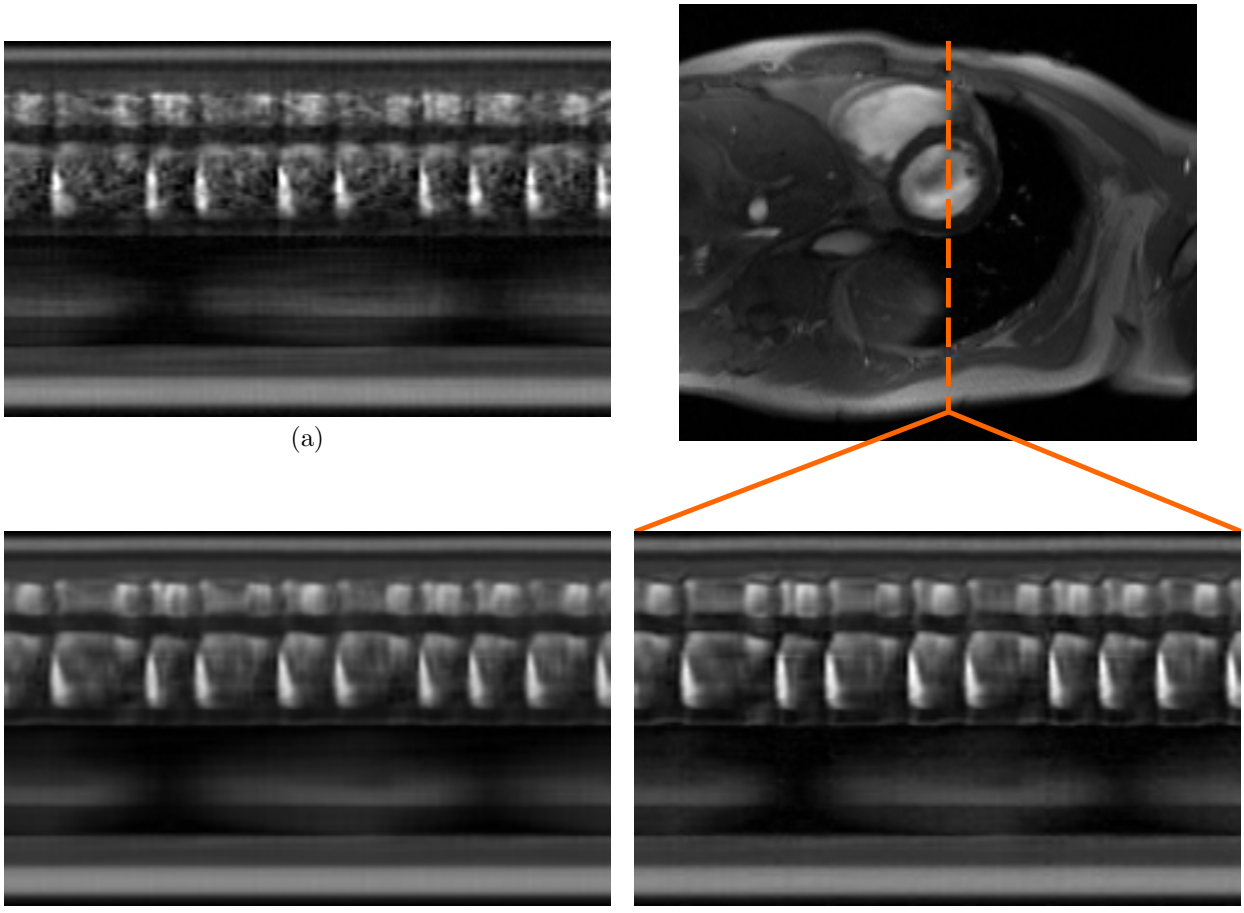

(a)

(c)

(b)

Figure 6.4: End-diastolic cardiac frame and spatiotemporal slices from arrhythmic human experimental results using (a) the full-rank (i.e., CS) model, (b) the proposed model with $L_1 = L_2$, and (c) the proposed model with $L_1 < L_2$.

6.3.3 Spatiotemporal resolution demonstration

6.3.3.1 Mouse subjects

Mouse imaging is a particularly challenging application of cardiac MRI due to very high spatial and temporal resolution requirements. Mice have even smaller hearts and higher heart

rates than do rats, making ungated, free-breathing cardiac imaging particularly difficult to perform. Here we employ self-navigation to image myocardial wall motion in mice at 0.12 mm $\times$ 0.12 mm (0.18 mu $\times$ 0.18 mu) spatial resolution with a frame rate of 97 fps (12 fpb).

Experiments were conducted on a Bruker Avance III 7 T scanner equipped with a B-GA12S32 gradient set capable of 480 mT/m maximum gradient strength and a quadrature surface coil. A customized FLASH pulse sequence with self-navigation was employed to collect imaging data with FA = 18°, FOV = 30 mm $\times$ 30 mm, matrix size = 256 $\times$ 256, slice thickness = 1 mm (1.5 mu), and imaging time = 11 min. No parallel acceleration was performed. Images were collected with T_{E} = 5.1 ms and T_{R} = 10.3 ms. Data were collected continually with neither ECG gating/triggering nor breath holding. Images were reconstructed with L_1 = 16 and L_2 = 24. Figure 6.5 shows a representative frame and spatiotemporal slice from a mouse subject.

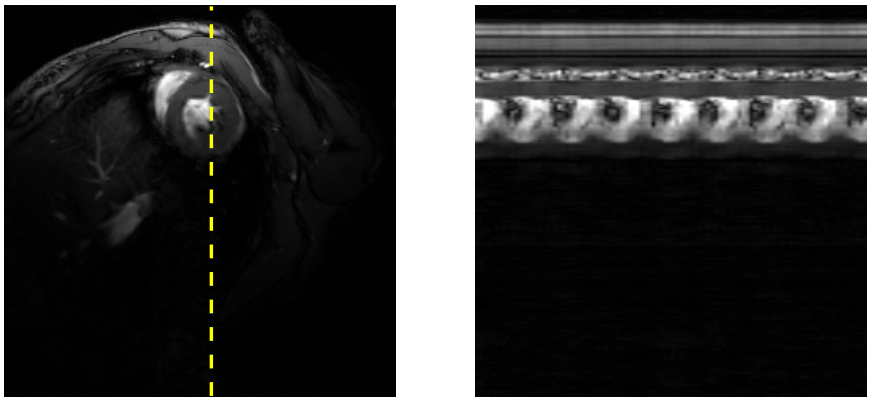

Figure 6.5: Single frame and spatiotemporal slice of a mouse heart using music note self-navigation. At 0.12 mm $\times$ 0.12 mm spatial resolution (0.18 mu $\times$ 0.18 mu) and 97 fps (12 fpb), these images show the capability of self-navigated imaging

6.4 Myocardial perfusion imaging

6.4.1 Acute transplant rejection

6.4.1.1 2D rat imaging

The ability to assess organ rejection is crucial to the survival of heart transplant recipients. The current clinical standard for detection of acute rejection is endomyocardial biopsy, an invasive procedure that can lead to significant complications and/or missed diagnoses [105]. Cardiovascular MRI has shown promise for noninvasive assessment of the immune response in transplanted hearts [106], but like many other cardiac MRI applications suffers from low imaging speeds. Here we demonstrate integrated anatomical (i.e., EF) and functional (i.e., first-pass myocardial perfusion) assessments of *in vivo* transplanted rat hearts from a single scan.

Allograft heart and lung transplants were performed from male Dark Agouti to male BN rats, with each recipient gaining an additional heart and lung in the abdomen while the native organs supported life. The allograft hearts underwent different degrees of rejection over time, experiencing moderate rejection on post-operational day (POD) 5; by POD 7, the majority of the allograft hearts had become severely rejected. *In vivo* MRI scans were performed on POD 5 and POD 7 for longitudinal monitoring of rejection on the same animals. Ungated images of cardiac motion, respiratory motion, and first-pass myocardial perfusion were acquired on the Bruker Avance III 7 T scanner described in Section 6.3.3.1 using a customized FLASH pulse sequence with interleaved-pulse navigation. The images were collected with the following parameters: T_{R} = 10.4 ms, T_{E} = 2.7 ms, FOV = 40 mm × 40 mm, matrix size = 256 × 256 ×, in-plane spatial resolution = 0.16 mm × 0.16 mm (0.12 mu × 0.12 mu), slice thickness = 2 mm (1.5 mu), $Q = 1$, $N_{\mathrm{d}} = 1$, and $P = 1$. The total acquisition time was 6 minutes. All data were collected continually with neither ECG gating/triggering nor breath

holding. Dynamic contrast enhancement for first-pass myocardial perfusion imaging was performed by injecting a 0.2 mmol/kg bolus of gadolinium contrast agent into each subject after the start of data acquisition. The resulting frame rate of each reconstruction was equal to 48 fps (7 fpb). No gating, triggering, or breath holding was used.

Figure 6.6 shows typical anatomical results from POD 5 and POD 7 for the same subject. Snapshots from end-diastolic cardiac phases are pictured, as well as spatiotemporal slices through the dotted lines. EF was relatively low by POD 5 and virtually zero by POD 7, strongly indicating acute rejection of the transplanted heart; the heart rate also declined. Figure 6.7 depicts baseline-corrected myocardial perfusion curves from POD 7, taken from the same scan depicted in 6.6. A large perfusion defect is apparent across the mid-ventricular inferior, inferolateral, and anterolateral myocardial segments.

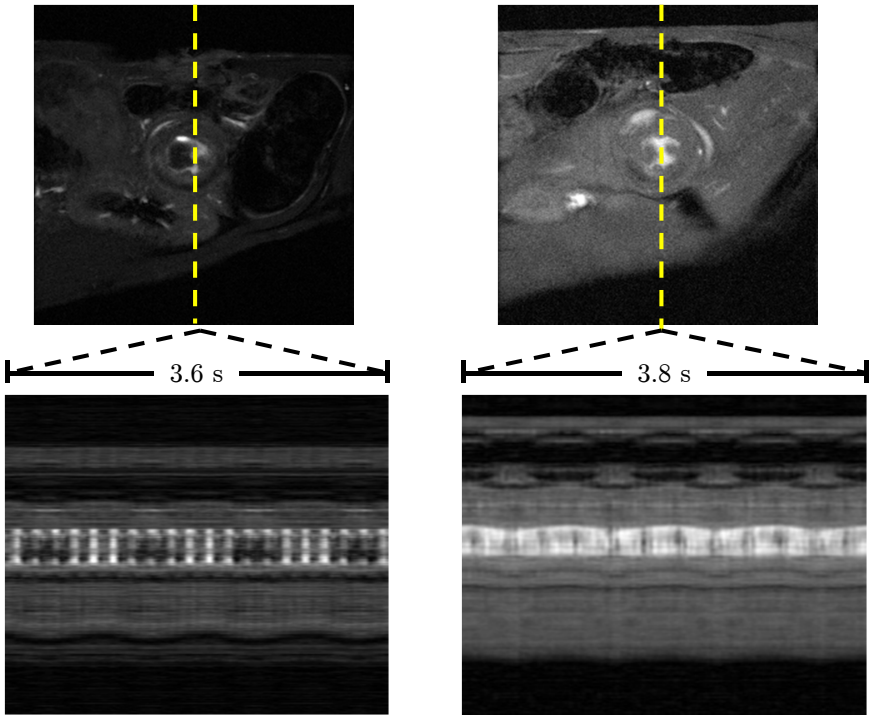

Figure 6.6: End-diastolic cardiac frames and spatiotemporal slices from post-operational days (a) POD 5 and (b) POD 7. The later scan shows large reductions in EF and heart rate.

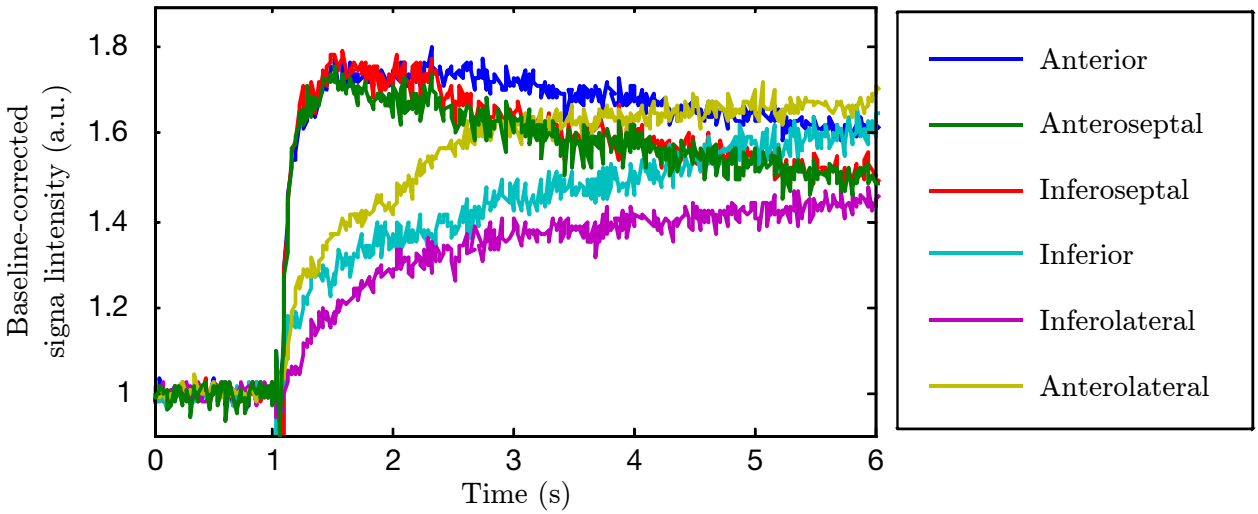

Figure 6.7: Baseline-corrected signal intensity curves from six mid-ventricular myocardial segments on POD 7. Severe hypoperfusion is evident in the inferior, inferolateral, and anterolateral segments.

6.4.2 Acute myocardial infarction

6.4.2.1 3D rat imaging

To demonstrate the proposed approach *in vivo* in rats, we implemented the data acquisition scheme on the Bruker Avance AV1 4.7 T scanner described in Section 6.3.1.1 using a customized FLASH pulse sequence with interleaved-pulse navigation. The images were collected with the following parameters: $T_{\mathrm{R}} = 7.5$ ms, $T_{\mathrm{E}} = 2.4$ ms, FA = 18°, FOV = 40 mm × 40 mm × 40 mm, matrix size = 62 × 62 × 128, spatial resolution = 0.65 mm × 0.65 mm × 0.31 mm (0.50 mu × 0.50 mu × 0.24 mu), $Q = 4$, $N_{\mathrm{d}} = 1$, and $P = 1$. The total acquisition time was 24 minutes. All data were collected continually with neither ECG gating/triggering nor breath holding. Dynamic contrast enhancement for first-pass myocardial perfusion imaging was performed by injecting a 0.2 mmol/kg bolus of gadolinium contrast agent into each subject after the start of data acquisition. The animals used in the study were BN rats with and without acute myocardial infarction induced by ligation of the left anterior descending (LAD) coronary artery.

We reconstructed the sparsely sampled $(\mathbf{k}, t)$-space data according to the proposed model with $L_1 = 15$ and $L_2 = 48$ and the proposed model with $L_1 = L_2 = 48$. The full-rank (i.e., CS) solution was not computed due to memory constraints. All regularization parameters λ_1 and λ_2 were set according to Morozov's discrepancy principle. Figure 6.8 depicts end-systolic frames from the reconstruction with $L_1 = 15$ and $L_2 = 48$ as well as spatiotemporal slices from each reconstruction. The frame rate of all reconstructions is 67 fps (10 fpb). Figure 6.9 depicts baseline-corrected signal intensity curves from the four apical segments of the myocardium in rats with and without ligation of the LAD coronary artery [107].

6.4.3 Ischemic reperfusion injury

6.4.3.1 3D rat imaging

Here we demonstrate integrated whole-heart 3D imaging of myocardial wall motion, first-pass perfusion, and LGE using interleaved-pulse navigation with a cone navigator trajectory.

For this application, we employed a rodent ischemic reperfusion injury (IRI) animal model using male BN rats. For IRI experiments, rats had a 45 min transient left circumflex (LCx) coronary artery occlusion followed by re-perfusion. For control rats, no coronary artery occlusion was performed. Contrast enhancement was performed in all subjects by injecting a 0.2 mmol/kg bolus of gadolinium contrast agent 5 minutes after the start of data acquisition. For reference, the 2D IntraGate method was used to image a mid-ventricular slice before and after each 3D imaging experiment.

Experiments were conducted on the Bruker Avance AV1 4.7 T scanner described in Section 6.3.1.1. 3D imaging data were collected with FA = 10°, FOV = 40 mm × 40 mm × 24 mm, matrix size = 128 × 128 × 24, spatial resolution = 0.31 mm × 0.31 mm × 1.0 mm (0.24 mu × 0.24 mu × 0.77 mu), $N_{\mathrm{ACS}} = 24$, $P = 2$, $T_{\mathrm{E}} = 2.5$ ms, and $T_{\mathrm{R}} = 6.8$ ms, for a frame rate of 74 fps (11 fpb). At 16 minutes, imaging time was short enough to re-

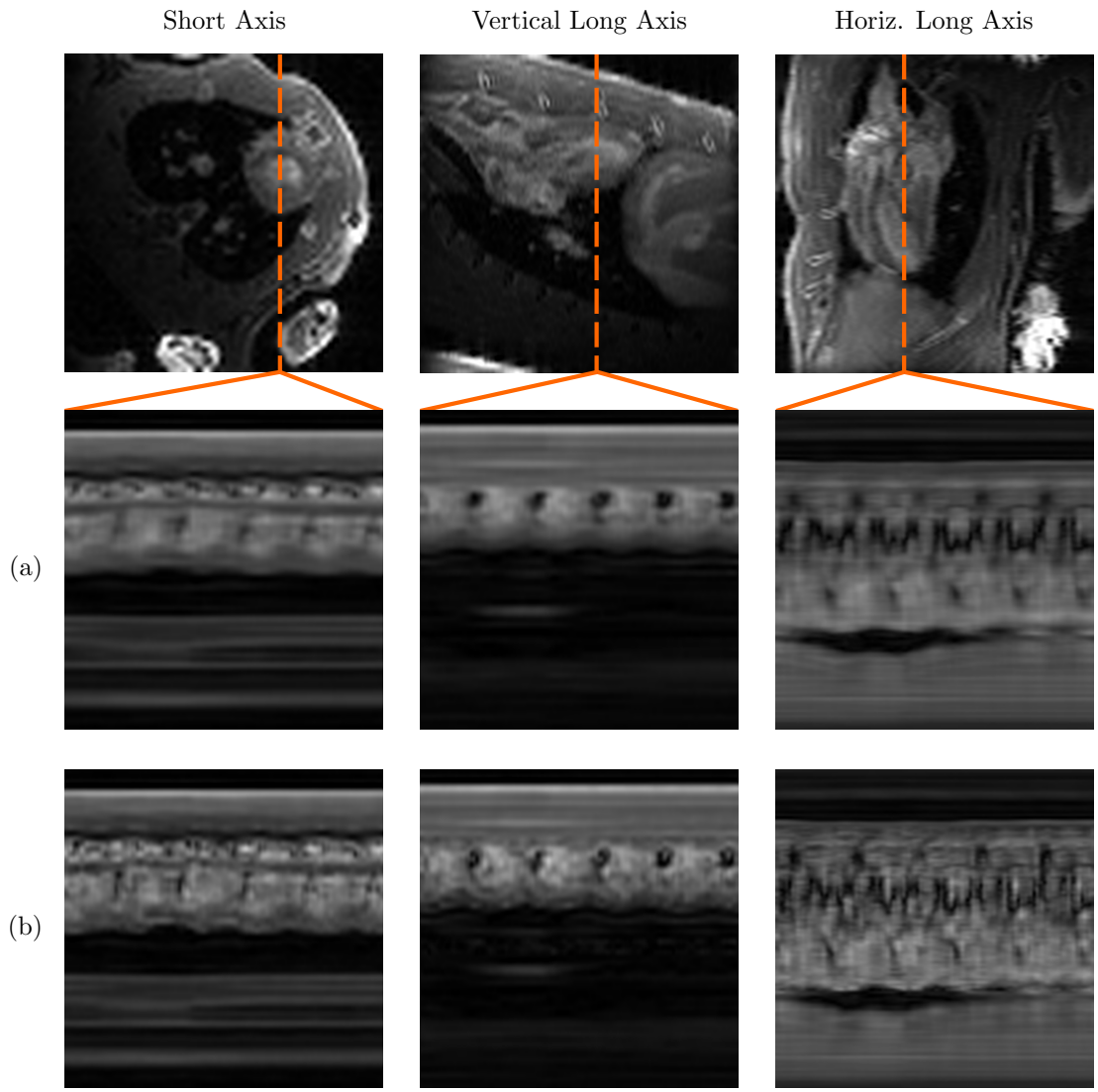

Figure 6.8: End-systolic cardiac frames and spatiotemporal slices from experimental results in rats using (a) the proposed model $L_1 = L_2$, and (b) the proposed model with $L_1 < L_2$.

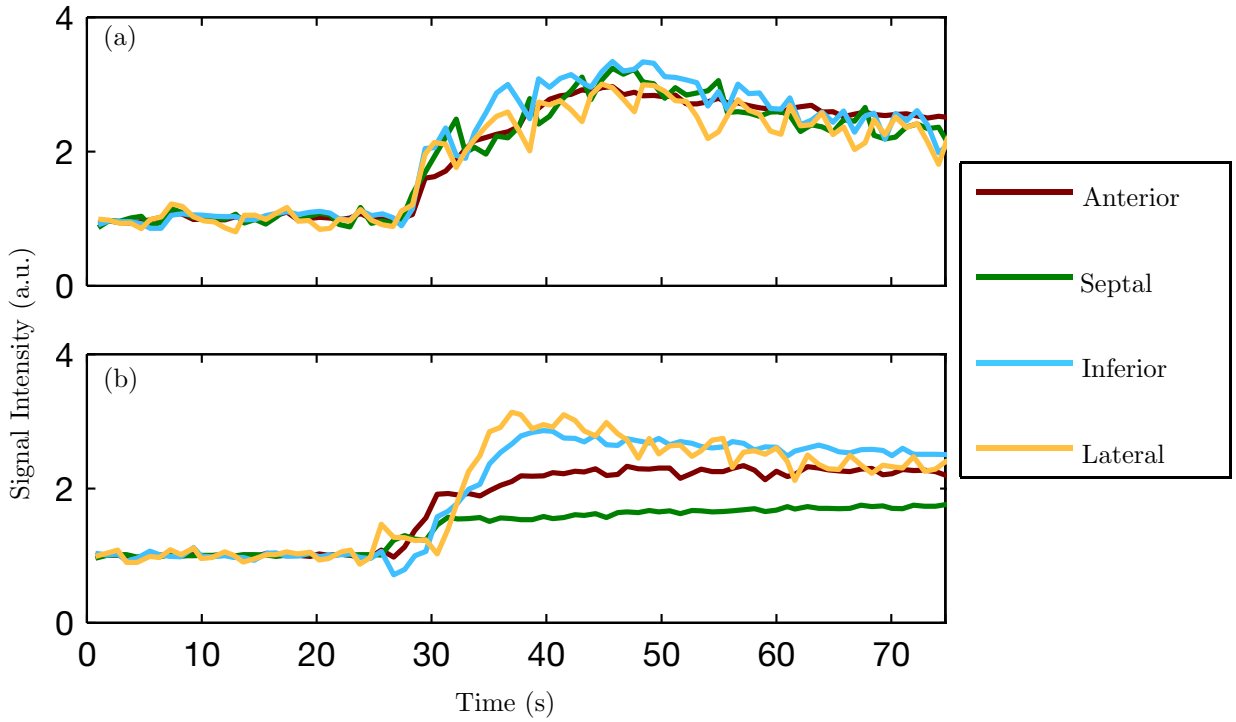

Figure 6.9: Baseline-corrected signal intensity curves from apical segments of the myocardium in (a) a healthy rat, and (b) a rat with a ligated LAD coronary artery.

main practical and long enough to collect both first-pass and delayed myocardial perfusion images. All data for subspace-constrained imaging were collected continually with neither ECG gating/triggering nor breath holding, using interleaved-pulse navigation. 3D subspace-constrained images were reconstructed with $L_1 = L_2 = 24$. IntraGate images were collected using the same parameters as the IntraGate images in Section 6.3.1.1.

Figure 6.10 shows pre- and post-contrast images of an IRI subject on the day of surgery. The figure shows both 2D IntraGate and 3D cone-navigated subspace-constrained images in order to compare the extent of the perfusion defect imaged by both methods. Figure 6.11 shows bullseye plots depicting time to peak concentration (TPC) of the first pass of contrast agent through the myocardium of a) a control subject, and b) the same IRI subject as in Fig. 6.10. The bullseye plots conform to the American Heart Association 17-segment standard [108].

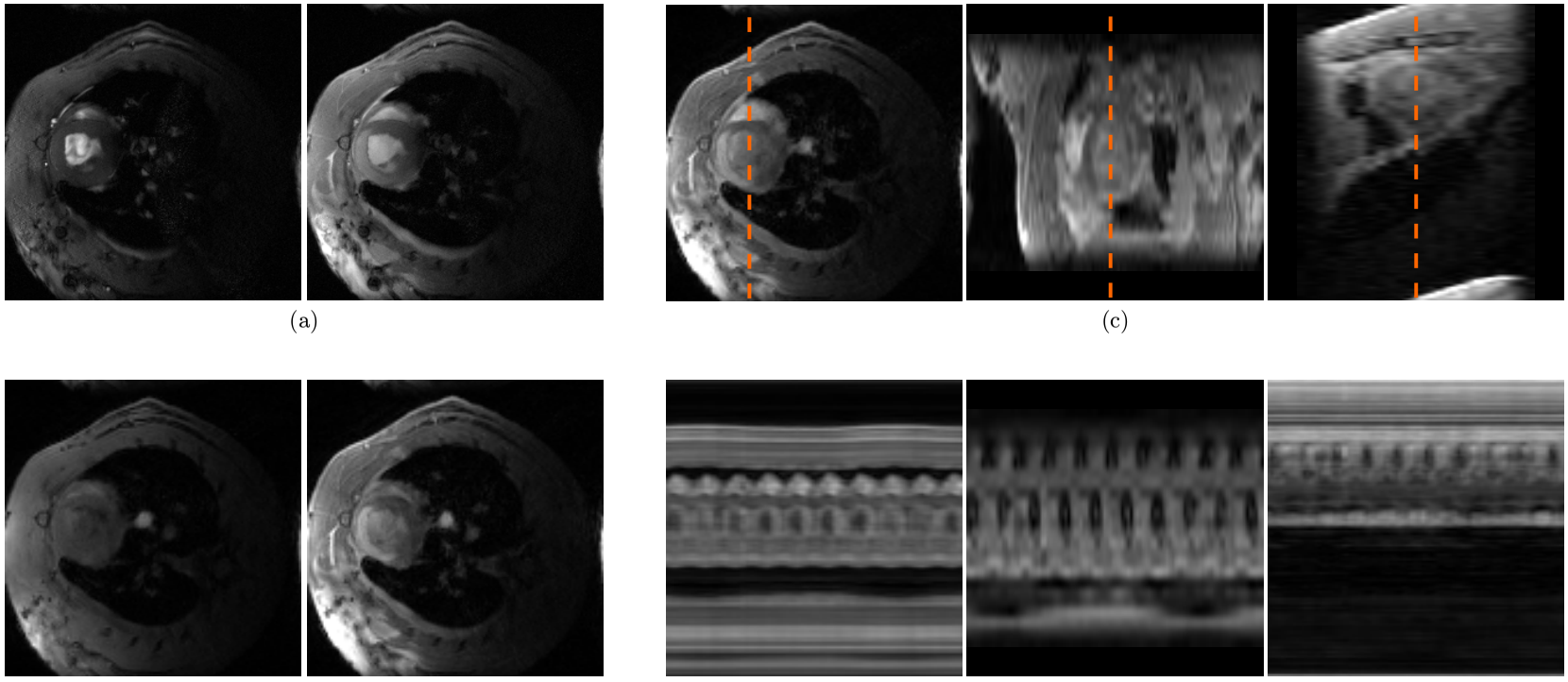

Figure 6.10: Representative IRI images on the day of surgery. (a) 2D IntraGate images pre- and post-contrast, (b) corresponding slices from 3D cone-navigated images pre- and post-contrast, (c) three perpendicular views of the 3D cone-navigated images post-contrast, and (d) spatiotemporal slices through the dotted lines. The extent of the in-plane LGE perfusion defect match in (a) and (b). The images in (a) and (b) have different contrast due to the differences between slice and slab excitation. The spatial-coverage benefit of 3D imaging can be seen in (c), which shows how far the perfusion defect extends towards the apex of the heart.

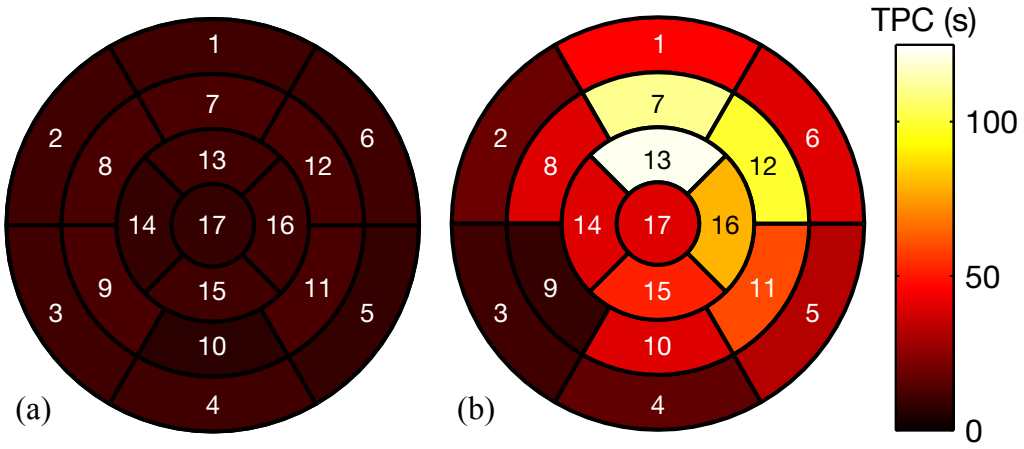

Figure 6.11: 17-segment bullseye plots showing time to peak concentration (TPC) for: (a) a control rat; (b) a rat with IRI (the same rat shown in Fig. 6.10). The TPC measurements in (b) indicate extensive myocardial damage compared to (a), especially in the apical anterior, mid-ventricular anterior, mid-ventricular anterolateral, and apical lateral segments, consistent with the LGE images in Fig. 6.10

6.5 Extracellular volume fraction mapping

6.5.1 Modeling multiple contrasts

The image contrast equations for many fast imaging sequences (e.g., FLASH) assume that the system has been driven into a steady state after multiple RF pulses. It is therefore impossible to quickly cycle through different contrasts using these sequences, so multiple contrasts must be collected asynchronously instead. Using FLASH imaging, we are therefore concerned with the matrix of H image sequences $\{\rho_h(\mathbf{r},t)\}_{h=1}^{H}$ (each with different image contrast) concatenated along the time dimension:

$$\mathbf{C}_{\text{mult}} = \begin{bmatrix} \mathbf{C}(\rho_1) & \mathbf{C}(\rho_2) & \cdots & \mathbf{C}(\rho_H) \end{bmatrix}. \tag{6.1}$$

A trivial extension of explicit-subspace low-rank imaging for multiple asynchronous contrasts could independently model each $\rho_h(\mathbf{r},t)$ as being Lth-order partially separable, with

$M \times N$ Casorati matrix representation $\mathbf{C}(\rho_h) = \mathbf{\Psi}_h \mathbf{\Phi}_h$. This would induce the structure

$$\mathbf{C}_{\text{mult}} = \begin{bmatrix} \mathbf{\Psi}_1\mathbf{\Phi}_1 & \mathbf{\Psi}_2\mathbf{\Phi}_2 & \cdots & \mathbf{\Psi}_H\mathbf{\Phi}_H \end{bmatrix} = \begin{bmatrix} \mathbf{\Psi}_1 & \mathbf{\Psi}_2 & \cdots & \mathbf{\Psi}_H \end{bmatrix} \begin{bmatrix} \mathbf{\Phi}_1 & \mathbf{0} & \cdots & \mathbf{0} \\ \mathbf{0} & \mathbf{\Phi}_2 & \cdots & \mathbf{0} \\ \vdots & & \ddots & \vdots \\ \mathbf{0} & \mathbf{0} & \cdots & \mathbf{\Phi}_H \end{bmatrix}, \quad (6.2)$$

which implies that $\text{rank}(\mathbf{C}_{\text{mult}}) \leq HL$. Image reconstruction could then be performed by: a) determining each $\mathbf{\Phi}_h \in \mathbb{C}^{L \times N}$ from the L most significant right singular vectors of $C(\mathcal{D}_{\text{nav},h})$; and b) determining the MHL unknowns in $\{\mathbf{\Psi}_h \in \mathbb{C}^{M \times L}\}_{h=1}^{H}$ by reconstructing each $\mathbf{\Psi}_h$ from $\mathcal{D}_{\text{img},h}$.

However, the above approach neglects the strong correlation between images of different contrasts [109, 110]. This correlation implies that $\{\mathbf{C}(\rho_h)\}_{h=1}^{H}$ belong to a shared spatial subspace of dimension $K < HL$, and that the matrix $\mathbf{C}_{\text{mult}}$ can instead be modeled as

$$\mathbf{C}_{\text{mult}} = \mathbf{\Psi}_{\text{mult}} \begin{bmatrix} \mathbf{\Phi}_1 & \mathbf{\Phi}_2 & \cdots & \mathbf{\Phi}_H \end{bmatrix}, \quad (6.3)$$

with $\text{rank}(\mathbf{C}_{\text{mult}}) \leq K < HL$. Image reconstruction can then be performed by: a) jointly determining $[\mathbf{\Phi}_1 \quad \mathbf{\Phi}_2 \quad \cdots \quad \mathbf{\Phi}_H] \in \mathbb{C}^{K \times HN}$ from the K most significant right singular vectors of $[\mathbf{C}(\mathcal{D}_{\text{nav},1}) \quad \mathbf{C}(\mathcal{D}_{\text{nav},2}) \quad \cdots \quad \mathbf{C}(\mathcal{D}_{\text{nav},H})]$; and b) determining the $MK < MHL$ unknowns in $\mathbf{\Phi}_{\text{mult}} \in \mathbb{C}^{M \times K}$ by reconstructing $\mathbf{\Phi}_{\text{mult}}$ from $\{\mathcal{D}_{\text{img},h}\}_{h=1}^{H}$. We will compare approaches employing the individual and joint models for ECV mapping via variable-angle FLASH T_1 mapping.

6.5.2 Results

6.5.2.1 3D rat imaging

For this application, we employed a rodent IRI animal model using male BN rats. Rats had a 45 min transient LCx coronary artery occlusion followed by re-perfusion. Data were collected on the Bruker Avance AV1 4.7 T scanner described in Section 6.3.1.1. Imaging data with four successive image contrasts (FA = $3°, 19°, 22°, 28°$) were collected using a FLASH pulse sequence. A 0.2 mmol/kg bolus of gadolinium contrast agent was then administered, followed by a repeat of the previous four-contrast imaging protocol during the gadolinium steady-state. Each of the $H = 8$ individual datasets were collected with 3D encoding, FOV = 40 mm $\times$ 40 mm $\times$ 24 mm, matrix size = 96 $\times$ 96 $\times$ 24, spatial resolution = 0.42 mm $\times$ 0.42 mm $\times$ 1.0 mm (0.32 mu $\times$ 0.32 mu $\times$ 0.77 mu), $N_{\mathrm{ACS}} = 24$, $P = 2$, $T_{\mathrm{E}} = 2.5$ ms, $T_{\mathrm{R}} = 10$ ms (for a frame rate of 50 fps = 8 fpb) and imaging time = 10 minutes. All data were collected continually with neither ECG gating/triggering nor breath holding, using interleaved-pulse cone navigation.

Figure 6.12 compares the NRMS error of low-rank approximations of $\mathcal{D}_{\mathrm{nav}}$ using the individual structure of Eq. 6.2 to the error using the joint subspace structure of Eq. 6.3. Collecting $H = 8$ individual rank-L Eckart–Young approximations of each $\mathcal{D}_{\mathrm{nav},h}$ results in a total model order $8L$, as compared to a total model order K for the rank-K joint Eckart–Young approximation of $\mathcal{D}_{\mathrm{nav}}$. As expected, the joint model can more accurately represent the data for any given total model order.

We compared the image quality of individual and joint reconstruction, selecting model orders for the individual case based on the singular values of each $C(\mathcal{D}_{\mathrm{nav},h})$, and for the joint case based on the singular values of $[\mathbf{C}(\mathcal{D}_{\mathrm{nav},1}) \quad \mathbf{C}(\mathcal{D}_{\mathrm{nav},2}) \quad \cdots \quad \mathbf{C}(\mathcal{D}_{\mathrm{nav},H})]$. The same singular value cutoff was used to compare cases: $\sigma_\ell/\sigma_1 = 0.002$, resulting in model orders $L = 23$ and $K = 28$. Figure 6.13 shows one slice from a post-contrast frame of the image

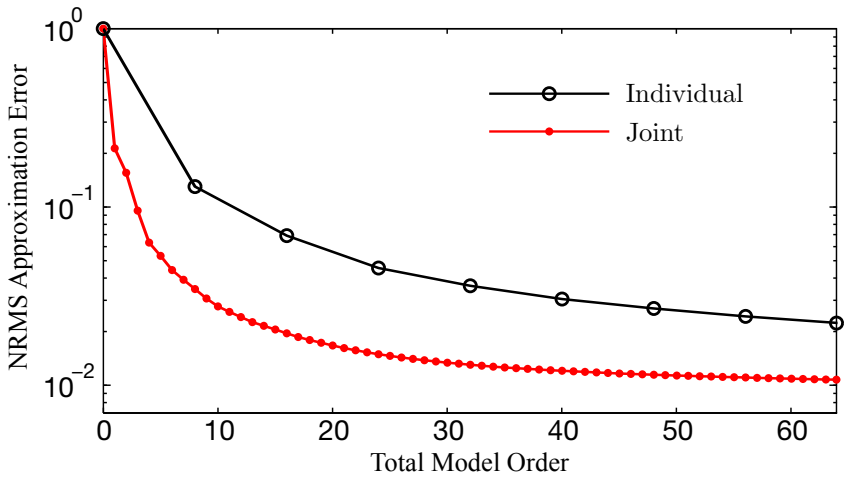

Figure 6.12: NRMS error of low-rank approximations of $\mathcal{D}_{\text{nav}}$, employing either the individual subspace structure of Eq. 6.2 or the joint subspace structure of Eq. 6.3. The collection of $H = 8$ individual rank-L Eckart–Young approximations of each $\mathcal{D}_{\text{nav},h}$ corresponds to total model order $8L$; the rank-K joint Eckart–Young approximation of $\mathcal{D}_{\text{nav}}$ corresponds to total model order K. The data can be far more efficiently represented using the joint model.

with FA = 28°, reconstructed (a) individually and (b) jointly alongside other contrasts. The individually reconstructed image suffers from motion and aliasing artifacts, a byproduct of the shorter scan time (per contrast) and longer T_{R} (for increased T_1 weighting) as compared to other 3D results in this chapter. The image quality of the joint reconstruction is clearly superior.

After joint reconstruction of all eight images, a correlation analysis of the temporal basis functions $\{\varphi_\ell\}_{\ell=1}^{K}$ extracted synchronized respiratory cycles. We then solved Eq. (2.35) by a direct search method [111] to obtain T_1 at each voxel both before and after administration of contrast agent; amplitude values were calculated according to Eq. (2.34), and ECV was calculated according to Eq. (2.51). Figure 6.14 shows a slice from the 3D fitted amplitude and R_1 maps, pre- and post-contrast, as well as LV myocardial ECV overlaid on an amplitude map. The region of elevated ECV clearly indicates the reperfusion injury.

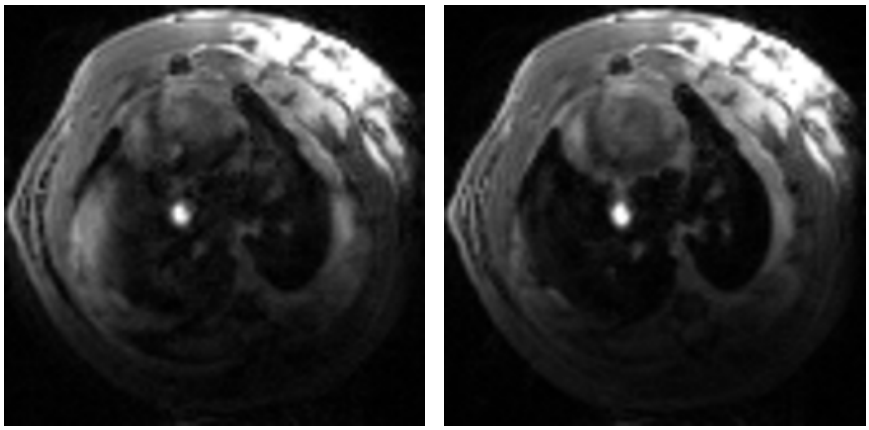

(a) (b)

Figure 6.13: Slice from a post-contrast frame (FA = 28°), reconstructed either (a) individually or (b) jointly with the images of other contrasts. The individually reconstructed image suffers from motion and aliasing artifacts; joint reconstruction offers a noticeable improvement in image quality.

6.6 Labeled cell imaging

6.6.1 Data acquisition comparison

6.6.1.1 Rat subjects

To demonstrate the increased speed offered by self-navigation specifically for T_2^*-weighted imaging, we have compared navigation strategies for cardiac imaging of healthy BN rats. We implemented both customized FLASH pulse sequences shown in Fig. 4.1: the interleaved-pulse navigation strategy in Fig. 4.1-a and the music note self-navigation strategy in Fig. 4.1-b. Imaging data were collected using FOV = 40 mm × 40 mm, matrix size = 256 × 256, spatial resolution = 0.16 mm × 0.16 mm (0.12 mu × 0.12 mu), slice thickness = 2 mm (1.5 mu), and imaging time = 5 min. Parallel acceleration was performed with $N_{\mathrm{ACS}} = 32$ and $P = 2$. Typical timing parameters were $T_{\mathrm{R}} = 10.5$ ms, $T_{\mathrm{E}} = 5.0$ ms, resulting in a frame rate of 48 fps (7 fpb) for interleaved-pulse navigation and a frame rate of 95 fps (14 fpb) for self-navigation. All data were collected continually with neither ECG gating/triggering nor

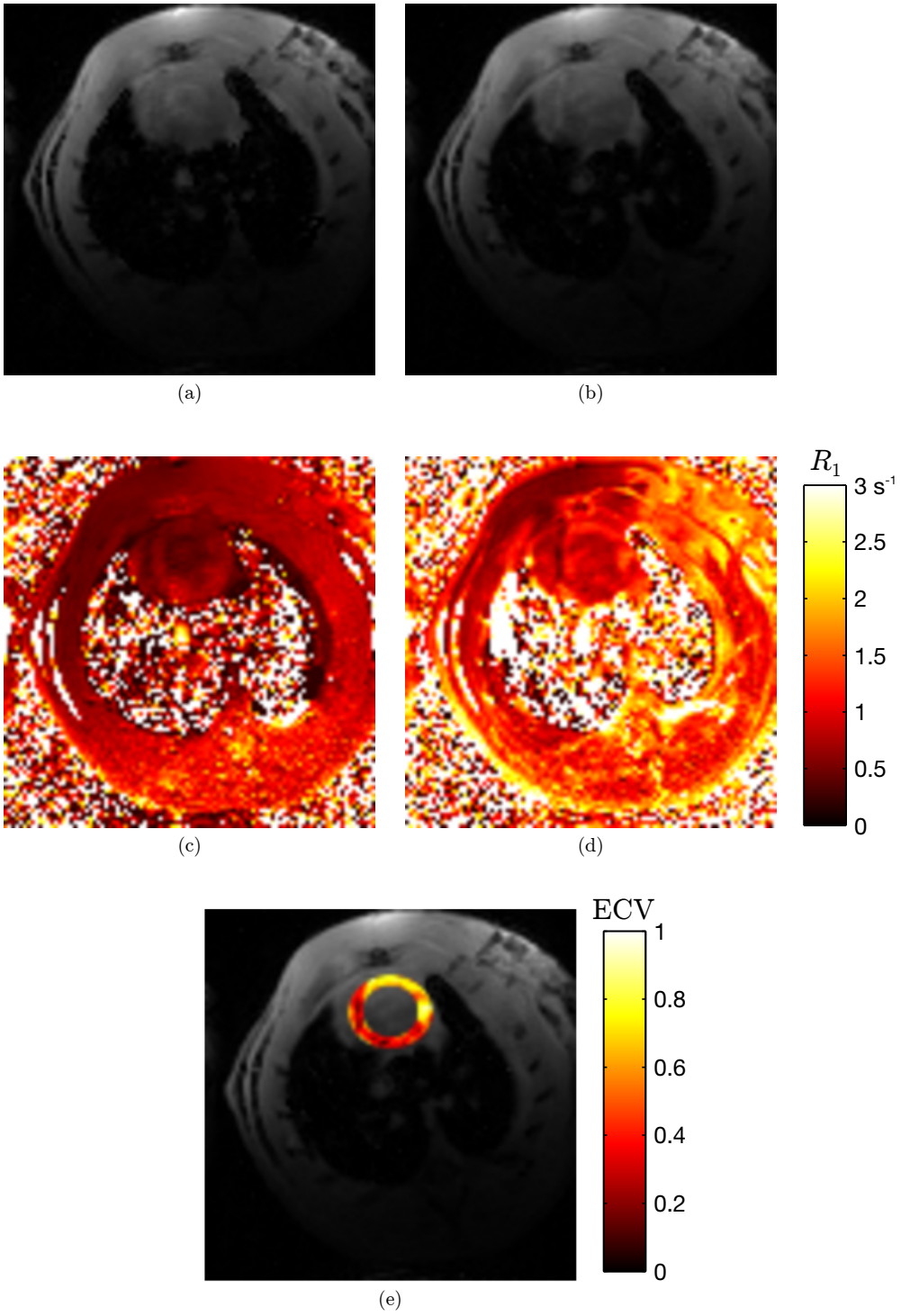

Figure 6.14: Slice from 3D fitted amplitude maps (a) pre-contrast and (b) post-contrast, slice from 3D R_1 maps (c) pre-contrast and (d) post-contrast, and (e) ECV map of the LV myocardium overlaid on an amplitude map. Elevated ECV measurements indicate the reperfusion injury.

breath holding on the Bruker Avance AV1 4.7 T scanner described in Section 6.3.1.1. Images were reconstructed using $L_1 = 16$ and $L_2 = 24$, with regularization parameters set according to Morozov's discrepancy principle. Figure 6.15 depicts spatiotemporal slices through the heart using (a) interleaved-pulse navigation, and (b) self-navigation. The self-navigated slice has double the frame rate and is noticeably sharper than that acquired with interleaved-pulse navigation.

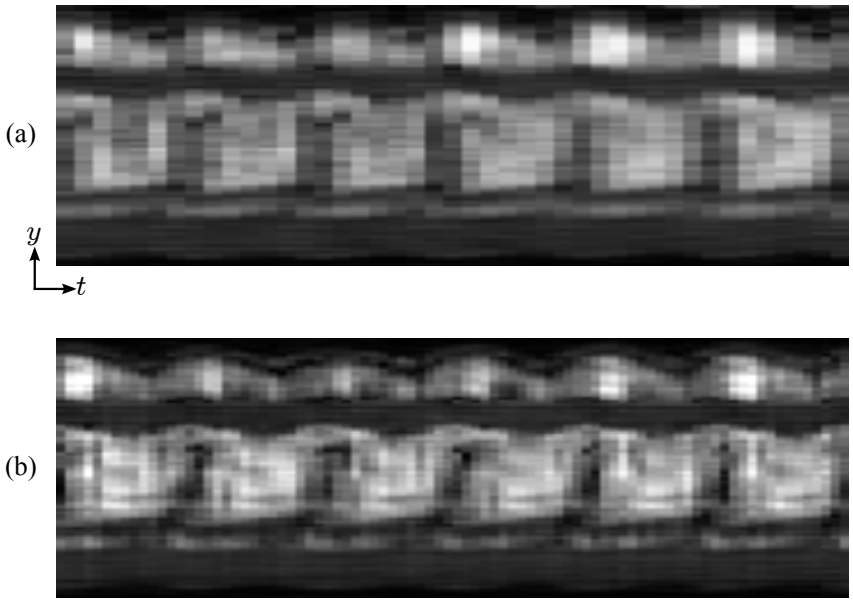

Figure 6.15: Spatiotemporal slices over the heart, using (a) interleaved-pulse navigation at 48 fps (7 fpb) and (b) self-navigation at 95 fps (14 fpb). The self-navigated slice is noticeably sharper due to the higher frame rate.

6.6.2 Demonstration

6.6.2.1 Rat subjects

In order to image the infiltration of micron-sized particles of iron oxide (MPIO)–labeled macrophages in the heart, we employed an IRI model in BN rats. IRI was induced by a 45 minute transient occlusion of the left circumflex coronary artery followed by reperfusion, resulting in inflammation of the affected myocardial tissue. Macrophages and monocytes

were labeled in circulation by intravenous administration of MPIO particles at least one day before imaging [112, 113]. We evaluated macrophage infiltration *in vivo* through T_2^*-weighted MRI using self-navigated subspace-constrained imaging. To highlight the utility of imaging MPIO-labeled immune cells, we also performed T_1-weighted LGE imaging, which is ubiquitous in cardiac MRI examinations [67]. After the conclusion of *in vivo* imaging, the hearts were excised and fixed in 4% paraformaldehye solution overnight and stored in phosphate buffered saline. T_2^* maps were then obtained using *ex vivo* MRI.

For *in vivo* T_2^*-weighted imaging, data were collected using $T_\mathrm{R} = 10.2$ ms, $T_\mathrm{E} = 5.1$ ms, FOV = 40 mm × 40 mm, matrix size = 256 × 256, spatial resolution = 0.16 mm × 0.16 mm (0.12 mu × 0.12 mu), slice thickness = 1 mm (0.8 mu), imaging time = 10 min, $N_\mathrm{ACS} = 32$, and $P = 2$. All data were collected continually with neither ECG gating/triggering nor breath holding using the Bruker Avance AV1 4.7 T scanner described in Section 6.3.1.1. Reconstructions were performed as in Section 6.6.1.1. The frame rate of the resulting images was 98 fps (15 fpb).

Ex vivo scans were performed on a Bruker Avance 11.7 T scanner with a single-channel volume coil using a multislice multiecho sequence with $T_\mathrm{R} = 1$ s, $T_\mathrm{E} = 8$ ms, 16 ms, 24 ms, ..., 64 ms (echoes = 8, echo spacing = 8 ms), FOV = 12.5 mm × 12.5 mm, matrix size =128 × 128, spatial resolution = 0.10 mm × 0.10 mm (0.075 mu × 0.075 mu), and slice thickness = 2 mm (1.5 mu).

Figure 6.16 shows (a) a self-navigated *in vivo* T_2^*-weighted short-axis slice from a rat with IRI on POD 4, as well as (b) a T_2^* map computed from *ex vivo* MRI. Dark patches are visible in the *in vivo* image and corroborated by the *ex vivo* T_2^* map, indicating macrophage accumulation to the myocardial region affected by the artery ligation. The self-navigated *in vivo* image sequence further revealed myocardial akinesis in the region surrounding the inflamed tissue, consistent with injury to that location.

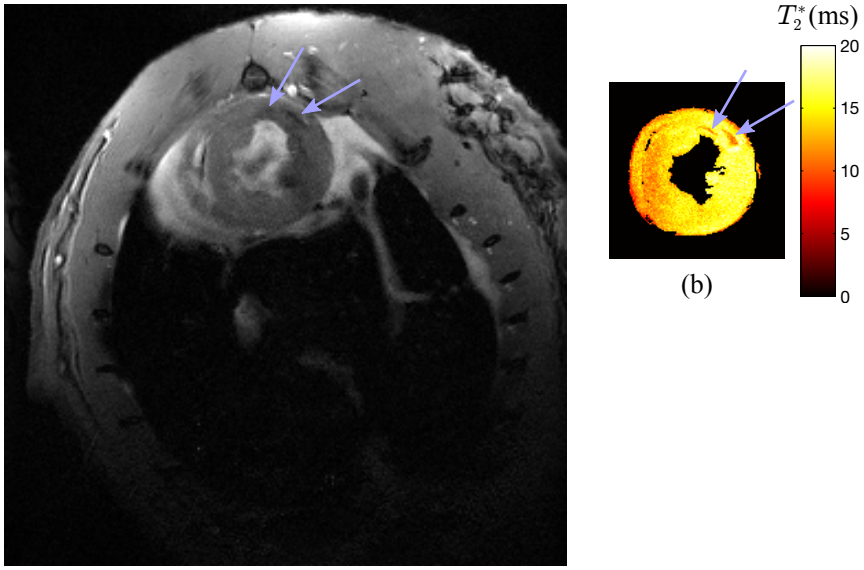

Figure 6.16: MPIO-labeled cell imaging of a short-axis slice on a rat with IRI (POD 4) using (a) self-navigated *in vivo* T_2^*-weighted imaging, and (b) *ex vivo* T_2^*-mapping. The dark patches of myocardial tissue visible in the *in vivo* image indicate macrophage accumulation and are corroborated by the *ex vivo* T_2^* map.

6.6.3 Contrast mechanism comparison

6.6.3.1 Rat subjects

For LGE imaging, the Bruker IntraGate method was used to acquire retrospectively gated T_1-weighted images 10 minutes after the introduction of a 0.1 mmol/kg bolus of gadolinium-based contrast agent. LGE imaging data were collected using $T_{\mathrm{R}} = 5.6$ ms, $T_{\mathrm{E}} = 3.1$ ms, FOV = 40 mm × 40 mm, matrix size = 128 × 128, spatial resolution = 0.31 mm × 0.31 mm (0.24 mu × 0.24 mu), slice thickness = 1 mm (0.8 mu), and imaging time = 10 min. Images were acquired using the Bruker Avance AV1 4.7 T scanner described in Section 6.3.1.1.

Figure 6.17 shows an LGE image from the same subject as in Fig. 6.16. The image shows no gadolinium contrast enhancement in the myocardium, indicating that the myocardium is still viable; the only indication of the injury was myocardial akinesis (observed in this image sequence just as in the self-navigated T_2^*-weighted images). The lack of late gadolinium en-

hancement in Fig. 6.16 highlights the difference between MPIO-labeled immune cell imaging and LGE imaging, demonstrating the value of imaging macrophage accumulation.

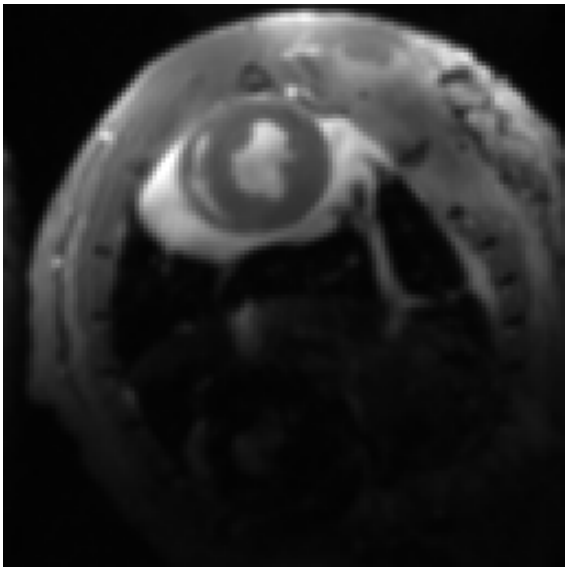

Figure 6.17: Gated LGE imaging of the same subject. Despite the reperfusion injury, no gadolinium contrast enhancement is visible in the myocardium, highlighting the difference between MPIO and other contrast mechanisms such as gadolinium-based agents.

Chapter 7

Discussion and Conclusions

7.1 Cine imaging

Each set of images in Figure 6.2 depicts the same myocardial wall motion at different frame rates. The subspace-constrained images are free of the experimental burdens and sensitivities to arrhythmia which are characteristic of ECG-gated images. Additionally, the subspace-constrained images capture respiratory motion (the IntraGate images were created using retrospective respiratory gating) and depict the entire image sequence (as opposed to a single representative cardiac cycle). Each of the subspace approaches reconstructed more cardiac phases per cycle than the IntraGate method, with the self-navigated images having the highest frame rate (95 fps = 14 fpb).

The primary tradeoff of the speed boost from self-navigation is a later minimum echo time; however, the signal gain from a longer repetition time may offset the signal loss from the later echo time, depending on the T_1 and T_2^* values of the tissue being imaged. Indeed, when compared to Fig. 6.2-b, the self-navigated images in Fig. 6.2-c have increased T_2^*-weighting due to the later echo time but higher overall SNR due to the longer repetition time. The

importance of this tradeoff is application-dependent: for T_2^*-weighted imaging applications such as labeled cell imaging, an even later echo time is desired, and the tradeoff disappears entirely.

In Figs. 6.3 and 6.4, the results using $L_1 < L_2$ show clear improvement over the results using $L_1 = L_2$ and the full-rank (i.e., CS) methods. The reconstructions with $L_1 < L_2$ clearly depict the cardiac and respiratory cycles without the blurring seen in the other reconstructions. All three reconstructions fit the data to the same degree, but the model with $L_1 < L_2$ is the most flexible: it exhibits the least model bias and captures more subtle temporal variations than do the other models. The other reconstructions show a clear model bias, relying far more heavily on $(\mathbf{r}, f)$-space sparse regularization than did the model with $L_1 < L_2$.

Figure 6.5 demonstrates the effectiveness of the approach for ungated, free-breathing imaging given particularly high spatial and temporal resolution requirements, successfully imaging mouse hearts at 97 fps (12 fpb) with an in-plane spatial resolution of 0.12 mm (0.18 mu).

7.2 Myocardial perfusion imaging

In Fig. 6.8, the proposed image reconstruction method with $L_1 < L_2$ shows some improvement over the proposed method with $L_1 = L_2$, although the differences between the reconstructions are less obvious than in the human case. As in the human case, all reconstructions match the measured data to the same degree. The images from the proposed method with $L_1 < L_2$ are sharper and show slightly less model bias than the images from the proposed method with $L_1 = L_2$. The increased similarity between the two reconstructions can be partly attributed to the increased reliance of the proposed method with $L_1 < L_2$ on the $(\mathbf{r}, f)$-space sparse regularization term for more highly undersampled scenarios such as whole-heart 3D imaging. The subspace model allows storage of $\mathbf{C}(\rho)$ in the factored form

$\mathbf{\Psi\Phi}$, allowing memory-efficient computation even in high-dimensional cases for which $\mathbf{C}(\rho)$ cannot be stored in memory. The CS method requires the full $\mathbf{C}(\rho)$ to be stored at each iteration, and was therefore not computed due to memory limitations.

In Fig. 6.9, hypoperfusion is apparent in the apical and septal segments, both of which are associated with LAD blood supply [114]; the ligated artery was identifiable using the proposed method.

In Fig. 6.10-a,b, the extent of the in-plane LGE perfusion defect matches in the 2D IntraGate reference images and the corresponding slice from the 3D images. The defect is specifically seen in the mid-ventricular anterior and anterolateral myocardial segments. The contrast weighting of the 2D and 3D images are different due to the differences between slice excitation and slab excitation; here, the 3D images have a better contrast enhancement ratio. The additional benefit of 3D imaging can be seen in Fig. 6.10-c, which shows how far the perfusion defect extends along the anterior and lateral walls of the myocardium towards the apex.

The first-pass perfusion measurements in Fig. 6.11-b indicate extensive myocardial damage when compared to the control rat in Fig. 6.11-a. This is clearest in the apical anterior, mid-ventricular anterior, mid-ventricular anterolateral, and apical lateral segments, which is consistent with the LGE images in Fig. 6.10.

7.3 Extracellular volume fraction mapping

Figure 6.14 shows the ability of jointly modeled explicit-subspace imaging to generate the 3D T_1 maps appropriate for ECV calculation without requiring ECG or respiratory control. Elevated ECV values were apparent in the anterior, anterolateral, and apical myocardial segments, consistent with interruption in the LCx blood supply. This demonstrates that ECV measurement using 3D explicit-subspace imaging is a potentially powerful tool for

myocardial tissue characterization.

However, it may ultimately be desirable to use a pulse sequence other than FLASH, which has the following major limitations in the context of dynamic T_1 mapping. First, the FLASH contrast equation assumes that the system has reached a steady-state after many RF pulses. The time required to reach steady-state precludes quick cycling between contrasts. Different contrasts are instead collected asynchronously, requiring an extra analysis step to extract matching cardiac cycles for T_1 fitting. Second, T_1 fitting requires knowledge of the flip angles $\{\alpha_i\}_{i=1}^{F}$, each of which is a function of the RF pulse $\mathbf{B}_1(\mathbf{r}, t)$ used for excitation. A number of practical issues lead to uncertainty in the true values of $\{\alpha_i\}_{i=1}^{F}$, including B_1 inhomogeneity, non-rectangular excitation profiles (especially troublesome for 2D imaging), and nonlinearity of the flip angle as a function of transmit power.

Several other pulse sequences for T_1 mapping of the myocardium are available as an alternative to FLASH (e.g., [115–119]). These sequences allow synchronous/interleaved contrasts; furthermore, they are robust to B_1 inhomogeneity, as they rely on variable timings rather than variable flip angles. Because the contrasts are synchronous, joint modeling of different contrasts could potentially be performed through the extension of low-rank modeling to low-rank tensor modeling [120, 121].

7.4 Labeled cell imaging

Figure 6.15 reveals the accelerated frame rate provided by self-navigation. The efficiency of the self-navigated pulse sequence offers an immediate two-fold increase in imaging speed without affecting image contrast weighting, thereby enabling high-speed, free-breathing MPIO-labeled cell imaging without ECG or respiratory gating.

Figure 6.16 demonstrates the feasibility of self-navigated T_2^* MPIO-labeled cell imaging. The method is capable of producing high-resolution images which indicate macrophage in-

filtration through negative contrast, allowing noninvasive identification of inflamed tissue. Coupled with the akinesis at the site of the negative contrast (revealed by the *in vivo* images), the high level of agreement between Figs. 6.16-a and 6.16-b confirms that the dark patches imaged *in vivo* indeed arise from shortened T_2^* due to the accumulation of MPIO-labeled macrophages.

T_2^*-weighted imaging with SPIO labeling provides complementary information to other contrast weightings and contrast agents, as evidenced by Fig. 6.17. LGE imaging, which is performed far more commonly than SPIO-labeled cell imaging, is the clinical gold standard for assessing myocardial viability. As such, LGE does not indicate minor injuries which cause inflammation, only injuries that irreversibly damage the myocardium. The lack of gadolinium contrast enhancement in Fig. 6.17 underscores the utility of SPIO as a contrast agent. Even though the entire myocardium is viable (as demonstrated by the lack of gadolinium contrast enhancement), the tissue is still inflamed, which cannot be inferred from the LGE images alone.

7.5 Conclusions

Cardiovascular MRI can be significantly accelerated by leveraging explicit-subspace low-rank imaging, particularly when integrated with parallel imaging and sparse modeling. This dissertation has described a novel approach to integrate these three approaches. We have shown that non-Cartesian navigation makes subspace estimation robust to navigator orientation and that the data acquisition speed of subspace-constrained imaging can be further improved using self-navigated pulse sequences which collect both navigator and imaging data within the same T_R interval. These properties of the proposed data acquisition scheme have been validated using both simulation and *in vivo* cardiac imaging data.

This explicit-subspace approach has been shown to achieve imaging speeds high enough

to represent cardiac and respiratory motion without the need for gating or triggering. Very high imaging speeds are even achievable in 3D: for example, speeds of up to 74 fps (11 fpb) at 0.31 mm × 0.31 mm × 1.0 mm (0.24 mu × 0.24 mu × 0.77 mu) spatial resolution were demonstrated in rats, depicting cardiac motion, respiratory motion, and contrast agent dynamics in a single experiment. Images with multiple contrasts can be jointly modeled, such as in the case of 3D T_1 mapping for ECV measurements.

We have also demonstrated T_2^*-weighted imaging of inflamed myocardial tissue at 0.16 mm (0.12 mu) in-plane spatial resolution and 98 fps (15 fpb) using self-navigation. Use of the self-navigated pulse sequence doubles the imaging speed as compared to interleaved-pulse navigation, accelerating SPIO-labeled cell imaging. Using self-navigated T_2^*-weighted imaging, we have observed macrophage accumulation *in vivo* without the use of cardiac or respiratory gating. Our noninvasive method for assessment of SPIO-labeled macrophage accumulation (corroborated by *ex vivo* T_2^* maps and observed regional myocardial akinesis) identified reperfusion injury where gadolinium contrast enhancement could not.

This dissertation presented an approach to accelerated MRI exploiting mathematical signal properties of cardiovascular images, allowing comprehensive evaluation of the heart through the visualization and measurement of cardiac structures and functions in very high spatial and temporal resolution. Looking forward, even greater advances may be achievable by additionally incorporating physics, physiology, computational modeling, and machine learning. Synergistic integration of computational modeling and imaging could leverage physical and physiological properties of the heart, blood, and vasculature to reconstruct images from even less MR data; machine learning techniques could be used to directly populate computational models from $(\mathbf{k}, t)$-space data. Furthermore, a growing emphasis on quantitation will allow for more reproducible, objective diagnoses. These developments would not only enhance the capability of cardiovascular MRI but also transform biomedical imaging and its role in medicine.

References

[1] A. G. Christodoulou, P. Kellman, and Z.-P. Liang, "Accelerating cardiovascular magnetic resonance imaging: Signal processing meets nuclear spins," *IEEE Signal Process. Mag.*, vol. 31, no. 5, pp. 138–143, Sep. 2014.

[2] K. Lindström and I. Edler, "The history of echocardiography," *Ultrasound Med. Biol.*, vol. 30, pp. 1565–1644, Dec. 2004.

[3] W. T. Roberts, J. J. Bax, and L. C. Davies, "Cardiac CT and CT coronary angiography: Technology and application," *Heart*, vol. 94, pp. 781 –792, June 2008.

[4] F. M. Bengel, T. Higuchi, M. S. Javadi, and R. Lautamäki, "Cardiac positron emission tomography," *J. Am. Coll. Cardiol.*, vol. 54, pp. 1–15, June 2009.

[5] E. G. DePuey, E. V. Garcia, and D. S. Berman, Eds., *Cardiac SPECT imaging*, 2nd ed. Philadelphia, PA: Lippincott Williams & Wilkins, 2001.

[6] J. P. Finn, K. Nael, V. Deshpande, O. Ratib, and G. Laub, "Cardiac MR imaging: State of the technology," *Radiology*, vol. 241, pp. 338–354, Nov. 2006.

[7] S. Schalla, E. Nagel, H. Lehmkuhl, C. Klein, A. Bornstedt, B. Schnackenburg, U. Schneider, and E. Fleck, "Comparison of magnetic resonance real-time imaging of left ventricular function with conventional magnetic resonance imaging and echocardiography," *Am. J. Cardiol.*, vol. 87, pp. 95–99, Jan. 2001.

[8] K. S. Nayak and B. Hu, "The future of real-time cardiac magnetic resonance imaging," *Curr. Cardiol. Rep.*, vol. 7, pp. 45–51, Jan. 2005.

[9] D. J. Pennell, U. P. Sechtem, C. B. Higgins, W. J. Manning, G. M. Pohost, F. E. Rademakers, A. C. van Rossum, L. J. Shaw, and E. K. Yucel, "Clinical indications for cardiovascular magnetic resonance (CMR): Consensus Panel report," *Eur. Heart J.*, vol. 25, pp. 1940–1965, Nov. 2004.

[10] A. G. Christodoulou, H. Zhang, B. Zhao, T. K. Hitchens, C. Ho, and Z.-P. Liang, "High-resolution cardiovascular MRI by integrating parallel imaging with low-rank and sparse modeling," *IEEE Trans. Biomed. Eng.*, vol. 60, no. 11, pp. 3083–3092, Nov. 2013.

[11] Z.-P. Liang and P. C. Lauterbur, *Principles of Magnetic Resonance Imaging: A Signal Processing Perspective*. New York: IEEE Press, 2000.

[12] E. L. Hahn, "Spin echoes," *Phys. Rev.*, vol. 80, p. 580, 1950.

[13] P. C. Lauterbur, "Image formation by induced local interactions: Examples employing nuclear magnetic resonance," *Nature*, vol. 242, pp. 190–191, 1973.

[14] A. Kumar, D. Welti, and R. R. Ernst, "NMR Fourier zeugmatography," *J. Magn. Reson.*, vol. 18, pp. 69–83, 1975.

[15] D. B. Twieg, "The k-trajectory formulation of the NMR imaging process with applications in analysis and synthesis of imaging methods," *Med. Phys.*, vol. 10, pp. 610–621, 1983.

[16] Q.-S. Xiang and R. M. Henkelman, "K-space description for MR imaging of dynamic objects," *Magn. Reson. Med.*, vol. 29, pp. 422–428, 1993.

[17] J. Frahm, A. Haase, and D. Matthaei, "Rapid NMR imaging of dynamic processes using the FLASH technique," *Magn. Reson. Med.*, vol. 3, pp. 321–327, Apr. 1986.

[18] H.-J. Weinmann, R. C. Brasch, W.-R. Press, and G. E. Wesbey, "Characteristics of gadolinium-DTPA complex: A potential NMR contrast agent," *Am. J. Roentgenol.*, vol. 142, no. 3, pp. 619–624, 1984.

[19] D. Widder, W. Greif, K. Widder, R. Edelman, and T. Brady, "Magnetite albumin microspheres: A new MR contrast material," *Am. J. of Roentgenol.*, vol. 148, no. 2, pp. 399–404, 1987.

[20] G. Golub and V. Pereyra, "Separable nonlinear least squares: The variable projection method and its applications," *Inverse Probl.*, vol. 19, no. 2, p. R1, 2003.

[21] P. Mansfield, "Multi-planar image formation using NMR spin echoes," *J. Phys. C: Solid State Phys.*, vol. 10, p. L55, 1977.

[22] C. B. Ahn, J. H. Kim, and Z. H. Cho, "High-speed spiral-scan echo planar NMR imaging–I," *IEEE Trans. Med. Imaging*, vol. 5, pp. 2–7, Mar. 1986.

[23] A. Haase, J. Frahm, D. Matthaei, W. Hanicke, and K. D. Merboldt, "FLASH imaging. Rapid NMR imaging using low flip-angle pulses," *J. Magn. Reson.*, vol. 67, pp. 258–266, Apr. 1986.

[24] A. Oppelt, R. Graumann, H. B. H. Fisher, W. Hartl, and W. Schajor, "FISP–a new fast MRI sequence," *Electromedica*, vol. 54, pp. 15–18, 1986.

[25] K. Sekihara, "Steady-state magnetizations in rapid NMR imaging using small flip angles and short repetition intervals," *IEEE Trans. Med. Imaging*, vol. 6, pp. 157–164, June 1987.

[26] Z.-P. Liang, H. Jiang, C. P. Hess, and P. C. Lauterbur, "Dynamic imaging by model estimation," *Int. J. Imag. Syst. Tech.*, vol. 8, pp. 551–557, 1997.

[27] J. Tsao, P. Boesiger, and K. P. Pruessmann, "k-t BLAST and k-t SENSE: Dynamic MRI with high frame rate exploiting spatiotemporal correlations," *Magn. Reson. Med.*, vol. 50, pp. 1031–1042, 2003.

[28] B. Madore, G. Glover, and N. J. Pelc, "Unaliasing by Fourier-encoding the overlaps using the temporal dimension (UNFOLD), applied to cardiac imaging and fMRI," *Magn. Reson. Med.*, vol. 42, pp. 813–828, Nov. 1999.

[29] N. Aggarwal and Y. Bresler, "Patient-adapted reconstruction and acquisition dynamic imaging method (PARADIGM) for MRI," *Inverse Probl.*, vol. 24, 2008.

[30] M. Lustig, J. M. Santos, D. L. Donoho, and J. M. Pauly, "k-t SPARSE: High frame rate dynamic MRI exploiting spatio-temporal sparsity," in *Proc. Int. Soc. Magn. Reson. Med.*, 2006, p. 2420.

[31] M. Lustig, D. L. Donoho, and J. M. Pauly, "Sparse MRI: The application of compressed sensing for rapid MR imaging," *Magn. Reson. Med.*, vol. 58, pp. 1182–1195, Dec. 2007.

[32] U. Gamper, P. Boesiger, and S. Kozerke, "Compressed sensing in dynamic MRI," *Magn. Reson. Med.*, vol. 59, pp. 365–373, Feb. 2008.

[33] H. Jung, K. Sung, K. S. Nayak, E. Y. Kim, and J. C. Ye, "k-t FOCUSS: A general compressed sensing framework for high resolution dynamic MRI," *Magn. Reson. Med.*, vol. 61, pp. 103–116, Jan. 2009.

[34] G. Adluru, C. McGann, P. Speier, E. G. Kholmovski, A. Shaaban, and E. V. R. DiBella, "Acquisition and reconstruction of undersampled radial data for myocardial perfusion magnetic resonance imaging," *J. Magn. Reson. Imaging*, vol. 29, pp. 466–473, 2009.

[35] R. Otazo, D. Kim, L. Axel, and D. K. Sodickson, "Combination of compressed sensing and parallel imaging for highly accelerated first-pass cardiac perfusion MRI," *Magn. Reson. Med.*, vol. 64, pp. 767–776, Sep. 2010.

[36] M. Usman, C. Prieto, T. Schaeffter, and P. G. Batchelor, "k-t group sparse: A method for accelerating dynamic MRI," *Magn. Reson. Med.*, vol. 66, pp. 1163–1176, Oct. 2011.

[37] C. Prieto, M. Usman, J. Wild, S. Kozerke, P. Batchelor, and T. Schaeffter, "Group sparse reconstruction using intensity-based clustering," *Magn. Reson. Med.*, vol. 69, no. 4, pp. 1169–1179, 2013.

[38] A. Sen Gupta and Z.-P. Liang, "Dynamic imaging by temporal modeling with principal component analysis," in *Proc. Int. Soc. Magn. Reson. Med.*, 2001, p. 10.

[39] Z.-P. Liang, "Spatiotemporal imaging with partially separable functions," in *Proc. IEEE Int. Symp. Biomed. Imaging*, 2007, pp. 988–991.

[40] H. Pedersen, S. Kozerke, S. Ringgaard, K. Nehrke, and W. Y. Kim, "k-t PCA: Temporally constrained k-t BLAST reconstruction using principal component analysis," *Magn. Reson. Med.*, vol. 62, pp. 706–716, Sep. 2009.

[41] J. P. Haldar and Z.-P. Liang, "Spatiotemporal imaging with partially separable functions: A matrix recovery approach," in *Proc. IEEE Int. Symp. Biomed. Imaging*, 2010, pp. 716–719.

[42] B. Zhao, J. P. Haldar, and Z.-P. Liang, "PSF model-based reconstruction with sparsity constraint: Algorithm and application to real-time cardiac MRI," in *Conf. Proc. IEEE Eng. Med. Biol. Soc.*, 2010, pp. 3390–3393.

[43] B. Zhao, J. P. Haldar, A. G. Christodoulou, and Z.-P. Liang, "Image reconstruction from highly undersampled (k, t)-space data with joint partial separability and sparsity constraints," *IEEE Trans. Med. Imaging*, vol. 31, pp. 1809–1820, Sep. 2012.

[44] S. Goud Lingala, Y. Hu, E. DiBella, and M. Jacob, "Accelerated dynamic MRI exploiting sparsity and low-rank structure: k-t SLR," *IEEE Trans. Med. Imaging*, vol. 30, pp. 1042–1054, May 2011.

[45] M. Fu, B. Zhao, C. Carignan, R. K. Shosted, J. L. Perry, D. P. Kuehn, Z.-P. Liang, and B. P. Sutton, "High-resolution dynamic speech imaging with joint low-rank and sparsity constraints," *Magn. Reson. Med.*, 2015, *in press*.

[46] C. Brinegar, S. S. Schmitter, N. N. Mistry, G. A. Johnson, and Z.-P. Liang, "Improving temporal resolution of pulmonary perfusion in rats using the partially separable function model," *Magn. Reson. Med.*, vol. 64, pp. 1162–1170, Oct. 2010.

[47] F. Lam and Z.-P. Liang, "A subspace approach to high-resolution spectroscopic imaging," *Magn. Reson. Med.*, vol. 71, no. 4, pp. 1349–1357, 2014.

[48] E. J. Candès and B. Recht, "Exact matrix completion via convex optimization," *Found. Comput. Math.*, vol. 9, pp. 717–772, Dec. 2009.

[49] E. J. Candès and T. Tao, "The power of convex relaxation: Near-optimal matrix completion," *IEEE Trans. Inf. Theory*, vol. 56, pp. 2053–2080, 2010.

[50] A. Papoulis, "Generalized sampling expansion," *IEEE Trans. Circuits Syst.*, vol. 24, pp. 652–654, Nov. 1977.

[51] L. Ying and Z.-P. Liang, "Parallel MRI Using Phased Array Coils," *IEEE Signal Process. Mag.*, vol. 27, pp. 90–98, July 2010.

[52] J. Carlson and T. Minemura, "Imaging time reduction through multiple receiver coil data acquisition and image reconstruction," *Magn. Reson. Med.*, vol. 29, pp. 681–687, 1993.

[53] D. K. Sodickson and W. J. Manning, "Simultaneous acquisition of spatial harmonics (SMASH): Fast imaging with radiofrequency coil arrays," *Magn. Reson. Med.*, vol. 38, pp. 591–603, Oct. 1997.

[54] P. M. Jakob, M. A. Grisowld, R. R. Edelman, and D. K. Sodickson, "AUTO-SMASH: A self-calibrating technique for SMASH imaging," *MAGMA*, vol. 7, pp. 42–54, 1998.

[55] K. P. Pruessmann, M. Weiger, M. B. Scheidegger, and P. Boesiger, "SENSE: Sensitivity encoding for fast MRI," *Magn. Reson. Med.*, vol. 42, pp. 952–962, Nov. 1999.

[56] M. A. Griswold, P. M. Jakob, M. Nittka, J. W. Goldfarb, and A. Haase, "Partially parallel imaging with localized sensitivities (PILS)," *Magn. Reson. Med.*, vol. 44, pp. 602–609, 2000.

[57] W. E. Kyriakos, L. P. Panych, D. F. Kacher, C.-F. Westin, S. M. Bao, R. V. Mulkern, and F. A. Jolesz, "Sensitivity profiles from an array of coils for encoding and reconstruction in parallel (space rip)," *Magn. Reson. Med.*, vol. 44, pp. 301–308, 2000.

[58] M. A. Griswold, P. M. Jakob, R. M. Heidemann, M. Nittka, V. Jellus, J. Wang, B. Kiefer, and A. Haase, "Generalized autocalibrating partially parallel acquisitions (GRAPPA)," *Magn. Reson. Med.*, vol. 47, pp. 1202–1210, June 2002.

[59] E. J. Candès, J. Romberg, and T. Tao, "Robust uncertainty principles: Exact signal reconstruction from highly incomplete frequency information," *IEEE Trans. Inf. Theory*, vol. 52, pp. 489–509, Feb. 2006.

[60] D. L. Donoho, "Compressed sensing," *IEEE Trans. Inf. Theory*, vol. 52, pp. 1289–1306, Apr. 2006.

[61] E. J. Candès, J. K. Romberg, and T. Tao, "Stable signal recovery from incomplete and inaccurate measurements," *Comm. Pure Appl. Math.*, vol. 59, pp. 1207–1223, Aug. 2006.

[62] P. Feng and Y. Bresler, "Spectrum-blind minimum-rate sampling and reconstruction of multiband signals," in *Proc. IEEE Int. Conf. Acoust., Speech, Signal Process.*, vol. 3, 1996, pp. 1688–1691.

[63] R. Venkataramani and Y. Bresler, "Further results on spectrum blind sampling of 2d signals," in *Proc. IEEE Int. Conf. Image Process.*, vol. 2, 1998, pp. 752–756.

[64] E. J. Candès, "The restricted isometry property and its implications for compressed sensing," *Comptes Rendus Mathematique*, vol. 346, pp. 589–592, 2008.

[65] E. Candès and J. Romberg, "Sparsity and incoherence in compressive sampling," *Inverse Probl.*, vol. 23, p. 969, 2007.

[66] M. Lustig, D. L. Donoho, J. M. Santos, and J. M. Pauly, "Compressed sensing MRI," *IEEE Signal Process. Mag.*, vol. 25, pp. 72–82, Mar. 2008.

[67] P. Kellman and A. E. Arai, "Cardiac imaging techniques for physicians: Late enhancement," *J. Magn. Reson. Imaging*, vol. 36, no. 3, pp. 529–542, 2012.

[68] P. Kellman, J. R. Wilson, H. Xue, M. Ugander, and A. E. Arai, "Extracellular volume fraction mapping in the myocardium, part 1: Evaluation of an automated method," *J. Cardiovasc. Magn. Reson.*, vol. 14, p. 63, 2012.

[69] M. Jerosch-Herold, R. T. Seethamraju, C. M. Swingen, N. M. Wilke, and A. E. Stillman, "Analysis of myocardial perfusion MRI," *J. Magn. Reson. Imaging*, vol. 19, pp. 758–770, June 2004.

[70] D. Atkinson, D. Burstein, and R. Edelman, "First-pass cardiac perfusion: Evaluation with ultrafast MR imaging," *Radiology*, vol. 174, no. 3, pp. 757–762, 1990.

[71] Y.-J. L. Wu, Q. Ye, L. M. Foley, T. K. Hitchens, K. Sato, J. B. Williams, and C. Ho, "In situ labeling of immune cells with iron oxide particles: An approach to detect organ rejection by cellular MRI," *Proc. Natl. Acad. Sci. U.S.A.*, vol. 103, pp. 1852–1857, Feb. 2006.

[72] A. G. Christodoulou, S. D. Babacan, and Z.-P. Liang, "Accelerating cardiovascular imaging by exploiting regional low-rank structure via group sparsity," in *Proc. IEEE Int. Symp. Biomed. Imaging*, 2012, pp. 330–333.

[73] C. Eckart and G. Young, "The approximation of one matrix by another of lower rank," *Psychometrika*, vol. 1, pp. 211–218, 1936.

[74] S. D. Solomon, N. Anavekar, H. Skali, J. J. McMurray, K. Swedberg, S. Yusuf, C. B. Granger, E. L. Michelson, D. Wang, S. Pocock et al., "Influence of ejection fraction on cardiovascular outcomes in a broad spectrum of heart failure patients," *Circulation*, vol. 112, no. 24, pp. 3738–3744, 2005.

[75] A. G. Christodoulou, T. K. Hitchens, Y. Wu, C. Ho, and Z.-P. Liang, "Improved subspace estimation for low-rank model-based accelerated cardiac imaging," *IEEE Trans. Biomed. Eng.*, vol. 61, no. 9, pp. 2451–2457, Sep. 2014.

[76] A. G. Christodoulou, Y.-L. Wu, T. K. Hitchens, C. Ho, and Z.-P. Liang, "Self-Navigated low-rank MRI for MPIO-labeled immune cell imaging of the heart," in *Conf. Proc. IEEE Eng. Med. Biol. Soc.*, 2014, pp. 1529–1532.

[77] A. G. Christodoulou, C. Brinegar, J. P. Haldar, H. Zhang, Y.-J. L. Wu, L. M. Foley, T. K. Hitchens, Q. Ye, C. Ho, and Z.-P. Liang, "High-resolution cardiac MRI using partially separable functions and weighted spatial smoothness regularization," in *Conf. Proc. IEEE Eng. Med. Biol. Soc.*, 2010, pp. 871–874.

[78] A. G. Christodoulou, B. Zhao, and Z.-P. Liang, "Regularized image reconstruction for PS model-based cardiovascular MRI," in *Proc. IEEE Int. Symp. Biomed. Imaging*, 2011, pp. 57–60.

[79] B. Sharif, J. A. Derbyshire, A. Z. Faranesh, and Y. Bresler, "Patient-adaptive reconstruction and acquisition in dynamic imaging with sensitivity encoding (PARADISE)," *Magn. Reson. Med.*, vol. 64, pp. 501–513, Aug. 2010.

[80] B. Zhao, J. P. Haldar, C. Brinegar, and Z.-P. Liang, "Low rank matrix recovery for real-time cardiac MRI," in *Proc. IEEE Int. Symp. Biomed. Imaging*, 2010, pp. 996–999.

[81] J. P. Haldar, D. Hernando, S.-K. Song, and Z.-P. Liang, "Anatomically constrained reconstruction from noisy data," *Magn. Reson. Med.*, vol. 59, pp. 810–818, 2008.

[82] C. A. Mistretta, "Undersampled radial MR acquisition and highly constrained back projection (HYPR) reconstruction: Potential medical imaging applications in the post-Nyquist era," *J. Magn. Reson. Imaging*, vol. 29, pp. 501–516, 2009.

[83] Y. Ming and L. Yi, "Model selection and estimation in regression with grouped variables," *J. R. Stat. Soc. Series B Stat. Methodol.*, vol. 68, pp. 49–67, 2006.

[84] J. Huang and T. Zhang, "The benefit of group sparsity," *Ann. Statist.*, vol. 38, pp. 1978–2004, 2010.

[85] J. Debbins, J. Felmlee, and S. Riederer, "Phase alignment of multiple surface coil data for reduced bandwidth and reconstruction requirements in volumetric MRI applications," in *IEEE Antennas and Propag. Soc. Int. Symp.*, vol. 2, July 1997, pp. 1214–1217.

[86] D. O. Walsh, A. F. Gmitro, and M. W. Marcellin, "Adaptive reconstruction of phased array MR imagery," *Magn. Reson. Med.*, vol. 43, pp. 682–90, May 2000.

[87] M. Bydder, D. J. Larkman, and J. V. Hajnal, "Combination of signals from array coils using image-based estimation of coil sensitivity profiles," *Magn. Reson. Med.*, vol. 47, pp. 539–48, Mar. 2002.

[88] R. L. Morrison, M. Jacob, and M. N. Do, "Multichannel estimation of coil sensitivities in parallel MRI," in *Proc. IEEE Int. Symp. Biomed. Imaging*, 2007, pp. 117–120.

[89] M. Lustig and J. M. Pauly, "SPIRiT: Iterative self-consistent parallel imaging reconstruction from arbitrary k-space," *Magn. Reson. Med.*, vol. 64, pp. 457–71, Aug. 2010.

[90] W. S. Hoge and D. H. Brooks, "Using GRAPPA to improve autocalibrated coil sensitivity estimation for the SENSE family of parallel imaging reconstruction algorithms," *Magn. Reson. Med.*, vol. 60, no. 2, pp. 462–467, Aug. 2008.

[91] J. Wang, T. Kluge, M. Nittka, V. Jellus, B. Kühn, and B. Kiefer, "Parallel acquisition techniques with modified SENSE reconstruction mSENSE," in *Proc. 1st Würzburg Workshop on Parallel Imaging Basics and Clin. Appl.*, 2001, p. 92.

[92] "Field-of-view limitations in parallel imaging," *Magn. Reson. Med.*, vol. 52, pp. 1118–1126, 2004.

[93] D. Geman and C. Yang, "Nonlinear image recovery with half-quadratic regularization," *IEEE Trans. Image Process.*, vol. 4, pp. 932–946, July 1995.

[94] M. Nikolova and M. K. Ng, "Analysis of half-quadratic minimization methods for signal and image recovery," *SIAM J. Sci. Comput.*, vol. 27, pp. 937–966, Oct. 2005.

[95] Y. Wang, J. Yang, W. Yin, and Y. Zhang, "A new alternating minimization algorithm for total variation image reconstruction," *SIAM J. Imaging Sci.*, vol. 1, pp. 248–272, 2008.

[96] E. van den Berg and M. P. Friedlander, "Sparse optimization with least-squares constraints," Department of Computer Science, University of British Columbia, Tech. Rep., Jan. 2011.

[97] N. Kawel, E. B. Turkbey, J. J. Carr, J. Eng, A. S. Gomes, W. G. Hundley, C. Johnson, S. C. Masri, M. R. Prince, R. J. van der Geest et al., "Normal left ventricular myocardial thickness for middle-aged and older subjects with steady-state free precession cardiac magnetic resonance: The multi-ethnic study of atherosclerosis," *Circ. Cardiovasc. Imaging*, vol. 5, no. 4, pp. 500–508, 2012.

[98] M. Fishbein, D. Maclean, and P. Maroko, "Experimental myocardial infarction in the rat: Qualitative and quantitative changes during pathologic evolution," *Am. J. Path.*, vol. 90, no. 1, p. 57, 1978.

[99] X.-M. Gao, A. M. Dart, E. Dewar, G. Jennings, and X.-J. Du, "Serial echocardiographic assessment of left ventricular dimensions and function after myocardial infarction in mice," *Cardiovasc. Res.*, vol. 45, no. 2, pp. 330–338, 2000.

[100] W. B. Kannel, C. Kannel, R. S. Paffenbarger, and L. A. Cupples, "Heart rate and cardiovascular mortality: The Framingham Study," *Am. Heart J.*, vol. 113, no. 6, pp. 1489–1494, 1987.

[101] D. Pass and G. Freeth, "The rat," *ANZCCART News*, vol. 6, no. 4, pp. 1–4, 1993.

[102] K. Kramer, S. A. van Acker, H.-P. Voss, J. A. Grimbergen, W. J. van der Vijgh, and A. Bast, "Use of telemetry to record electrocardiogram and heart rate in freely moving mice," *J. Pharmacol. Toxicol. Methods*, vol. 30, no. 4, pp. 209–215, 1993.

[103] Committee for the Update of the Guide for the Care and Use of Laboratory Animals; National Research Council, *Guide for the Care and Use of Laboratory Animals: Eighth Edition.* The National Academies Press, 2011.

[104] V. A. Morozov, "On the solution of functional equations by the method of regularization," *Sov. Math. Dokl.*, vol. 7, pp. 414–417, 1966.

[105] G. K. Sethi and J. G. Copeland, "Routine surveillance endomyocardial biopsy," *Ann. Thorac. Surg.*, vol. 64, no. 5, p. 1230, 1997.

[106] Y.-J. L. Wu, Q. Ye, K. Sato, L. M. Foley, T. K. Hitchens, and C. Ho, "Noninvasive evaluation of cardiac allograft rejection by cellular and functional cardiac magnetic resonance," *JACC Cardiovasc. Imaging*, vol. 2, pp. 731–741, June 2009.

[107] A. G. Christodoulou, H. Zhang, B. Zhao, Q. Ye, T. K. Hitchens, C. Ho, and Z.-P. Liang, "High-resolution 3D first-pass myocardial perfusion imaging," in *Proc. Int. Soc. Magn. Reson. Med.*, 2012, p. 1151.

[108] M. D. Cerqueira, N. J. Weissman, V. Dilsizian, A. K. Jacobs, S. Kaul, W. K. Laskey, D. J. Pennell, J. A. Rumberger, T. Ryan, and M. S. Verani, "Standardized myocardial segmentation and nomenclature for tomographic imaging of the heart: A statement for healthcare professionals from the Cardiac Imaging Committee of the Council on Clinical Cardiology of the American Heart Association," *Circulation*, vol. 105, pp. 539–542, 2002.

[109] B. Zhao, F. Lam, and Z.-P. Liang, "Model-based MR parameter mapping with sparsity constraints: Parameter estimation and performance bounds," *IEEE Trans. Med. Imaging*, vol. 33, pp. 1832–1844, Sep. 2014.

[110] B. Zhao, W. Lu, T. K. Hitchens, F. Lam, C. Ho, and Z.-P. Liang, "Accelerated MR parameter mapping with low-rank and sparsity constraints," *Magn. Reson. Med.*, 2015, *in press.*

[111] J. A. Nelder and R. Mead, "A simplex method for function minimization," *Comput. J.*, vol. 7, no. 4, pp. 308–313, 1965.

[112] E. M. Shapiro, S. Skrtic, K. Sharer, J. M. Hill, C. E. Dunbar, and A. P. Koretsky, "MRI detection of single particles for cellular imaging," *Proc. Natl. Acad. Sci. U.S.A.*, vol. 101, no. 30, pp. 10 901–10 906, 2004.

[113] E. M. Shapiro, K. Sharer, S. Skrtic, and A. P. Koretsky, "In vivo detection of single cells by MRI," *Magn. Reson. Med.*, vol. 55, no. 2, pp. 242–249, 2006.

[114] J. Bogaert, S. Dymarkowski, and A. Taylor, Eds., *Clinical Cardiac MRI*. Germany: Springer-Verlag Berlin Heidelberg, 2005.

[115] D. R. Messroghli, A. Radjenovic, S. Kozerke, D. M. Higgins, M. U. Sivananthan, and J. P. Ridgway, "Modified Look-Locker inversion recovery (MOLLI) for high-resolution T1 mapping of the heart," *Magn. Reson. Med.*, vol. 52, no. 1, pp. 141–146, 2004.

[116] S. K. Piechnik, V. M. Ferreira, E. Dall'Armellina, L. E. Cochlin, A. Greiser, S. Neubauer, and M. D. Robson, "Shortened modified look-locker inversion recovery (shmolli) for clinical myocardial t1-mapping at 1.5 and 3 t within a 9 heartbeat breathhold," *J. Cardiovasc. Magn. Reson.*, vol. 12, no. 1, p. 69, 2010.

[117] K. Chow, J. A. Flewitt, J. D. Green, J. J. Pagano, M. G. Friedrich, and R. B. Thompson, "Saturation recovery single-shot acquisition (SASHA) for myocardial T1 mapping," *Magn. Reson. Med.*, vol. 71, no. 6, pp. 2082–2095, 2014.

[118] S. Weingärtner, M. Akçakaya, T. Basha, K. V. Kissinger, B. Goddu, S. Berg, W. J. Manning, and R. Nezafat, "Combined saturation/inversion recovery sequences for improved evaluation of scar and diffuse fibrosis in patients with arrhythmia or heart rate variability," *Magn. Reson. Med.*, vol. 71, no. 3, pp. 1024–1034, 2014.

[119] S. Weingärtner, S. Roujol, M. Akçakaya, T. A. Basha, and R. Nezafat, "Free-breathing multislice native myocardial T1 mapping using the slice-interleaved T1 (STONE) sequence," *Magn. Reson. Med.*, 2015, *in press*.

[120] A. G. Christodoulou and Z.-P. Liang, "Accelerated multiparameter mapping using low-rank tensors," in *Proc. Int. Soc. Magn. Reson. Med.*, 2015, p. 104.

[121] A. G. Christodoulou and Z.-P. Liang, "3D dynamic T1 mapping of the myocardium using a time-varying subspace," in *Proc. Int. Soc. Magn. Reson. Med.*, 2015, p. 2614.